Graphene-Wrapped Hierarchical TiO_2 Nanoflower Composites with Enhanced Photocatalytic Performance

by

Gregory Lui

A thesis

presented to the University of Waterloo

in fulfilment of the

thesis requirement for the degree of

Master of Applied Science

in

Chemical Engineering

Waterloo, Ontario, Canada, 2014

Author’s Declaration

I hereby declare that I am the sole author of this thesis. This is a true copy of my thesis, including any required final revisions, as accepted by my examiners.

I understand that my thesis may be made electronically available to the public.

Abstract

Increasing energy demands as well as the depletion of traditional energy sources has led to the need for the development and improvement of energy conversion and storage technologies. Concerns regarding climate change and environmental awareness has also created increased support for renewable energy and clean technology research. One technology of interest is the photocatalyst, which is a material that is able to use natural light irradiation to create electrical currents or drive useful chemical reactions. For this purpose, a strong photocatalytic material has the following properties: i) strong absorbance over a wide solar radiation spectrum; ii) high surface area for adsorbance of target species; iii) high electron efficiency characteristics such as high conductivity, long charge-carrier lifetimes, and direct pathways for electron transport; and iv) good chemical stability. All of these requirements serve to maximize the efficiency and overall output of the device, and are a means of overcoming the performance hurdle required for the commercialization of various energy conversion technologies.

Unfortunately, current photocatalytic materials suffer from small absorbance windows and high recombination rates which greatly reduce the conversion efficiency of the catalyst. Titanium dioxide (TiO_2), the most well-known and widely used photocatalyst, can only absorb light within the ultraviolet (UV) range – which accounts for only a small fraction of the entire solar spectrum. For this reason, the majority of recent research has been directed toward producing photocatalysts that are able to absorb light within the visible and infrared range in order to maximize the amount of light absorbed in the solar spectrum. Other research is also being conducted to increase electrical conductivity and charge-carrier separation to further increase conversion efficiency.

It is hoped that these two major problems surrounding photocatalysis can be solved by using novel functional nanomaterials. Nanomaterials can be synthesized using three main techniques: crystal structuring, doping, and heterostructuring. By controlling the structure of the crystal, materials of different phase, morphology, and exposed crystal facets can be synthesized. These are important for controlling the electronic properties and surface reactivity of the photocatalyst. Doping is the act of introducing impurities into a material in order to modify its band structure and create a red shift in light absorption. Lastly, heterostructuring is a method used to combine different photocatalysts or introduce co-catalysts in order to widen the range of absorption, encourage charge separation, or both. Many novel photocatalytic materials have been synthesized using these techniques. However, the next-generation photocatalytic material has remained elusive due to the high cost of production and complexity of synthesis.

This thesis proposes a novel photocatalytic material that can be used in photocatalyzed waste-water remediation. Graphene-wrapped hierarchical TiO_2 nanoflowers (G-TiO_2) are synthesized using a facile synthesis method. TiO_2 is a material of particular interest due to its chemical and photo-corrosion stability, high redox potential, strong electronic properties, and relative non-toxicity. Hierarchical structures are highly desired because they are able to achieve both high surface area and high conductivities. Graphene hybridization is a popular method for creating composites with highly conductive networks and highly adsorptive surfaces. To the best of my knowledge, the hybridization of graphene on hierarchical TiO_2 structures without pre-functionalization of TiO_2 has not yet been demonstrated in literature. Therefore, it is proposed that the use of such a material would greatly simplify the synthesis process and

enhance the overall photocatalytic performance of TiO_2 over that of commercial TiO_2 photocatalysts.

In the first study, hierarchical TiO_2 nanoflowers are synthesized using a solvothermal reaction. It is then shown that under UV irradiation, the hierarchical TiO_2 material is able to outperform commercial TiO_2 material in the photodegradation of methylene blue (MB). Further characterization shows that this improvement is explained by a higher electrical conductivity, and exists in spite of having a lower specific surface area compared to the commercial material.

In the second study, G-TiO_2 is synthesized by mixing hierarchical TiO_2 nanoflowers with graphene oxide (GO) and reducing GO in a hydrothermal reaction. Photocatalytic tests show that this hybridization further improves the performance of the hierarchical TiO_2. Further studies reveal that an optimal graphene loading of 5 wt% is desired in order to achieve the higher rate of MB decomposition, and greatly outperforms P25 in this task. Characterization shows that G-TiO_2 composites have increased specific surface area and electrical conductivity compared to the hierarchical TiO_2 nanoflower.

It is believed that this work will provide a simple and efficient avenue for synthesizing graphene–TiO_2 composites with greatly improved photocatalytic activity. This work may also find use in other photocatalytic applications such as chemical deconstruction and manufacturing, hydrogen production, solar cells, and solar enhanced fuel cells.

Acknowledgements

I would first like to thank my family – Yvonne, Geoffrey, and Genny – for their continued patience, care, and support in my pursuit of higher education. Thank you for everything, dad.

I would also like to thank my colleagues who have given me guidance and assistance throughout the tenure of my degree: Dr. Jin-Yun Liao, Aoshu Duan, and Brian Kim. I also thank Dr. Zhongwei Chen for providing additional lab space and equipment for me to perform my research.

Finally, I would like to thank my supervisors Dr. Aiping Yu and Dr. Michael Fowler for their invaluable advice and guidance throughout this process.

Soli Deo gloria.

Table of Contents

List of Figures

List of Tables

List of Abbreviations, Symbols and Nomenclature

A	Absorbance
BET theory	Brunauer–Emmett–Teller theory, describes the surface adsorption of gas molecules
c	BET constant; concentration
C	Concentration
C_0	Equilibrium concentration
CVD	Chemical vapour deposition
d	Distance between two features; lattice spacing between two crystal faces
DRS	Diffuse Reflectance UV-Vis Spectroscopy
E_g	Band gap
E_h	Acceleration potential of an electron beam
EHP	Electron-hole pair
EIS	Electrochemical impedance spectroscopy
$F(R\infty)$	Approximation of absorbance used in the Kubelka-Munk transformation
FTIR	Fourier-transform infrared spectroscopy
FWHM	Full width half maximum
GO	Graphene oxide
Graphene-TiO_2	General composites made from graphene and TiO_2 materials.
G-TiO_2	Specific composites made from wrapping graphene around hierarchical TiO_2 flowers
h	Planck constant
$h\nu$	Band gap expressed in terms of the Planck constant and wavenumber
K	Shape factor
L	Path length
MB	Methylene blue
m_e	Rest mass of an electron
NA	Numerical aperture
p	Equilibrium pressure

p_0	Saturation pressure
PVD	Physical vapour deposition
RGO	Reduced graphene oxide
SAED	Selected area electron diffraction
SEM	Scanning electron microscopy
SHE	Standard hydrogen electrode
TEM	Tunnelling electron microscopy
UV-Vis	Ultraviolet-Visible
XRD	X-Ray Diffraction
$Z'(\Omega)$	Real part of impedance value
$Z''(\Omega)$	Imaginary part of impedance value
Z_W	Warburg impedance
β	Line broadening at full width half maximum
ε	Molar absorptivity/extinction coefficient
θ	Incident angle of light
λ	Wavelength of light
v	Total adsorbed gas quantity
v_m	Monolayer adsorbed gas quantity
τ	Crystallite size
Ω	Impedance

1.0 Introduction

As the world faces growing concerns regarding environmental issues and energy sources, the scientific community is looking for cleaner solutions to existing problems. In the face of dwindling fossil fuel resources, energy production, and storage industries are under pressure to provide technologies that are clean and renewable. Waste remediation and pollution control technologies are in high demand in order to combat the increasing emissions of an increasing world population. Although Canada is continually working towards lowering its greenhouse gas emissions, its oil and gas and transportation sectors continue to contribute the largest and growing greenhouse gas emissions.[1]

Photocatalysts are a recently discovered class of materials that are a potential solution to many of the energy concerns described above. Fujishima showed in 1972 that photocatalytic materials such as titanium dioxide (TiO_2) could convert natural sunlight into photo-generated charge-carriers that were able to split water into oxygen and hydrogen gas.[2] This discovery was significant because the work implied that a completely passive and renewable mechanism could be used to produce energy in the form of hydrogen fuel. Since then, photocatalysts have been used in various applications, including waste-water treatment, sterilization, cancer therapy,[3] dye-sensitized solar cells,[4] and hydrocarbon cracking.[5]

The reason TiO_2 is able to act as a photocatalyst is because of its many desirable optical properties. The redox chemistry of TiO_2 is such that it is highly reactive with many other compounds. TiO_2 is also very chemically stable, even under light irradiation, making it a strong candidate for a photocatalytic material. The main issues surrounding TiO_2 and its future development is three-fold. First, the recombination rate of charge-carriers in conventional TiO_2

particles is high, leading to low efficiencies and photocatalytic activities. Second, TiO_2 only absorbs light within the ultraviolet (UV) spectrum, limiting it to less than 10% of the solar spectrum.[6] Lastly, the affinity of target species for TiO_2 is much smaller than other materials. This lack of adsorption presents a mass transfer issue during photocatalysis.

It is for the aforementioned reasons that research on improved photocatalytic systems is continuing to grow.[7, 8] TiO_2 photocatalytic activity can be improved by controlling its morphology, introducing dopants, and heterostructuring TiO_2 with other materials.[9] The objective of this thesis work is to: (i) show the merits of hierarchical morphologies in photocatalysis; and (ii) pair hierarchical TiO_2 structures with graphene to create a material with enhanced photocatalytic activity over a commercial photocatalyst. Specifically, this work outlines the first attempt in literature to produce graphene-wrapped hierarchical TiO_2 in the photodegradation of methylene blue (MB) as a model for waste-water purification. Graphene is a material of great interest in many applications for its high conductivity and high surface area. It is believed that the use of graphene as a co-catalytic material in photocatalysis can address many of the issues currently plaguing conventional TiO_2 photocatalysts.

1.1 Thesis Organization

This thesis will focus on the development of a specific graphene-TiO_2 composite configuration that can be used in the photocatalytic degradation of organic compounds in waste-water. In Section 2, a brief overview of the operating principles of photocatalysts is given, highlighting the necessary properties of a strong photocatalytic material. TiO_2 is then presented as a

potential photocatalyst. The synthesis and use of TiO_2 in literature as a photocatalyst is discusses in greater detail, including the merits of hierarchical morphologies in optical and electronic applications. Lastly, graphene is introduced as a co-catalytic material, and graphene-TiO_2 composites found in literature are explored. Section 3 provides a brief explanation of the characterization techniques used in this work.

Section 4 covers the first study performed in this thesis work. Hierarchical TiO_2 nanoflower material is synthesized using a solvothermal reaction. The photocatalytic activity of these TiO_2 nanoflowers are then evaluated against a commercial TiO_2 material (P25) using MB as the target species. Various characterization techniques are performed to determine the factors behind the improved catalytic activity of the hierarchical material.

Section 5 contains the second study of this thesis work. Hierarchical TiO_2 nanoflowers are wrapped in graphene sheets via the reduction of graphene oxide in a hydrothermal reaction. The photocatalytic activity of this graphene-TiO_2 composite is again tested in the photodegradation of MB and compared with P25. The mass of graphene is also controlled to determine the optimal weight loading of graphene on TiO_2 for photocatalysis. The composite is characterized extensively to determine the nature of the benefits of graphene as a co-catalyst. Lastly, Section 6 gives a conclusion of the work described in this thesis and the future direction of this research.

2.0 Background

2.1 Basic Principles of Photocatalysis

Photocatalysis, as its name implies, involves the acceleration of a chemical reaction via a light-activated catalyst. Photocatalysts use photo-generated electron-hole pairs (EHPs) to generate free radical species that can undergo secondary reactions. Because of the nature of photo-generation, photocatalysts rely on a class of materials called semiconductors to perform this type of process.

Semiconductors are materials that have all of their valence shells filled with electrons.[10] Because of this, electrons are not mobile within the material and semiconductors are not intrinsically conductive. When enough energy is put into the system, an electron can be excited to the next unfilled shell, also called the conduction band. Since the conduction band was previously empty, electrons that are excited to this band have much more mobility. This charge-carrier movement creates a current within the semiconductor. The gap in which no energy states exists is called the electronic band gap, and is the amount of energy required to excite an electron from the valence band to the conduction band. It is important to note that the band gap is the minimum amount of energy required to excite an electron. It is possible to excite an electron with energy greater than the band gap, however the electron may relax back down to the conduction band edge and release energy in the form of phonons.

When an electron is excited from the valence band to the conduction band, it leaves behind an electron vacancy. In semiconductor theory, this vacancy is referred to as a ‘hole’ – an

imaginary particle that holds a positive charge. Therefore, the movement or transition of a hole in one direction is actually the movement or transition of an electron in the opposite direction.

Once an EHP is generated, these charge-carriers must be separated and transported to an active site for reaction. EHP separation is necessary because electrons have a tendency to lower their potential energy, and by extension holes have a tendency to increase their potential energy. Therefore, EHPs have a tendency to recombine in order to create a more thermodynamically favourable system.

This unique characteristic of charge-carriers is important for understanding how they interact with other molecules in redox reactions. Redox reactions are chemical reactions in which the oxidation state of an atom is changed.[11] This means that an electron transfer has taken place. The term, 'redox,' is a portmanteau used to describe two types of electron transfer processes: reduction and oxidation. Reduction is the process of gaining electrons, leading to a decrease in the oxidation state of a species. Oxidation is the process of losing electrons, leading to an increase in the oxidation state of a species.

Redox reactions require a driving force in order to proceed. Redox potentials are a measure of the tendency of chemical species toward these types of reactions. For example, in a solution containing two species, the species with a more positive electrochemical potential will have a tendency to gain an electron from the species with a less positive electrochemical potential. This is the same behaviour of charge-carriers described previously, except stated in terms of electrochemical potentials: Electrons have a tendency to move toward species with higher electrochemical potentials (or lower potential energies), reducing the species; and, holes have

a tendency to move toward lower electrochemical potentials (or high potential energies), oxidizing the species.

The above processes describe the mechanism by which photocatalysts, such as TiO_2, induce chemical reactions (Figure 1): (i) an incident photon with sufficient energy strikes the photocatalyst, photo-generating an EHP; (ii) the EHP are either separated and reach an active site on the surface of the photocatalyst (a), or they recombine, ending the process (b); and, (iii) successfully separated electrons and holes undergo reduction and oxidation reactions with adsorbed species, respectively. In an aqueous solution, photocatalysts can react with water or other organic compounds to form radical species. These species are highly reactive and are 'resolved' through various oxidation reactions, eventually leading to products such as CO_2 and H_2O (Equations 1 to 3c).[12]

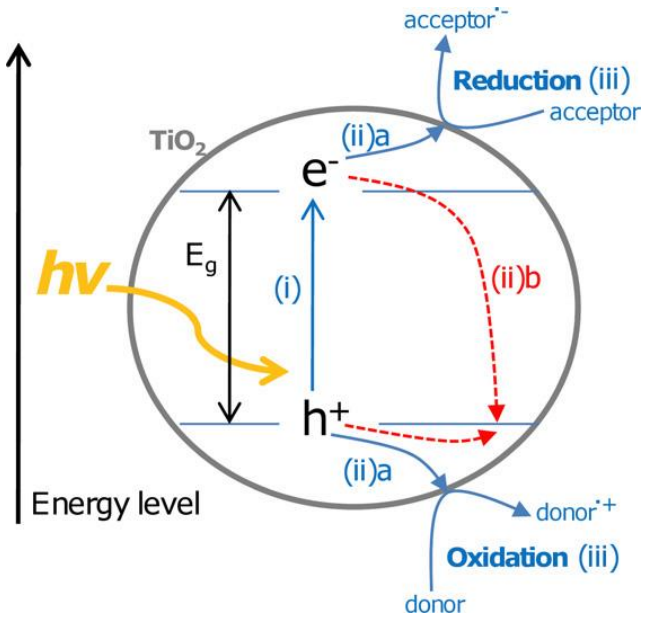

Figure 1: Illustration of the basic photocatalytic mechanism.[7]

$$TiO_2 + h\nu \rightarrow e^- + h^+ \quad (1)$$

$$e^- + O_2 \rightarrow O_2 \cdot \quad (2a)$$

$$O_2 \cdot + H^+ \rightarrow HO_2 \quad (2b)$$

$$HO_2 + e^- + H^+ \rightarrow H_2O_2 \quad (3c)$$

$$H_2O_2 + e^- \rightarrow \cdot OH + OH^- \quad (4d)$$

$$H_2O_2 + O_2 \cdot \rightarrow \cdot OH + OH^- + O_2 \quad (5e)$$

$$2O_2 \cdot + H_2O \rightarrow O_2 + HO_2 \cdot + OH^- \quad (6f)$$

$$h^+ + TiOH/OH^-/H_2O \rightarrow R/R \cdot / \cdot ROH \quad (3a)$$

$$\rightarrow O_2 \cdot, HOO \cdot, HOOH, HOO^-, HO \cdot, OH^-, H_2O \quad (3b)$$

$$\rightarrow H_2O + CO_2 \quad (3c)$$

Based on this reaction mechanism, there are four main requirements for a strong photocatalytic material: (i) chemical stability; (ii) absorbance over a wide light spectrum; (iii) high electron conductivity; and (iv) high specific surface area. These four requirements will be described in greater detail below:

Chemical Stability

Chemical stability and photo-corrosion resistance is an important property of photocatalysts for three reasons: First, a catalyst by definition should not be used up during a chemical reaction; second, the decomposition of a catalyst means that it can no longer be used and must be replaced with new catalyst; and third, the decomposition of a catalyst can produce harmful or dangerous products.[13]

One example of a good photocatalytic material with low photo-corrosion resistance is cadmium sulfide (CdS). CdS has a band gap of 520 nm (2.39 eV), making it a candidate material for visible-light photocatalysis.[14] However, one issue with CdS, along with many

other metal sulfides, is that it can easily undergo photo-corrosion via the oxidation of S^{2-} (Equations 7 to 9). Not only does this destroy the photocatalyst and lower overall activity, but this decomposition also introduces toxic dissolved Cd^{2+} into solution, which is detrimental to health and quality of life.

$$CdS + h\nu \rightarrow e^- + h^+ \quad (7)$$

$$CdS + 2h^+ \rightarrow Cd^{2+} + S(s) \quad (8)$$

$$CdS + 2O_2 \rightarrow Cd^{2+} + 2O_4^{2+} \quad (9)$$

For this reason, unstable catalysts such as CdS require either a hole-scavenging species to reduce the rate of self-oxidation (such as a S^{2-}/SO_3^{2-} system),[14] or another co-catalyst that can accept holes from CdS, thus preventing oxidation of S^{2-}.[15]

Absorption Spectrum

The absorption requirements for a photocatalytic material appear obvious at first. The smaller the band gap the wider the range of light that can be absorbed. For example, the anatase phase of titanium dioxide (TiO_2) has a band gap of 3.2 eV and can only absorb light within the ultraviolet (UV) range.[2] As shown previously, CdS has a band gap of 2.39 eV, and can therefore absorb UV light as well as part of the visible-light spectrum.

It is important to understand redox potentials and the position of band gaps in materials, as these potentials determine the movement of charge-carriers. For example, in the case of photocatalytic water splitting, the photocatalyst must straddle both the H^+/H_2 reduction potential (0 eV vs. SHE) and the H_2O/O_2 oxidation potential (1.23 eV vs. SHE).[16] Based on

Figure 2 below, the band gaps of the semiconductors on the left are large (UV-active only) but are able to induce photocatalytic water splitting. The semiconductors in the middle are unstable because they are susceptible to redox reactions and decomposition. Lastly, the semiconductors on the right have unsuitable band edge positions. This means that the conduction band or valence band are too positive or negative to induce a reduction or oxidation reaction with water, respectively.

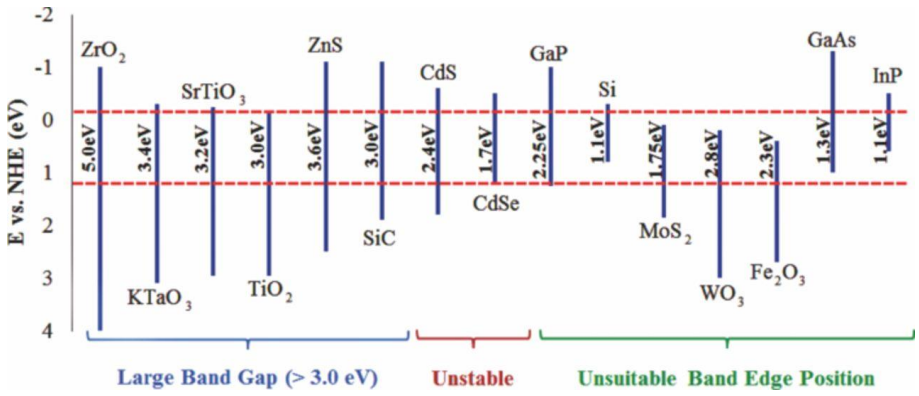

Figure 2: Redox potentials of various materials in evaluating suitability for water splitting. Reprinted with permission from publisher.[16] Copyright 2013, The Electrochemical Society.

Therefore, although smaller band gaps are desired for their absorption of higher wavelengths, one must guarantee that the band edge positions are suitable for the desired redox reaction. At the same time, if the desire redox reactions are known, then it is possible to find or tailor the best material with the most appropriate redox potentials to drive the reactions forward.

The absorption spectrum can therefore be increased by: (i) finding or synthesizing a material with a small band gap that perfectly straddles the desired redox reaction; (ii) doping a large band gap material to create intermediate states, effectively lowering the band gap; or, (iii)

heterostructuring a large band gap material with a small band gap material to create a wider absorption spectrum.

Electron Conductivity

A material's electrical conductivity is defined as its ability to allow the flow of electric current.[17] The higher the conductivity, the more easily electrons can move. Metals are considered the most conductive type of material because their Fermi levels – the hypothetical energy level that has a 50% chance of being occupied by an electron at thermodynamic equilibrium - exist within their energy band. This means that many energy levels exist near the Fermi level and can easily be occupied by electrons.

Unfortunately, photocatalytic materials are by nature semiconductors and therefore have no energy levels near their Fermi levels. This means that photocatalysts intrinsically have low conductivities. However, it is possible to improve the conductivity of photocatalysts by creating a composite with a conductive material such as a carbonaceous material. The crystal structure of the catalyst can also be improved to reduce the amount of defects and increase grain boundary size that can act as traps for charge-carriers.[18]

Surface Area

The surface area of a photocatalyst is important because an increased amount of active surface sites allows for creating more active oxygen species and adsorbing target species for decomposition.[19, 20] Because active sites are only found at the interface between the catalyst and the target medium, a high specific surface area ($m^2 \cdot g^{-1}$) is generally desired for all photocatalytic applications.

Given the criteria mentioned above, different photocatalytic materials have been proposed and are currently being researched.[21, 22] Relevant classes of materials include metal oxides, metal sulfides, and nitrides. Metal oxides are represented mainly by TiO_2,[2 23] ZnO,[24, 25] α-Fe_2O_3,[26, 27] and WO_3,[28, 29] though other binary metal oxide photocatalysis exist.[21] Ternary metal oxides such as $SrTiO_3$[30, 31] and $BiVO_4$[32, 33] have also been gaining attention as potential visible-light photocatalysts. Still, various other metal oxide combinations have been tested for their photocatalytic activity.[34, 35] Potential metal sulfide photocatalysts include CdS,[36, 37] ZnS,[38, 39] and more recently MoS_2 and WS_2.[40] Lastly, nitrides such as graphitic-C_3N_4 have been gaining attention for its simple and inexpensive synthesis and visible light activity.[41, 42] For the sake of brevity, this thesis will focus mainly on photocatalytic TiO_2 and its various forms, which will be discussed in detail in Section 2.2.

2.1.1 Testing of Photocatalytic Systems

Photocatalysts can be tested in various photocatalytic systems. Solution-based setups vary from simple batch suspension reactors and continuous flow annular reactors to more complex compound parabolic collecting reactors (shown in Figure 3) and photocatalytic membrane reactors.[43-46] Solution-based photocatalysis normally involves the treatment of waste water, the electrolysis of water (or water-splitting), or the directed cracking of specific hydrocarbons. Gas-based systems, such as powder layer reactors, fluidized bed reactors, and honeycomb monolith reactors, are often used to decompose harmful pollutants such as NO_X gas and volatile organic compounds.[47] The aim of all photocatalytic systems is to maximize the

exposed surface area of photocatalyst and the mass transport of target species to the surface of the photocatalyst while guaranteeing the highest throughput possible.

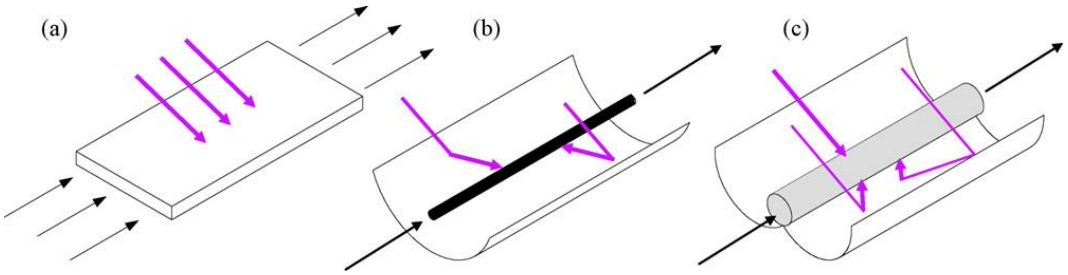

Figure 3: Diagram outlining the design of a compound parabolic collecting reactor (right). A non-concentration continuous flow reactor is shown on the left and a basic concentrating reactor in the center.[44]

In solution-based photocatalysis, many different target species are tested at the lab-scale including the degradation of pharmaceuticals and organic compounds, and the reduction of heavy metal ions.[48-51] At the same time, model compounds are used to provide a standard by which different research groups can compare results. One such model compound is $C_{16}H_{18}N_3SCl$, or methylene blue (MB), a textile dye that is considered toxic and a pollutant in textile effluents.[52] MB is a heterocyclic aromatic compound that easily dissolves in H_2O to form a positively charged molecule.[53] The adsorption of MB on TiO_2 and carbonaceous materials follows a monolayer Langmuir type isotherm.[54, 55] This means that MB will not form multiple layers on these surfaces, and that an equilibrium adsorption concentration of MB exists in solutions containing excess MB.

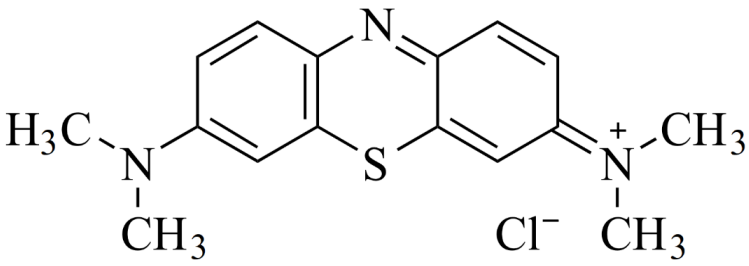

Figure 4: Chemical structure of methylene blue.

In this work, a batch reaction is employed. This system is chosen for its ease of use and simple characterization of photocatalysts compared to continuous-flow reactors. Batch reactions also allow for photocatalyst dispersions which maximizes the available surface area for reaction. Two beakers containing an aqueous photocatalyst solution are placed on two stir plates approximately 6 in (15.24 cm) away from a center lamp. While maintaining a dark environment without any illumination, stock MB solution is added to the photocatalyst solution under stirring. Without light irradiation, the MB in the solution slowly adsorbs onto the surface of the photocatalyst. After a certain period of time the solution is expected to reach adsorption-desorption equilibrium. The concentration of MB at this time is known as the equilibrium concentration (C_0). Because different photocatalytic materials differ in the amount of time it takes to reach adsorption-desorption equilibrium, a long period of time – such as one hour – is used to guarantee that concentration C_0 has been reached for all samples. This value remains consistent across all experiments.

At this point, the UV lamp can be turned on to begin the photocatalytic reaction. MB that is closest to the photocatalytic material – mainly the MB that is adsorbed on the surface – can undergo direct oxidation or reduction. The product of this redox reaction can then desorb from

the photocatalyst surface and allow another MB molecule to adsorb on the newly vacant active site. Vacant active sites can also be used to induce redox reactions with water species to produce active oxygen species that can further react with MB and cause decomposition.

As MB undergoes photocatalytic reduction and decomposition, it forms intermediates which are also reduced over time. The N-demethylation of MB causes the formation of intermediate products such as Azure B, Azure A, Azure C, and Thionine.[56] The decomposition of MB into these intermediates causes a blue shift in the characteristic absorbance peak (~664 nm). This blue shift in absorbance is similar to the behaviour seen in the N-deethylation of Rhodamine B.[57] The final products of MB decomposition are CO_2, SO_4^{2-}, NH_4^+, and NO_3^-.[54] The concentration of MB can be measured using an Ultraviolet-Visible (UV-Vis) spectrometer to determine the absorbance of MB in the range of 660 – 670 nm. The reduction of the absorbance peak in this range signals the removal of MB.

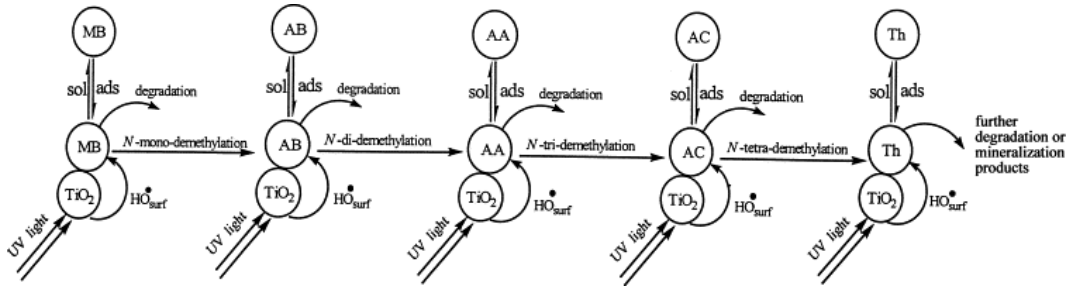

Figure 5: Proposed decomposition of MB during photocatalysis. N-demethylation causes the formation of intermediates Azure B (AB), Azure A (AA), Azure C (AC), and Thionine (Th), causing a blue shift in MB's characteristic absorbance peak.[56]

2.2 Titanium Dioxide (TiO_2) as a Photocatalytic Material

TiO_2 is a naturally occurring metal oxide that is typically found in the form of ilmenite ore. TiO_2 exists in three main mineral forms: anatase, rutile, and brookite. Both anatase and brookite are metastable states, and convert to rutile upon heating.[58] The photocatalytic activity of TiO_2 was first discovered by Fujishima in 1967 and published by Fujishima and Honda in 1972.[2] It was found that TiO_2 could use light irradiation to perform hydrolysis – the breaking of water molecules into hydrogen and oxygen gas – at active surface sites.

Since the discovery of this effect – called the Honda-Fujishima effect – TiO_2 has been used as a photocatalytic material in applications ranging from dye-sensitized solar cells[59] to antibacterial systems[60] to air pollution control.[61] Even today, TiO_2 has remained at the forefront of photocatalytic research because of its low cost, chemical stability, and large redox potentials with respect to water.[62]

Subsequent work revealed that TiO_2 could be modified in many different ways in order to improve its photocatalytic activity.[23] In addition to changing its mineral phase, impurities could be introduced to modify its absorption spectrum; the morphology of the material could be changed to improve surface area and conductivity; and, TiO_2 could be paired with other co-catalysts to improve overall performance.

The following sections will focus on: the properties of TiO_2 that make it a strong photocatalytic material; the various methods for synthesizing TiO_2; and, the specific control of TiO_2 morphology to form hierarchical structures.

2.2.1 TiO_2 Properties

The properties of TiO_2 relevant to photocatalysis have been widely studied.[63] The most photoactive active form of TiO_2 is thought to be anatase due to its high adsorption of organic compounds and high hole trapping rate,[64, 65] though the rutile and brookite phases have also been shown to be photoactive.[66] In fact, TiO_2 containing multiple phases have been shown to improve photocatalytic activity and reduce recombination of charge-carriers.[67, 68] Because anatase and rutile TiO_2 are the most relevant and widely studied phases, this section will focus on these phases only.

The most thermally stable crystal face of anatase is (101).[63] The (101) surface is corrugated and consists of alternating rows of 5-coordinated Ti atoms. The lowest energy crystal face of rutile is (110), which consists of 6-coordinated Ti atoms with bridging oxygens. Both anatase and rutile have tetragonal crystal structures, and the transformation of anatase into rutile is possible by annealing anatase at temperatures greater than 400°C.[69]

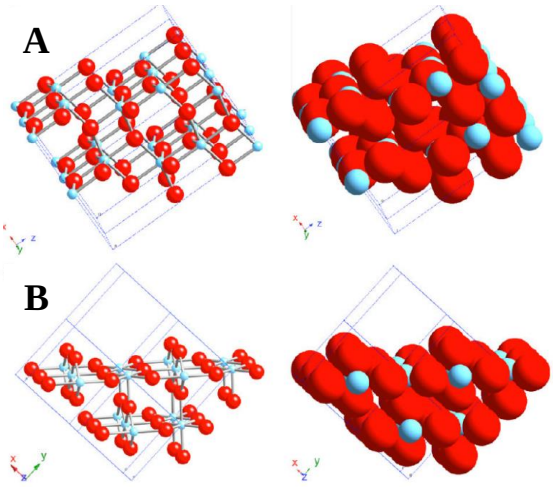

Figure 6: The most thermodynamically stable crystal faces of anatase TiO_2 (a) and rutile TiO_2 (b). Red spheres = O; blue spheres = Ti.[63]

TiO_2 is an intrinsic wide band gap semiconductor, with optical absorption gaps of 3.2 eV and 3.03 eV for anatase and rutile, respectively.[70] However, anatase and rutile can also be considered n-type semiconductors due to the natural oxygen vacancies within the lattice which reduces Ti^{4+} to Ti^{3+}.[63] These band gaps effectively place the absorption spectrum of pure TiO_2 within the ultraviolet range ($\lambda \approx 10 - 400$ nm).

It has been recently confirmed that mixed-phase TiO_2 containing anatase and rutile consists of a 0.4 eV band alignment, with anatase having a work function 0.2 eV larger than that of rutile (Figure 7).[67] This confirmation provides a strong theoretical basis for the use of mixed-phase TiO_2 to effectively separate EHPs, reducing charge recombination and increasing photocatalytic efficiency. TiO_2 can have a wide range of conductivities depending on its crystal structure and morphology. As a nanoporous film, TiO_2 has been shown to have conductivities as high as $3.7 \times 10^{-3}\ \Omega^{-1}\cdot cm^{-1}$.[71]

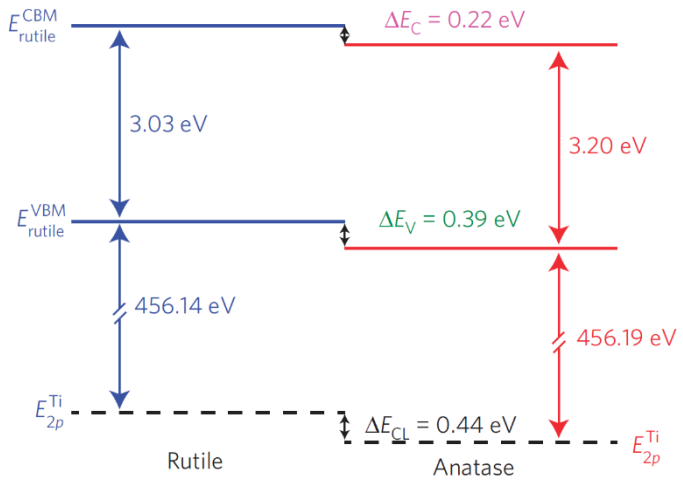

Figure 7: Band gap mismatch between anatase and rutile in mixed-phase TiO_2.[67]

At neutral pH, the conduction band of anatase has a potential of -0.5 eV vs. SHE (Figure 8).[72] The conduction band of anatase is negative enough to reduce O_2 to $O_2^{\bullet -}$ (-0.3 eV vs. SHE). The valence band is also sufficiently positive to oxidize H_2O and other hydroxide species to form their respective radicals. When placed relative to the redox potential of organic functional groups such as aromatics, phenols, amines, and sulfur bands, TiO_2 is very capable of inducing redox reactions.

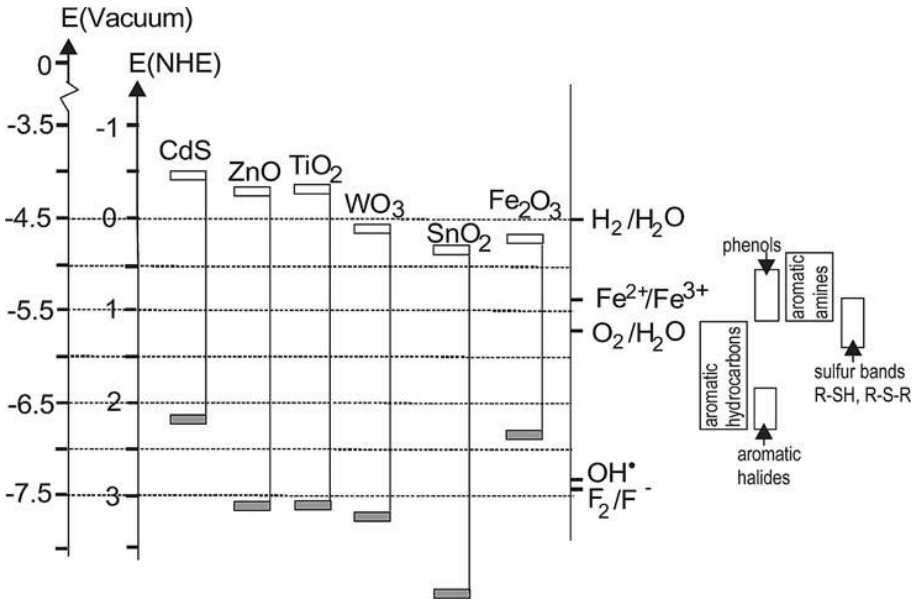

Figure 8: Band positions of various semiconductors including TiO_2. Relative redox potentials of various organic functional groups.[23]

Apart from photocatalytic applications, TiO_2 is used extensively as a pigment in paints and coatings, as a UV-blocker in sunscreens, and as a food additive.[73] TiO_2 is useful as a white pigment due to its high refractive index and, therefore, high brightness.[74] Its high refractive index means that light is easily bent and redirected off of the surface – even for very thin layers of TiO_2. With the addition of strong UV absorption, this also makes TiO_2 a useful additive in

sunscreens. In foodstuffs, TiO_2 is commonly used as both a whitening agent and as an anti-bacterial additive for increasing product shelf-life.

Unfortunately, the toxicity of nanoscale TiO_2 particles used in these applications have yet to be thoroughly studied. Although bulk TiO_2 is found to be inert and relatively non-toxic towards humans, existing toxicity studies performed on sub-micron TiO_2 particles has led the International Agency for Research on Cancer to label TiO_2 as an IARC Group 2B carcinogen, meaning that it is *possibly carcinogenic* to humans.[73] This evaluation is based on several studies. One of the largest epidemiological cohort studies performed in TiO_2 production industries in six European countries, as well as three other studies in the USA and Canada showed inadequate evidence for TiO_2 carcinogenicity in humans.[73, 75] However, ultrafine TiO_2 particles tested in rats, mice, and hamsters have shown sufficient evidence in animals for its carcinogenicity. For these reasons, TiO_2 is currently classified as possibly carcinogenic to human beings.

2.2.2 TiO_2 Synthesis

The synthesis of photocatalytic materials can be divided into three main approaches: morphology control, doping, and heterostructuring.[76] By controlling and fine-tuning the morphology of a photocatalyst, one can control the physical and electronic properties of the material. Doping, as mentioned previously, can be used to introduce intermediate energy states and lower the effective band gap of the material. Lastly, heterostructuring combines two

different materials in order to take advantage the properties of each material and improve charge-carrier separation.

TiO_2 can be synthesized using a wide array techniques and processes which have been extensively recorded in literature.[23, 76, 77] These include precipitation, sol-gel, emulsion, solvothermal and hydrothermal, electrochemical, chemical and physical vapour deposition (CVD and PVD), and microwave methods. Precipitation, sol-gel, and emulsion methods are often employed to create TiO_2 nanoparticles that can be used as films, membranes, or powders. These methods rely on the hydrolysis of TiO_2 precursors such as titanium oxysulfates, titanium chlorides and titanium alkoxides. These methods can also be used with templating compounds such as surfactants, block co-polymers, and other ordered structures to produce specific ordered membranes. Solvothermal and hydrothermal methods are high temperature, high pressure processes that use organic or aqueous solvents as media, respectively. These methods often begin with sol-gel solutions, and so use similar precursors. Solvothermal and hydrothermal reactions are favoured when specific complex morphologies are desired. CVD and PVD processes can be used to produce thin TiO_2 films. Lastly, microwave methods use high-frequency electromagnetic waves to induce hydrolysis of TiO_2 suspensions to form larger ordered structures.

Sol-gel synthesis of TiO_2 is one of the simplest and popular means of growing TiO_2 nanomaterials.[23, 78] Sol-gel methods can be used to produce high purity TiO_2, and processing parameters can be modified to change structure, introduce dopants, and form composites.[23] In sol-gel synthesis, TiO_2 is formed through the hydrolysis and condensation of a titanium alkoxide. Titanium salts can also be used, however this requires the removal of the anion after

synthesis. When sol-gel methods are combined with solvothermal and hydrothermal techniques, the range of TiO_2 materials that can be synthesized greatly diversifies.

TiO_2 can take various forms depending on the synthesis method.[77] Hydrothermal and solvothermal methods alone account for the synthesis of nanoparticles,[79] nanotubes,[80] nanosheets,[81] nanobelts,[82] nanorods,[83], nanowires,[84] nanowire arrays,[85] and aerogels.[86] Hierarchical morphologies are becoming an important part of the photocatalysis research due to the many benefits of combining different morphologies into one material.[20, 87, 88] Spherical 0D structures have the highest theoretical surface area, while highly crystalline 1D structures (such as nanotubes, nanobelts, nanorods, and nanowires) are known to have lower recombination rates and higher electron transport properties.[88] In order to address the scattering issues of smaller structures, larger 3D morphologies are desired to increase light scattering and absorbance.

An example of a hierarchical material is shown in Figure 9. In this example, a continuous film is cast or deposited on a substrate. This film consists of smaller nanowires, which themselves are comprised of even smaller nanoparticles. The nanoparticles provide a higher surface area for the material, while the nanowire morphology provides higher electrical conductivity between sites. Lastly, because the material can be made as a continuous film it can easily be applied to various surfaces.

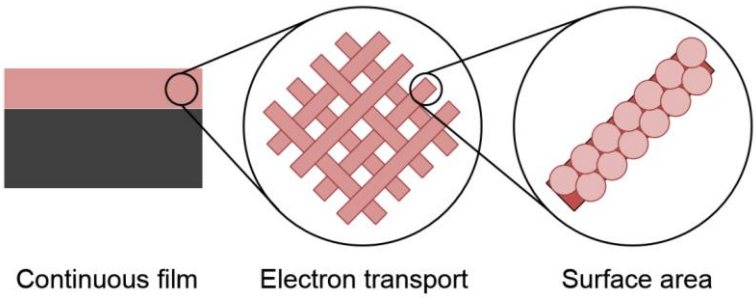

Figure 9: Example of a hierarchical structure: a continuous film consisting of nanowires that are themselves comprised of nanoparticles.

Even without the use of surfactants, various hierarchical morphologies can be synthesized using hydrothermal and solvothermal reactions. For example, Mali et al showed that hierarchical TiO_2 structures could be synthesized without the use of surfactants. By increasing the hydrothermal reaction temperature from 100°C to 190°C, Mali showed the evolution of TiO_2 morphology from 0D nanoparticles to 1D nanorods to ordered 3D dendritic structures. Similar hierarchical structures have also been shown by other research groups.[89-91]

TiO_2, and photocatalytic materials in general, can also be doped in order to change the band structure of the semiconductor material. The doping of TiO_2 has been explored extensively by research groups, including both metal ions (Fe, Mo, Ru, Os, Re, V, Rh, Co, Al, Ag, Pd, Pt, Zn, Zr, Cr, Mg, La, Ce, Er, Pr, Gd, Nd, Sm)[92-95] and non-metal ions (C,[96] N,[97] S,[98] F,[99] Cl/Br[68]). Dopants introduce energy bands within the band gap of semiconductors. These energy bands, although very close to either the valence band or conduction band (depending on their contribution to the band structure), causes a shift in the Fermi level and ultimately a reduction in the band gap of the material. Doping is commonly used with TiO_2 to cause a red shift in its absorption spectrum and induce visible light photoactivity. In general, *p*-doping is more

desirable than *n*-doping, since TiO_2 is intrinsically more oxidative than reductive of water molecular and other organic compounds. This means that the introduction of excess holes, unlike electrons, is more favourable for reducing band gap because their influence over the reduction potential of TiO_2 is less problematic.[9]

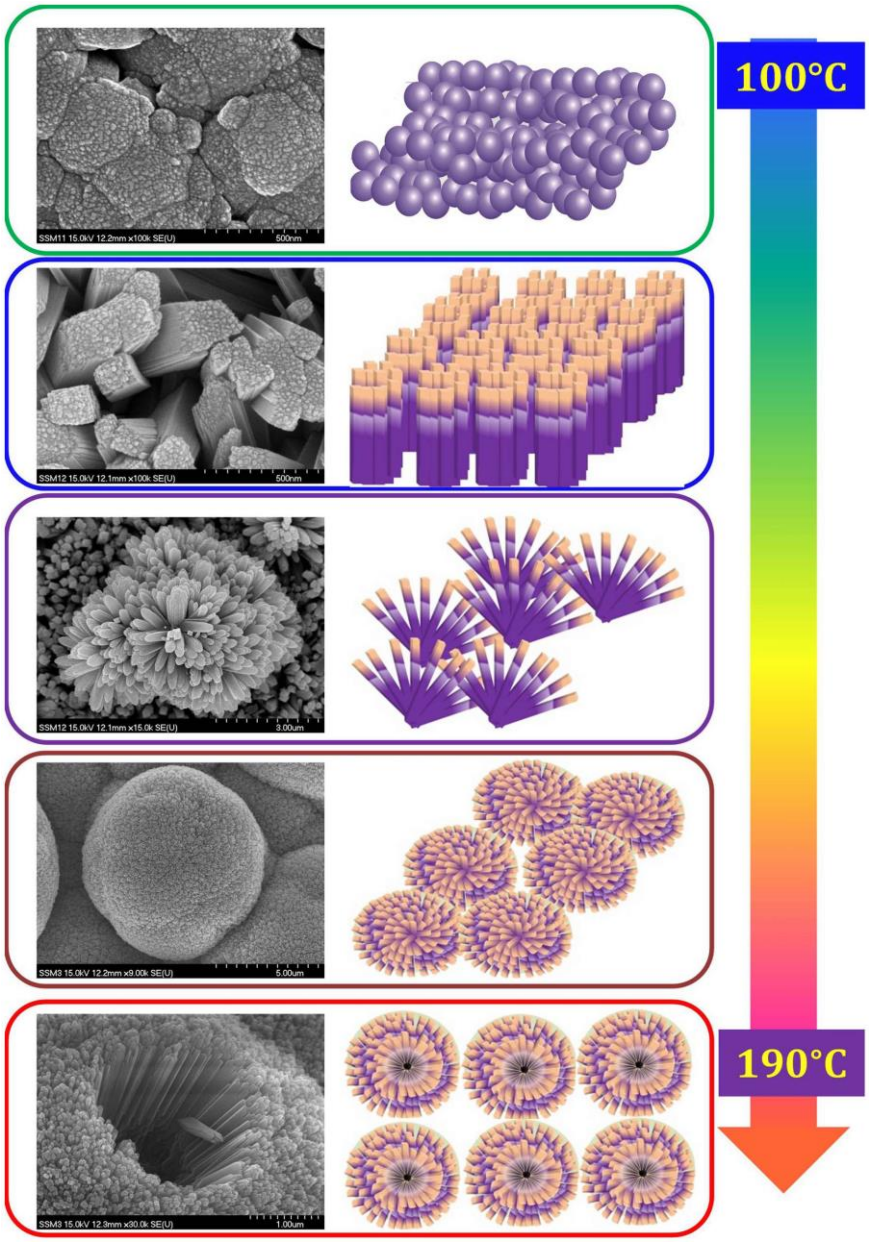

Figure 10: Various hierarchical morphologies of TiO_2 based on reaction temperature.[88]

The final means for improving photocatalytic activity is introducing a second distinct material that improves absorption of light, acts as a charge-carrier acceptor or donor, or both. The advantage of creating a heterogeneous photocatalyst like this is that the crystal structure and redox characteristics of TiO_2 are preserved, while additional properties can be provided by a secondary material. There are many types of heterogeneous mechanisms, but the most widely studied are charge-carrier transfer, indirect Z-scheme, sensitization, and co-catalyst coupling.[9] Charge-carrier transfer requires the pairing of TiO_2 with another semiconductor that produces a staggered band-alignment like that shown in Figure 7. In this configuration, electrons preferentially transfer to one semiconductor, while holes preferential transfer to the second semiconductor. Examples of semiconductors paired with TiO_2 include CdS,[100] Bi_2O_3,[101] PbS[102]. Charge-carrier transfer has the advantage of reducing recombination but also the disadvantage of ultimately lowering the reaction potential of both charge-carriers.

This disadvantage can be solved by using indirect Z-scheme processes, which separate the two semiconductors and place a redox mediator in between electrons from one semiconductor and holes from the other. This keeps reduction and oxidation reactions on separate semiconductors, while maintaining the reaction potential of all charge-carriers. An example of a TiO_2-based indirect Z-scheme is an anatase-rutile TiO_2 system using an IO^{3-}/I^- redox mediator.[103]

Sensitization improves the photocatalytic performance of TiO_2 by providing visible-NIR sensitivity in the form of a narrow band gap secondary material such as an organic dye like N719,[104] or semiconductor such as Cu_2O[105] or CdSe[106]. This heterostructure makes it possible to absorb light within both UV and visible spectrums, while maintaining the large redox potential of TiO_2.

Lastly, co-catalysts can be coupled with TiO_2 to either improve reactivity, improve absorbance, or act as electron acceptors. Both metals (Au, Pt, Ir, Ag, Pd, Ru, Rh)[107-109] and other semiconductors such as NiO and RuO_2[109] have been used as co-catalysts. Carbonaceous nanomaterials are also considered co-catalytic in these systems. It has been found that carbon-based materials can be used to photosensitize TiO_2 to larger wavelengths, reduce recombination through charge-carrier transfer, and provide more active surface sites.[7] Graphene is one such material that is being increasingly studied, and will be discussed in greater detail in the following section.

2.3 Graphene

Graphene is a very popular carbon nanomaterial due its highly interesting and beneficial properties.[110] Graphene was first successfully produced by Novoselov et al in 2004[111] and Geim and Novoselov were eventually given the 2010 Nobel Prize in Physics for their work.[112] Graphene consists monolayer, sp^2 hybridized, carbon atoms that create a 2D honeycomb lattice. This structure makes graphene the precursor to various other carbon materials such as 0D fullerenes, 1D nanotubes, and 3D graphite (Figure).[113] Each carbon atom can form a σ-bond with a neighbouring atom, and these bonds are responsible for the high mechanical strength of graphene. The unused *p* orbital is free to form π-bonds with neighbouring atoms, forming a half-filled orbital. The result is a highly conjugated structure that allows for extremely high conductivity. In fact, calculations show that graphene has a mobility in excess of 15 000 $cm^2 \cdot V^{-1} \cdot s^{-1}$ and a resistivity as low as 10^{-6} $\Omega \cdot cm^{-1}$.[113, 114] In theory, these

characteristics make graphene one of the strongest and most conductive materials presently known.

An additional property of graphene is its high specific surface area. Calculations show that monolayer graphene has a maximum theoretical specific surface area of 2630 $m^2 \cdot g^{-1}$.[115] This high surface area, combined with its highly conjugated structure, makes graphene a suitable material for adsorbing other conjugated compounds, such as aromatics, via π-π interactions.[116]

Lastly, graphene is known to be a zero-band gap material with a work function of -4.42eV – just below that of anatase TiO_2 (-4.40 eV).[117, 118] This makes graphene a good electron acceptor of anatase TiO_2 and electrons have a tendency to transfer to graphene, avoiding recombination with holes that remain on TiO_2.

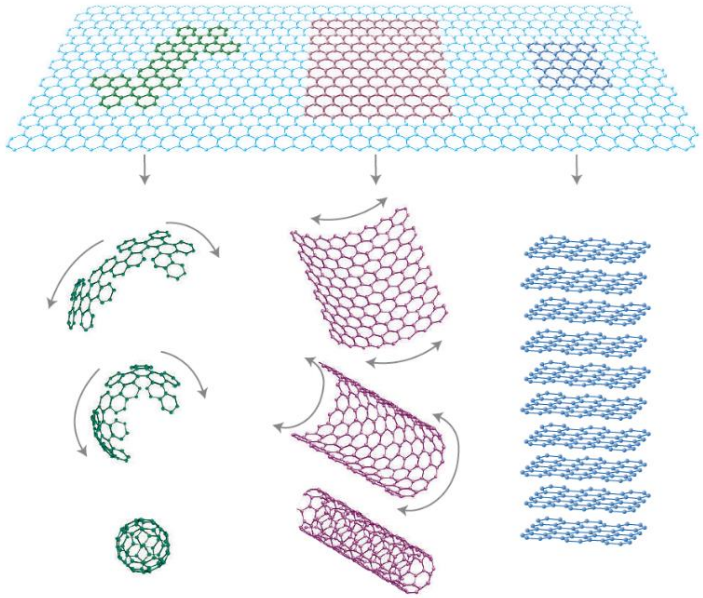

Figure 11: Single layer graphene, as a parent to other carbonaceous materials: 0D fullerenes, 1D nanotubes, and 3D graphite.[113]

2.3.1 Graphene Synthesis

Graphene can be synthesized using various methods. In order to produce single-layer or bi-layer graphene, micromechanical cleavage of highly oriented pyrolytic graphite, epitaxial growth, chemical vapour deposition, and arc discharge of graphite can be used.[119] For large-scale production of graphene, the aforementioned methods are not suitable. The most popular method for producing graphene is to reduce chemically exfoliated graphene oxide (GO).[120] The large-scale, facile synthesis of GO was first created by Hummers and is aptly named the Hummers method.[121]

The Hummers method involves the exfoliation and oxidation of a graphite precursor in order to form graphene oxide, a non-conductive and hydrophilic graphene sheet containing functionalities such as epoxides, alcohols, ketone carbonyls, and carboxylic groups. First, graphite powder is added to a solution containing concentrated sulfuric acid (H_2SO_4), sodium nitrate ($NaNO_3$), and potassium permanganate ($KMnO_4$) to oxidize and exfoliate the graphite. After this process is complete, the solution is slowly neutralized using water, and excess $KMnO_4$ is reduced using hydrogen peroxide (H_2O_2). This final solution is washed and centrifuged to obtain the final GO powder.

This method has since been modified to improve the quality of the prepared GO.[122] Specifically, $NaNO_3$ is no longer used in the oxidation process and the ratio of H_2SO_4 and $NaNO_3$ is changed. This not only improves the efficiency of the oxidation process, but also makes the synthesis process itself safer and easier to control. The method used in this thesis is based heavily on these methods.

2.3.2 Graphene-TiO_2 Composites

Graphene-TiO_2 composites are quickly growing in popularity due to the complimentary properties of each material.[7, 123-125] Because graphene can easily be produced from GO using a variety of reduction methods, composites likewise can be made using various experimental techniques. As mentioned earlier, graphene has the potential for providing certain benefits to pure TiO_2 photocatalysis:[123] i) the highly conjugated surface of graphene allows for preferential adsorption of aromatic compounds through π–π stacking;[116, 125, 126] ii) the addition of graphene has been shown to produce a red-shift in light absorption;[7, 116, 125] iii) and, the presence of two-dimensional graphene can improve the electrical conductivity of the overall material and act as an electron acceptor to reduce recombination.[116, 125, 127]

A qualification must be made to distinguish between true graphene-based composites and composites based on reduced GO (RGO). In the majority of synthesis methods, the complete reduction of GO is not possible and some oxygenated surface groups remain on GO – this type of GO is referred to as reduced GO (RGO).[124] Therefore, although GO is typically never fully reduced, for the sake simplicity the term graphene-TiO_2 is still used to refer to RGO-based TiO_2 composites.

Graphene-TiO_2 composites can be synthesized using various methods.[127] The UV-assisted reduction of GO onto TiO_2 is a simple method using the photocatalytic nature of TiO_2.[128] Reducing agents can also be used to reduce GO in the presence of TiO_2, including hydrazine[129], glucose[130], and even various solvents including water.[131] Hybridization of graphene and TiO_2 occurs through hydrogen bonding between the various functional groups of GO (for example, –OH and –COOH groups) and the surface of TiO_2. During reduction, the functional groups of

GO are removed and unpaired *p* electrons on the carbon atoms can bond with more free Ti atoms of TiO_2.[132] Hybridization is the basis for electronic contact between TiO_2 and graphene and allows for graphene to act as an electron acceptor, as mentioned earlier in this section.

Composites containing graphene and various types of TiO_2 have been synthesized to great effect in photocatalysis.[59, 60] Graphene has been hybridized with TiO_2 nanoparticles,[116, 133, 134] nanotubes,[135] nanowires,[136] nanorods,[137] and various mesoporous and hierarchical morphologies.[138-141] One aspect of graphene-TiO_2 composites that is gaining more interest is the nature of hybridization between the two materials. Theoretically, to be able to synthesis titanium structures that are wrapped in graphene would provide greater electrical contact than to synthesize graphene sheets that have titanium structures on their surface (Figure 12). Only several papers have been published concerning preferentially wrapping graphene around titanium structures.[142-145] In addition, only one paper has been published concerning graphene-wrapped hierarchical TiO_2 structures and in the area of li-ion battery research.[146]

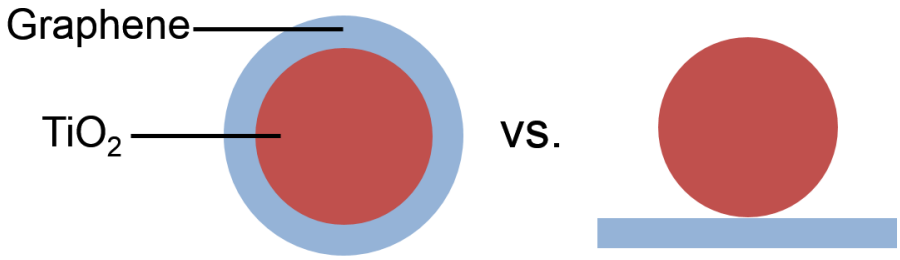

Figure 12: Diagram comparing graphene-wrapped TiO_2 and TiO_2 loaded on graphene. Graphene-wrapping maximizes the surface area of TiO_2 in contact with graphene.

Most importantly, to the best of my knowledge the wrapping of graphene around TiO_2 structures without pre-functionalization has yet to be achieved. Compounds such as poly(allylamine hydrochloride),[142] (3-aminopropyl) trimethoxysilane,[147] and aminopropyl-trimethoxysilane[148] has been used to amine functionalize TiO_2. This functionalization introduces a positive charge on the surface of TiO_2, making it more easily hybridized with GO, which is negatively charged. To remove the necessity of such chemicals would reduce synthesis costs and any health concerns associated with these functionalization compounds. Therefore, it is pertinent to determine whether graphene-wrapped hierarchical TiO_2 structures can be synthesized without need for amine functionalization for solution-based photocatalysis.

2.4 Summary

This section has covered the operating principles of photocatalysis and the basic attributes of a good photocatalyst. These attributes include chemical stability, high absorbance, high conductivity, and high specific surface area. A brief overview of photocatalytic systems are also discussed, as well as the use of MB as a model for the photodegradation of organic compounds. Background regarding TiO_2 as a photocatalytic material is given in greater detail, highlighting its crystal structure, large redox potential, and stability. The synthesis of TiO_2 is explained, detailing the various possible TiO_2 structures found in literature, including differences in morphology, doping, and heterostructuring. Lastly, graphene is introduced as a potential co-catalyst in photocatalysis. Graphene is used for its high surface area, high conductivity, and high absorptivity of aromatic compounds. Graphene can easily be hybridized with TiO_2 to form graphene-TiO_2 composites, with many examples in literature. Very few

literature has been found concerning graphene-wrapped TiO_2 as a specific means of hybridizing graphene-TiO_2, and no literature has been found regarding graphene-wrapped hierarchical TiO_2 structures without the use of pre-functionalization. The strong performance of these results warrants the synthesis of graphene-wrapped hierarchical TiO_2 as a potential photocatalytic material with further enhanced performance.

3.0 Characterization of Photocatalytic Materials

3.1 Scanning Electron Microscopy (SEM)

SEM is perhaps the most popular characterization technique for obtaining the topographical features and elemental composition of a material. This type of microscopy benefits from the use of electrons as opposed to conventional photons in optical microscopy. An optical microscope's ability to resolve the features of a specimen – or its resolution – is a function of the wavelength of light (λ) used and the microscope's numerical aperture (NA) via the Abbe diffraction limit (Equation 10). Based on this equation, current optical microscopes are intrinsically hindered by the wavelength of visible light (λ ≈ 400-750 nm), and in practice are able to achieve resolutions no better than 100 nm.[149]

$$d = \frac{\lambda}{2NA} \tag{10}$$

On the other hand, electron microscopes can achieve much higher resolutions using the concept that all matter has wave-particle duality. Louis de Broglie proposed this very thing in 1924, showing that the wavelength of a particle was inversely proportional to its momentum.[150] In his proposed relation (Equation 11), λ_{DB} is the de Broglie wavelength, h is the Planck constant, m_e is the rest mass of an electron, and E_b is the potential of the electron beam. Based on this equation, electrons with larger energy potentials – and therefore larger momentums – will have smaller wavelengths. Based on de Broglie's equation, a 1 eV electron with a rest mass of 0.511 MeV would have a de Broglie wavelength of 1.123 nm. SEMs are typically able to resolve features down to 1 nm in size.

$$\lambda_{DB} = \frac{h}{p} = \frac{h}{\sqrt{2m_e E_b}} \tag{11}$$

SEMs obtain an image via the following steps (Figure 13):[151] electrons are first thermionically emitted from an electron source, normally an electron gun consisting of a tungsten filament, inside a column. The electrons then form a beam that is accelerated by an applied potential (typically in the range of 0.2-40 kV) through the column and manipulated by condenser lenses. In the final objective lens, the electron beam is deflected along the *x* and *y* axes in order to provide a raster scan over a rectangular area of the sample. Because of the need for high beam accuracy, high vacuum conditions are necessary in order to remove particulate that could scatter the electron beam or compromise the sample being characterized. Once an electron beam strikes the sample, it interacts with the material through various scattering and absorption events, releasing secondary electrons, backscattered electrons, characteristic X-ray photons, and visible light photons. These signals are then caught by various detectors placed within the device and digitized into an image for viewing. The nature of these various signals is determined by their source, and is commonly described by the interaction volume of the electron beam (Figure 14).

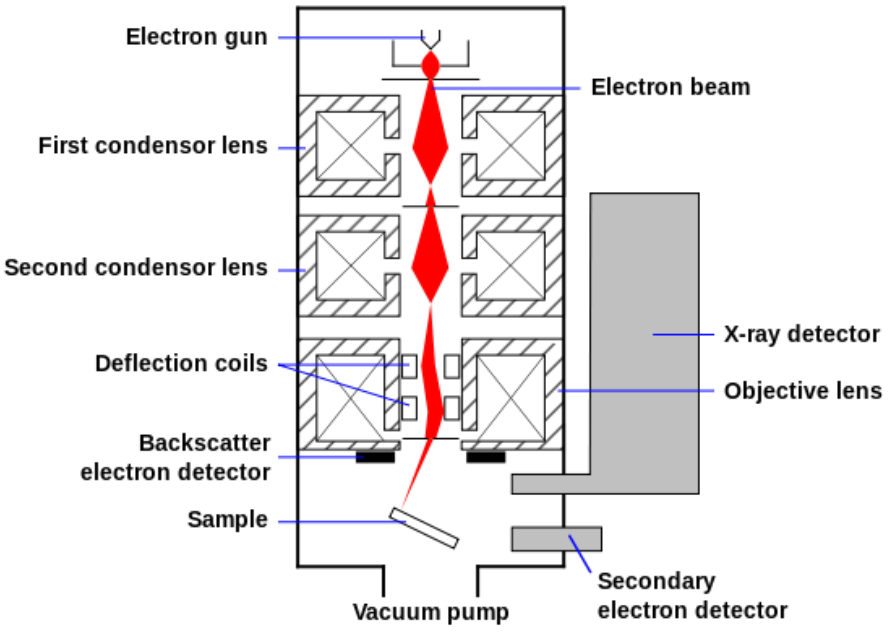

Figure 13: Diagram outlining the main components of an SEM. This work is attributed to Steff.

Secondary electrons are generated by incident electrons passing near an atom and ionizing a local electron in the atom with a much smaller kinetic energy. This ‘secondary’ electron is then ejected from the atom and caught by a detector. Secondary electrons are able to reveal topographical information about the sample because only secondary electrons near the surface of the sample have enough energy to leave the sample and be detected. Backscattered electrons are generated when incident electrons strike the nucleus of the atom in the sample and scatters back toward the column. The number of electrons that backscatter is directly proportional to the mass of the atom, meaning heavier elements appear brighter than lighter elements. Lastly, characteristic X-ray photons are generated when secondary electrons leave an inner shell of an atom. When a valence electron lowers its energy to fill the vacancy in the inner shell, energy

is released in the form of an X-ray. Because the energy of these X-rays are unique across different elements, this signal can be used to determine the elemental composition of a sample.

It is possible to perform elemental analysis on materials, however they are not reliable enough to give meaningful information concerning material composition of the materials used in this work. Therefore, we are only interested in verifying the morphology of our titanium oxide (TiO_2) and graphene-TiO_2 composite samples using SEM.

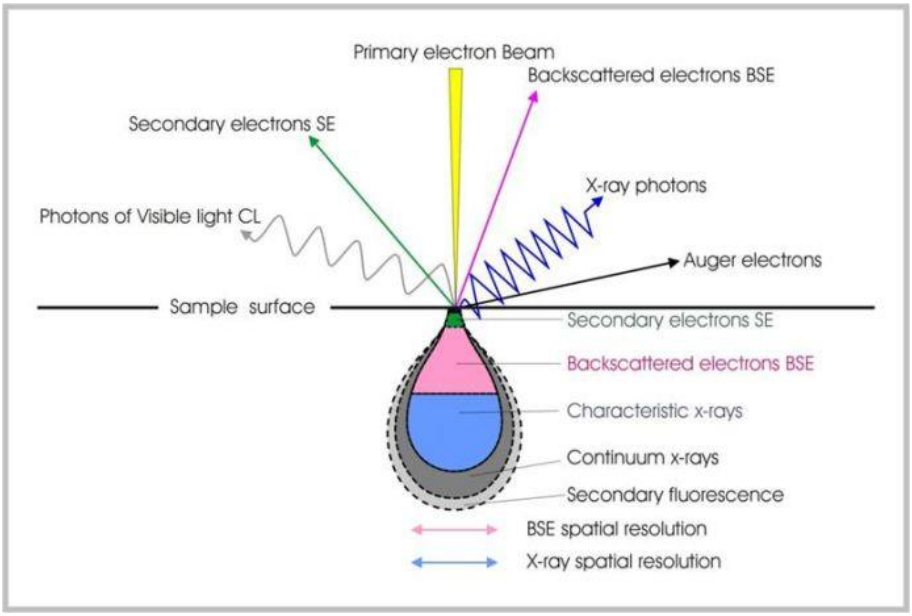

Figure 14: Interaction volume of an electron beam in SEM.[152]

3.2 Transmission Electron Microscopy (TEM) & Selected Area Electron Diffraction (SAED)

TEM is similar to SEM in the fact that they both rely on an electron beam to interact with a sample and produce images of the specimen. However, because TEMs require electrons to

transmit through the specimen being characterized, samples must be extremely thin in order to be appropriately imaged. Like an SEM, electron beams in TEMs are produced using an electron gun.[153] Electron beams are then manipulated using magnetic lenses and electrostatic fields. When electrons pass through the sample, they are projected onto a fluorescent screen and imaged using a high-resolution camera. In this way, thinner areas of the sample that allow for electron transmission appear brighter, while thicker or denser areas of the sample appear darker.

TEMs use much higher accelerating voltages than SEMs (typically 100 kV to 300 kV), leading to much smaller de Broglie wavelengths and sub-nanometer resolutions. This means that characteristics such as crystal structure and lattice spacing can be obtained – and even visualized – using a TEM.

By moving the focal plane of the electron beam from the imaging plane to the fluorescent screen, a diffraction pattern of the sample can be generated. When focused on a specific region of the sample, this diffraction pattern can give insight into the crystal structure and orientation of the sample. This technique is known as Selected Area Election Diffraction (SAED).

For this thesis work, TEM will be used to look at higher magnification images of the sample materials. Because TEM does not provide topographical information, it will be used to look at the general structure of TiO_2 and G-TiO_2. TEM will also be used to verify the lattice spacing that corresponds to the crystal structure of TiO_2 (using both the visual image and SAED pattern), and the number of layers of graphene wrapped around TiO_2.

3.3 X-Ray Diffraction (XRD)

XRD is a characterization technique that can ascertain the crystal structure of a material based on Bragg's model of diffraction (Equation 12). This model says that, given a crystal structure consisting of evenly-spaced crystal sheets (of lattice spacing *d*), incident light that diffracts off of each of these sheets will interfere constructively when the angle θ between the plane and the incident light results in a path-length difference equal to an integer multiple (n) of the wavelength of light (λ). All non-integer path-length differences will results in destructive interference, providing a unique XRD spectra for a material with a specific crystal structure.

$$2dsin\theta = n\lambda \tag{12}$$

X-rays are suitable light sources for obtaining this type of information because their wavelengths are on the same order of magnitude of the *d* spacing in crystals (1-100 Å). In normal operation, an X-ray source – such as a copper plate – is struck by an electron beam, generating X-rays.[154] These X-rays are then filtered into a single wavelength and collimated into a single direction before striking the sample. X-rays that elastically scatter off the sample hit a detector, which records the intensity of the signal as a function of incident angle θ. When the signal intensity of this constructive interference is plotted as a function of 2θ, an XRD spectrum can be obtained and compared against a database to determine its composition and crystal structure.

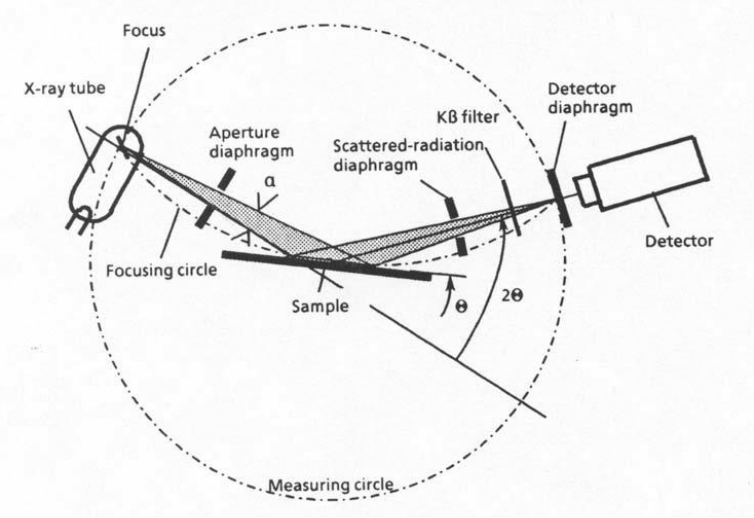

Figure 15: Illustration of XRD operating mechanism.[155]

XRD can also be used to estimate the crystallite size of a material based on the broadening of a peak in an XRD spectrum. The Scherrer equation (Equation 13) can be used to estimate the size of crystallites no greater than 0.2 μm in size.[156] Here, τ is the mean crystallite size, K is the shape factor (typically ≈ 0.9), λ is the X-ray wavelength, β is the line-broadening at the full width half maximum (FWHM), and θ is the corresponding Bragg angle.

$$\tau = \frac{K\lambda}{\beta cos\theta} \tag{13}$$

XRD will be main characterization technique for verifying the crystal structure and phase of TiO_2, as well as distinguishing the crystal structure of the hierarchical materials before and after heat treatment. XRD will also be used to estimate the crystallite size of TiO_2 and determine whether there is a change in size before and after hybridization with graphene.

3.4 Brunauer–Emmett–Teller (BET) Specific Surface Area Analysis

BET is not so much a characterization technique as it is a theory used to analysis surface area and pore analysis data.[157] BET theory is used to explain the physical adsorption of gas molecules on a surface as a means of determining a material's specific surface area. Specific surface area is typically expressed by the surface area divided by mass ($m^2 \cdot g^{-1}$) or by volume ($m^2 \cdot m^{-3}$, or m^{-1}).

BET theory builds upon the foundational Langmuir adsorption theory, which provides a model for monolayer molecular adsorption, and extends this theory to multilayer adsorption using three assumptions:

1. Gas molecules can adsorb on a solid surface in an infinite number of layers;
2. Individual adsorption layers do not interact with one another; and
3. Langmuir theory can be applied to each individual adsorption layer.

These three assumptions form the basis for the BET equation shown below (Equation 14):

$$\frac{1}{v[(\frac{p_0}{p}) - 1]} = \frac{c - 1}{v_m c}\left(\frac{p}{p_0}\right) + \frac{1}{v_m c} \tag{14}$$

where p_0 and p are the saturation and equilibrium pressure of adsorbates at a given temperature, v and v_m are the total adsorbed gas and monolayer adsorbed gas quantity, and c is the BET constant. By measuring the pressure and total gas adsorption at a given temperature, a plot showing $1/v[(p_0/p) - 1]$ vs. $\phi = p/p_0$ can be created. Finding the slope and y-intercept of this data allows the monolayer adsorption v_m and BET constant c to be calculated. Once these

values are found, the total specific surface can be derived based on the cross-sectional area of the adsorbate species and the mass of the sample used for characterization.

In this thesis work, BET will be used to determine the specific surface area of all materials, including the commercial reference (P25), the hierarchical TiO_2 nanoflowers, and G-TiO_2 composites. BET results may give further insight into how surface area effects overall photocatalytic performance and whether it is a large factor in determining high activity photocatalysts. Special provisions must be made when analyzing graphene-based samples, since graphene is known to reconfigure and collapse when heated to high temperatures. This reduces the surface area of graphene and causes the analyzer to underestimate the surface area of the material. In order to obtain BET data, graphene-based samples must be degassed at especially low temperatures.

3.8 Ultraviolet-Visible (UV-Vis) Spectroscopy

UV-Vis spectroscopy is a type of absorption spectroscopy that uses electron transitions within transition metal ions, conjugated organic molecules, and biological macromolecules to characterize their nature and abundance.[158] Specifically, this type of spectroscopy is useful for analyzing molecules containing π-electrons and non-bonding n-electron that can be excited from the highest occupied molecular orbital (HOMO) to the lowest unoccupied molecular orbital (LUMO). As the name suggests, UV-Vis spectroscopy covers both the ultraviolet and visible spectrums of light, but also part of the near-infrared spectrum (190-1100 nm).

A UV-Vis spectrophotometer operates by passing a beam of light through a cuvette holding the sample solution of interest (Figure 16). The machine then compares the intensity of light that transmits through the sample with the intensity of the initial beam of light to obtain the absorbance of the material. UV-Vis spectrophotometers use a dispersive method in that a monochromator is used to scan across single wavelengths at a time in order to produce a spectrum. When light strikes a sample, it is either reflected, transmitted, or absorbed. For this reason, a baseline, or reference, measurement containing only the solvent and cuvette must be taken to account for reflection that may occur due to these materials. Once this reference measurement is taken, it can be subtracted from subsequent sample measurements to produce an accurate spectrum of the sample's absorbance.

Beer-Lambert's law (Equation 15) states that the absorbance A of a sample in solution is directly proportional to the concentration c of the absorbing species within the solution and the path length L. (ϵ is a constant corresponding to the molar extinction coefficient of a compound.) Therefore, given a constant path length, a linear relationship between a compound's absorbance and its concentration can be obtained.

$$A = \epsilon c L \tag{15}$$

This property is extremely useful for measuring how the concentration of a compound in solution may vary with time. In photocatalytic degradation, UV-Vis spectroscopy can be used to record the decomposition (or decrease in concentration) of a target species during light

irradiation. In this work, UV-Vis spectroscopy will be used for this very purpose, measuring the reduction in methylene blue (MB) concentration over time as it is decomposed by TiO_2.

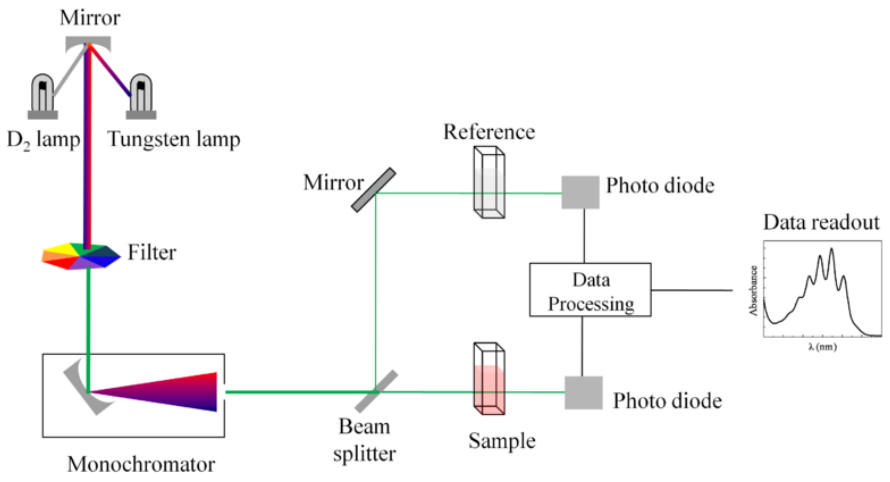

Figure 16: Illustration of the operating mechanism of a UV-Vis spectrophotometer.

3.8.1 Diffuse Reflectance UV-Vis Spectroscopy (DRS)

DRS is a specific type of UV-Vis spectroscopy that uses the same light spectrum to obtain not the change in transmittance of a sample but rather the change in reflectance.[159] Instead of passing a beam of light through a sample, light is reflected off the sample inside an integrating sphere. An integrating sphere is a hollow, spherical enclosure coated with highly diffuse reflective coating (Figure 17). When a light source enters an integrating sphere, its beam is diffused or integrated across the volume of the sphere. This diffusion preserves the light's original power but removes any spatial characteristics such as beam shape, direction, and position. An integrating sphere therefore provides much more accurate measurements of reflectance.

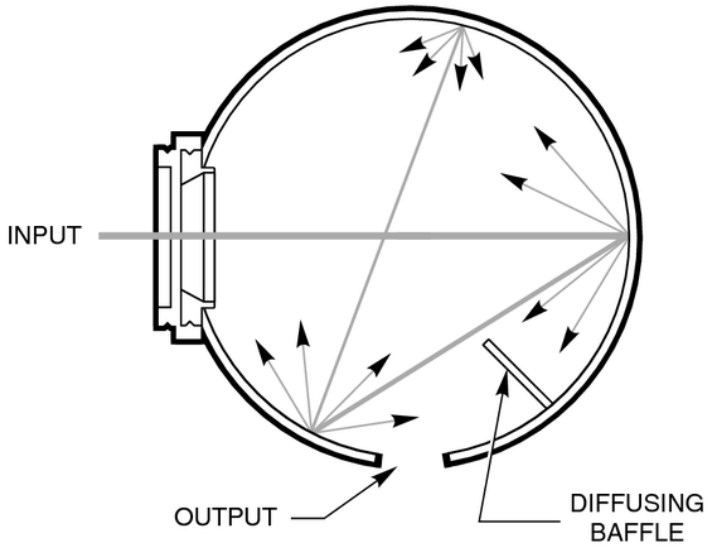

Figure 17: Operation mechanism of an integrating sphere used in diffuse reflectance UV-Vis spectroscopy.[160]

The improved accuracy of DRS is important in estimating the band gaps of materials. Diffuse reflectance data can be manipulated into a Tauc plot using the Kubelka-Munk transformation, given by:[161]

$$[h\nu \cdot F(R\infty)]^{1/n} = A(h\nu - E_g) \quad (16)$$

where h is the Planck constant, ν is the frequency of the light source, $F(R\infty)$ is a value proportional to the absorbance, A is a proportional constant, E_g is the band gap, and n signifies the nature of the electron transition. For anatase TiO_2, $n = 2$, denoting an allowed indirect transition. Once $[h\nu \cdot F(R\infty)]^{1/2}$ is plotted against $h\nu$, the linear region of the resulting graph can be extrapolated to the x-axis to estimate the band gap (expressed in $h\nu$) of the material.

DRS will be used to find the absorption spectrum of all photocatalytic materials, as well as estimate their band gaps. This information may confirm the visible light absorption of G-TiO_2 which may make G-TiO_2 a viable visible-light photocatalyst.

3.4 Fourier Transform Infrared Spectroscopy (FTIR)

FTIR is another type of absorption spectroscopy that measures the degree to which samples absorb and elastically scatter light over a range of wavelengths or frequencies.[162] FTIR devices do this by using a broadband light source – light containing all frequencies being measured – and a Michelson interferometer. A Michelson interferometer consists of an arrangement of mirrors that move in order to modify the spectrum of the light source (Figure 18). When a collimated, broadband light source strikes the beam splitter, it is split into two separate beams that each move toward a stationary mirror and a moving mirror. Once reflected off of the two mirrors, the two beams return to the beam splitter and recombine to strike the sample. Upon exiting the sample the beam is detected by a sensor and is recorded. As the non-stationary mirror moves, a difference in path-length of the two beams changes causing different frequencies to interfere destructively and constructively. Consequently, information regarding all frequencies is obtained simultaneously over the course of the experiment and integration time greatly increases. This technique differs from the dispersive method used in UV-Vis spectroscopy, which analyzes one wavelength at a time. The raw data obtained from the instrument is called an interferogram, and a Fourier transform operation must be applied to the data to create the final FTIR spectrum.

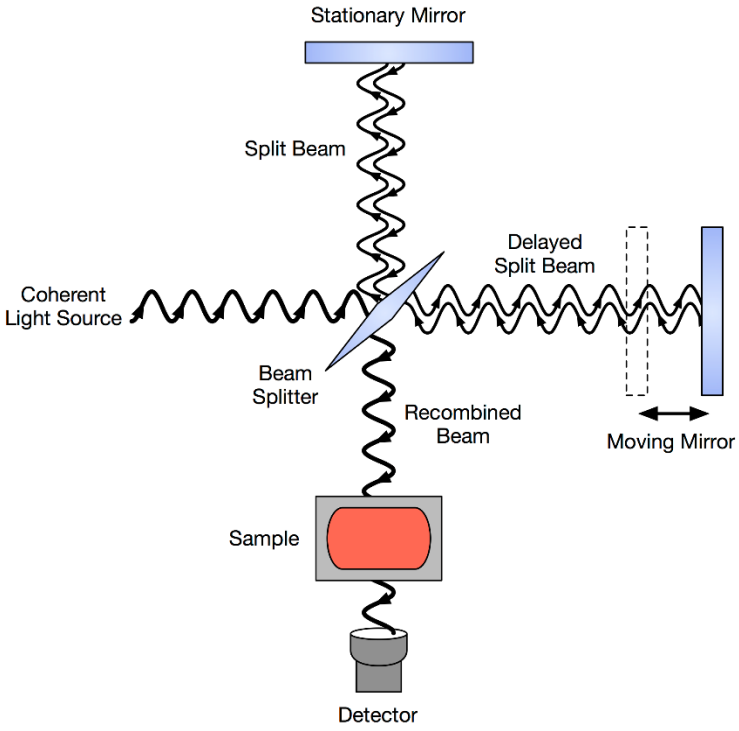

Figure 18: Mechanism behind a Michelson interferometer in FTIR.

FTIR takes advantage of the fact that many molecules absorb frequencies that are specific to their structure. Molecules absorb resonant frequencies, or frequencies that are equal to the vibrational mode of a bond or group. Because different molecular interactions have different masses and bonding energies – and therefore different resonance frequencies – FTIR can be used to determine if such interactions exist within a material.

It is important to note that FTIR is only able to detect vibrational modes that are IR-active, meaning that the vibration involves the change in the dipole moment of the bond or group. For example, symmetrical diatomic molecules (e.g. N_2) are not detected in the IR spectrum, while asymmetrical diatomic molecules (e.g. CO) are detected. This differs from Raman spectroscopy, which is described in Section 3.5.

In this work, FTIR is used mainly to confirm the existence of bonds that normally found in TiO_2 and carbon-TiO_2 composites. FTIR will also be used to explore the theory that band gap reduction in G-TiO_2 composites are due to the formation of Ti-O-C bonds which function as C-doped TiO_2.[163, 164] Unfortunately, the evaluation of these bonds depends on the sensitivity of the FTIR device, therefore it may not be possible to resolve such interactions even if they do exist.

3.5 Raman Spectroscopy

Raman spectroscopy operates on principles similar to that of FTIR spectroscopy and vibrational modes. However, unlike FTIR, Raman spectroscopy measures signals that undergo inelastic scattering when interacting with molecules.[165] Inelastic scattering of light occurs when the scattered light has an energy different from that of the incident light. This is due to the change in polarizability of the molecule during vibration which causes a change in the energy of the excited electron. This means that while a symmetrical molecule like N_2 is not IR active, it is Raman-active. In this same way, the symmetric stretch of CO_2 is Raman-active while the asymmetric stretch is IR-active. In the case of molecules that do not have a center of inversion (e.g. H_2O), it is possible for molecules to be active in both IR and Raman spectra.

There are six normal vibrational modes in molecules with centers of symmetry: symmetrical and anti-symmetrical stretching, scissoring, rocking, wagging, and twisting. Based on the previous discussion on IR and Raman-active modes, it can be determined that anti-symmetrical stretching, rocking, and wagging modes will be IR-active. On the other hand symmetrical

stretching, scissoring, and twisting modes are Raman-active. Again, it is of course possible for molecular modes to be both or neither IR and Raman-active, however this only occurs in molecules without a center of symmetry.

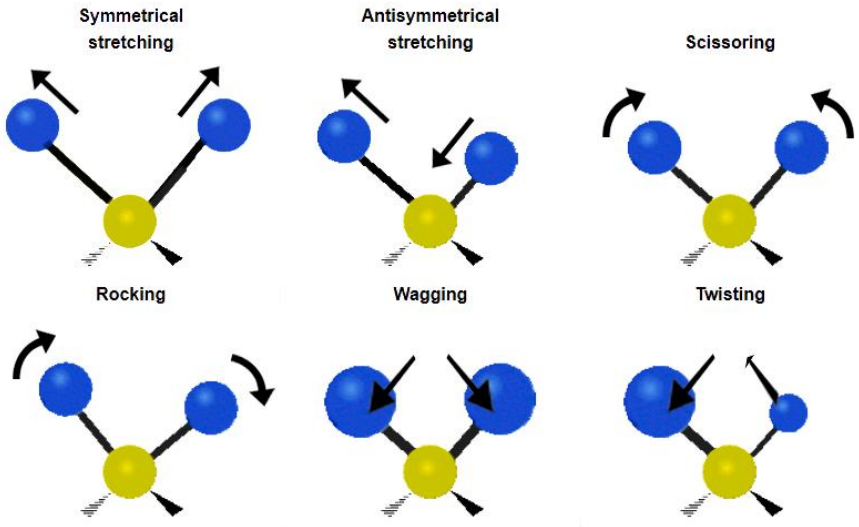

Figure 19: Examples of molecular modes found in molecules.

Raman spectroscopy will be used in this thesis as a complementary characterization technique to XRD: confirming the structure and phase of TiO_2. This technique will also be used to analyze the G-TiO_2 composites and the level of disorder within the graphitic material.[166] Unfortunately, the use of chemically reduced graphene oxide (GO) means that the reduced GO will exist in several layers. This means that the number of graphene layers in the G-TiO_2 composite cannot be determined using Raman spectroscopy.

3.7 Electrochemical Impedance Spectroscopy (EIS)

EIS, sometimes called dielectric spectroscopy, is a measure of a material's dielectric properties as a function of frequency. This technique is performed by applying an alternating voltage to an electrode interface and measuring the response for a range of frequencies.[167] When displayed as a Nyquist plot – plotting imaginary impedance $Z''(\Omega)$ vs. real impedance $Z'(\Omega)$ – EIS data can reveal information about the impedance and electrochemical behaviour of materials (Figure 20). Beginning at the high frequency response, the *x*-intercept of the data provides the series resistance of the entire electrochemical system. The size of the following semi-circle provides a measure of the charge transfer resistance of the material. This resistance is closely related to inter-particle resistance within the electrode.[168] At lower frequencies, the response enters into a 45° slope known is the Warburg diffusion regime. This regime corresponds to the Warburg impedance Z_W, which is a measure of the diffusion resistance of the electrochemical system.

In order to extract more quantitative results from EIS data, software is used to model the experimental data against equivalent circuits in order to estimate impedance values. This data will be used to confirm the differences in impedance and diffusion resistance between all photocatalytic materials. This work hopes to show that hierarchical TiO_2 can improve conductivity over that of nanoparticle TiO_2, and also that the addition of graphene can further improves the conductivity of TiO_2.

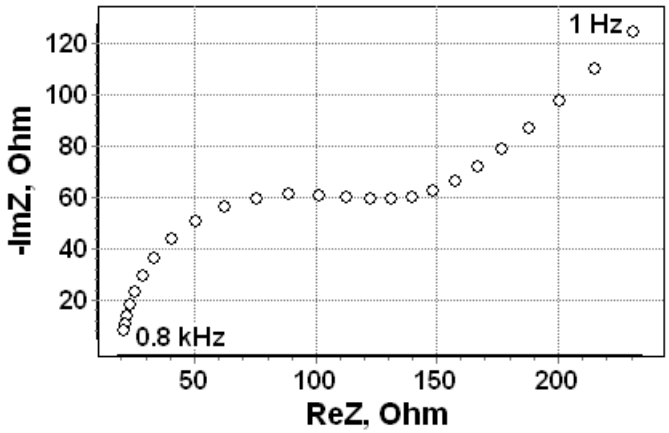

Figure 20: Example of a typical Nyquist plot.

4.0 Hierarchical TiO_2 Nanoflowers

The following section is based on previously published work[169] and is reproduced by permission from The Royal Society of Chemistry.

As mentioned previously, titanium dioxide (TiO_2) has become a widely studied semiconductor material in photocatalysis ever since its excellent photocatalytic properties were discovered by Fujishima and Honda in 1972.[2] The strong photocatalytic performance of TiO_2 is largely due to its high redox potential and appropriately positioned energy bands. Through the photo-generation of electrons-hole pairs, surrounding water molecules can be reduced and oxidized to form radical species capable of subsequent degradation of both organic and inorganic compounds. Therefore, photocatalytic materials such as TiO_2 have a promising future through the use of this mechanism and the sun's abundant source of radiation.

Various TiO_2 morphologies have been studied extensively, including micro- and nanoparticles,[170] nanotubes,[171] nanowires,[172] and hierarchical morphologies.[87, 173] Hierarchical materials are of great interest due to their ability to combine the light-scattering ability of larger particles with the high surface area of smaller particles.[87] In the absence of initial absorption, light scattering increases the probability that photons can still be absorbed by the material, while high surface areas increase the material's capacity for adsorption and subsequent degradation.[87] The use of specialized morphologies such as one and two-dimensional structures can be used to improve charge transfer, thus improving charge separation and reducing charge recombination.[174] The larger size of hierarchical morphologies also increases the ease of removal and recycling of the photocatalyst from solution. Flower-like structures are an example of hierarchical materials with large size, relatively large surface area, and the

effective use of one and two-dimensional nanostructures to aid charge transport. Some work has been done regarding flower-like structures and their related morphologies, and they have found great success in various applications. For example, Sun et al. has synthesized spherical dendritic structures consisting of nanorods, nanoribbons, and nanowires for lithium ion storage.[89] Liao et al. successfully synthesized flower-like morphologies consisting of nanorods and nanoparticles for use in dye-sensitized solar cells.[175] Wu et al. was able to synthesize F-doped flower-like TiO_2 structures consisting of short nanorods.[176]

This study reports the synthesis of hierarchical TiO_2 nanoflowers using a facile solvothermal method with significantly improved photocatalytic degradation of MB under UV irradiation. These TiO_2 nanoflowers are shown to improve upon commercial P25 performance by improving charge transport and reducing recombination rate, leading to an improvement of MB photodegradation over P25 by a factor of 1.49.

4.1 Experimental Methods & Characterization

TiO_2 nanoflowers were synthesized using a facile solvothermal reaction based on previous literature.[177] First, 1 mL titanium butoxide was added to 30 mL acetic acid. After stirring for 10 minutes, the solution was transferred to a 40 mL Teflon-lined stainless steel autoclave and heated to 140 °C for 12 h. The product was then centrifuged and washed several times with de-ionized water and ethanol to remove any residual reagents and solvents. After drying overnight at 60 °C, the resulting powder was annealed in air at 700 °C for 1 h to produce TiO_2.

A summary of this procedure, along with the procedure for the synthesis of G-TiO_2 composites and the RGO reference, is found in Section 5.1.

The morphologies and microstructures of materials were determined using field-emission scanning electron microscopy (FESEM, Zeiss ULTRA Plus; 10 kV acceleration voltage) and transmission electron microscopy (TEM, JEOL 2010F; 200 kV acceleration voltage), X-ray diffraction (XRD, Bruker AXS D8 Advance), and Raman spectroscopy (Bruker SENTERRA; 532 nm 20 mW laser). Moisture was removed from BET samples by first placing material in a vacuum oven at 100 °C overnight. In order to further remove moisture and impurities, samples were degassed at 80 °C for 300 min using He. Lower degassing temperatures were used to remain consistent with the temperature used for graphene samples – which were considerably more temperature sensitive.

Material performance was determined by the photocatalytic degradation of MB under UV light irradiation (500W Hg lamp, Beijing CEL Sci-Tech Co., Ltd). 30 mg of photocatalyst was added to a 40 mL MB aqueous solution (1.56 x 10-3 M) and stirred in the dark for 30 min to achieve adsorption-desorption equilibrium. Under irradiation, 1 mL sample solutions were drawn at 1, 2, 5, 10, 15, 20, and 30 min. After centrifuging to remove the photocatalyst, the concentration of MB was obtained using a UV-Vis photospectrometer (Fischer Scientific, GENESYS 10S). The absorbance was measured at the characteristic MB peak (664 nm) and data was reported as C/C_0, where C is the measured dye absorption at a given time interval and C_0 is the measured dye absorption of the solution at absorption-desorption equilibrium. DRS data was obtained using a diffuse reflectance UV-Vis recording spectrophotometer (Shimadzu Corporation UV-2501PC).

EIS of as-prepared samples were measured using an electrochemical workstation (Princeton Applied Research VersaSTAT MC) with a frequency ranging from 10 mHz to 1 MHz. The magnitude of the alternative signal was 5 mV. Glassy carbon was used as the working electrode with a material loading of 0.413 mg/cm3. EIS data was modelled using ZSimpWin data analysis software.

4.2 Results & Discussion

4.2.1 Structure & Morphology

SEM was used to investigate the morphology and microstructure of the synthesized TiO_2 nanoflowers (Figure 21). Before annealing the as-prepared material exists as a six-coordinated Ti-complex, $Ti_6O_6(Ac)_6(OBu)_6$, which has been discussed previously in the literature by Liao et al (Figure 21a and b).[175, 177] It has been proposed that TiO_2 nanoflowers are synthesized through the oriented growth of Ti-complex nanoparticles under high temperature and pressure. The oriented attachment of nanoparticles forms nanoribbons, which over time agglomerate together to form hierarchical spherical structures consisting of these nanoribbons. This hierarchical material is approximately 2–2.5 μm in diameter and has a flower-like morphology consisting of nano-ribbon 'petals'. Annealing causes the formation of anatase TiO_2 and the roughening of the nano-ribbon surface, which is due to the decomposition of the as-prepared Ti-complex into TiO_2.

The effects of this decomposition are seen in the annealed TiO_2 material (Figure 21c and d), which consists of small nanosheet and nanoparticle morphologies. TEM images gives greater

insight into the fine structure of the TiO_2 material (Figure 22) and better illustrate the hierarchical nature of the TiO2 nanoflower. Figure 22b provides a higher magnification of the 'petal' structures of the nanoflower. It can be seen that the petals vary in width (~10-50 nm) and consist of smaller nanoparticles.

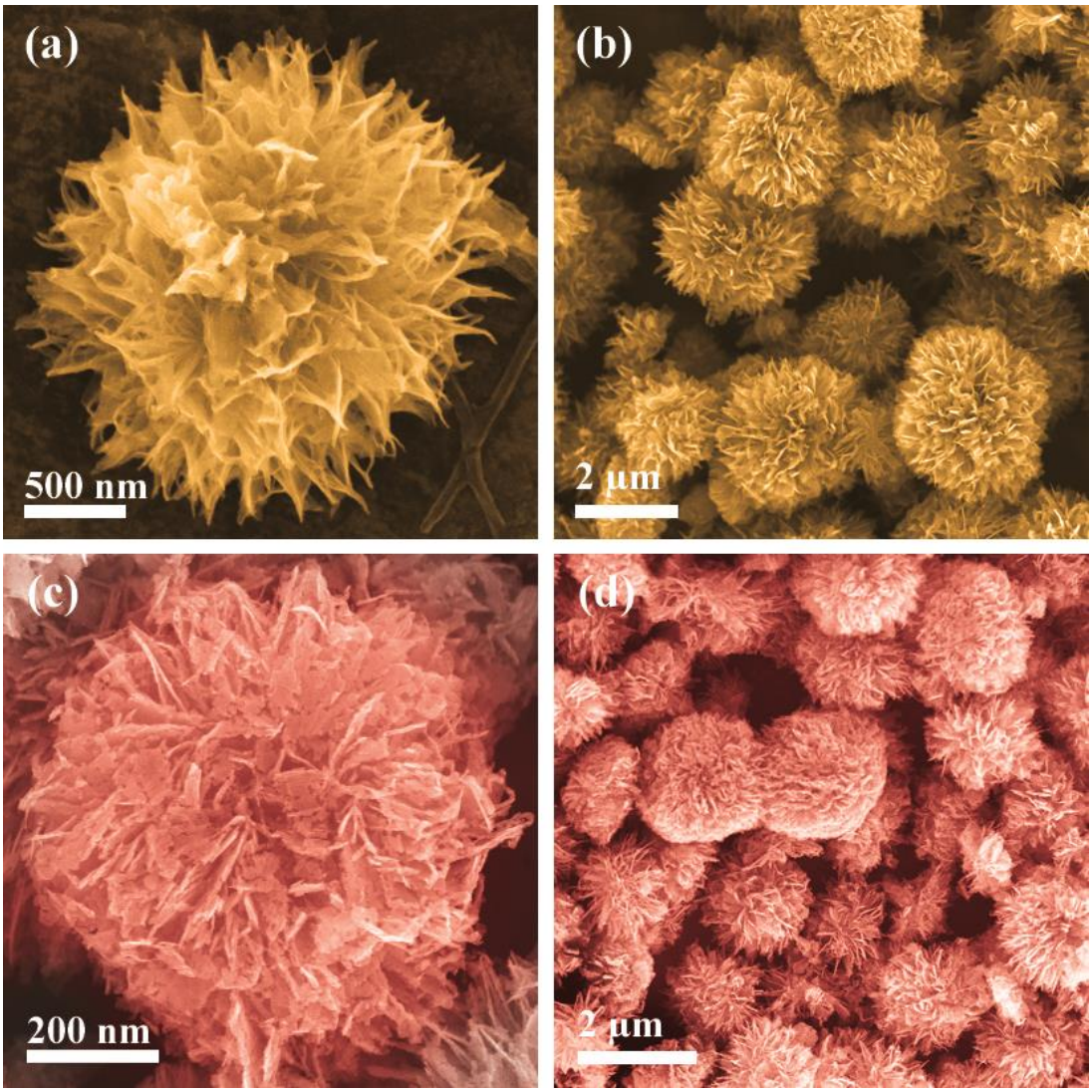

Figure 21: SEM images of as-prepared nanoflowers (a and b) and TiO_2 nanoflowers after annealing (c and d).

XRD was conducted using Cu K_α radiation with a wavelength of 1.54 Å. Figure 23a shows typical XRD patterns of the as-prepared nanoflower and annealed TiO_2 nanoflower. It can be seen that the as-prepared material is an unknown crystal structure of TiO_2, while annealing leads to the formation of a dominant anatase phase, marked by characteristic peaks at 25.5°, 38.0°, 48.2°, 54.1°, and 55.2°, and the formation of a rutile phase, as indicated by the characteristic peaks at 27.4°, 36.3°, and 69.0°.[178] Anatase TiO_2 has been known to transform into rutile TiO_2 anywhere in the range of 400 °C to 1200 °C,[69] and early formations of the rutile phase are often observed above 600 °C.[178, 179] Using the Scherrer equation, an average crystallite size of 28 nm is obtained for the annealed TiO_2 nanoflower.

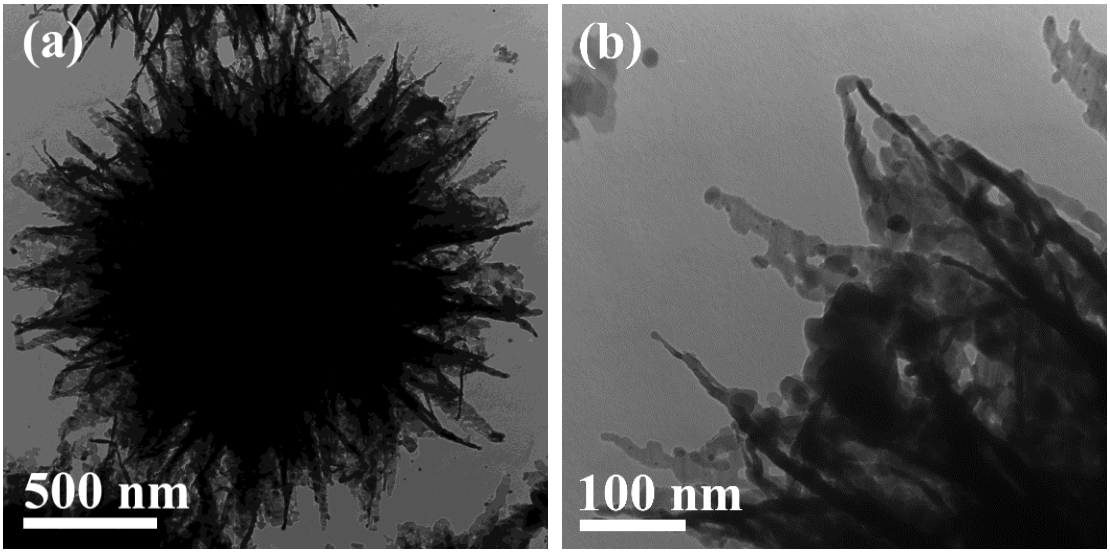

Figure 22: TEM of TiO_2 nanoflower (a) with a closer look at the nanoribbon 'petals' consisting of smaller nanoparticles (b).

Raman spectroscopy was also conducted to confirm the crystal phase of TiO_2 (Figure 23b). The spectrum for TiO_2 again confirms an anatase phase, with the characteristic E_g band at 150 cm^{-1}, 199 cm^{-1}, and 630 cm^{-1}, the B_{1g} band at 394 cm^{-1}, and the (A_{1g} + B_{1g}) mode centered at

509 cm^{-1}.[180] Each band is associated with a vibrational mode of TiO_2:[181] The E_g band is mainly associated with the symmetric stretching vibration of O-Ti-O; the B_{1g} is associated with the symmetric bending vibration of O-Ti-O; and, the A_{1g} band is associated with the anti-symmetric bending vibration of O-Ti-O. The peak at 449 cm^{-1} and shoulder around 613 cm^{-1} are assigned to the E_g and A_{1g} modes of the rutile phase, respectively, and are consistent with XRD results.[182]

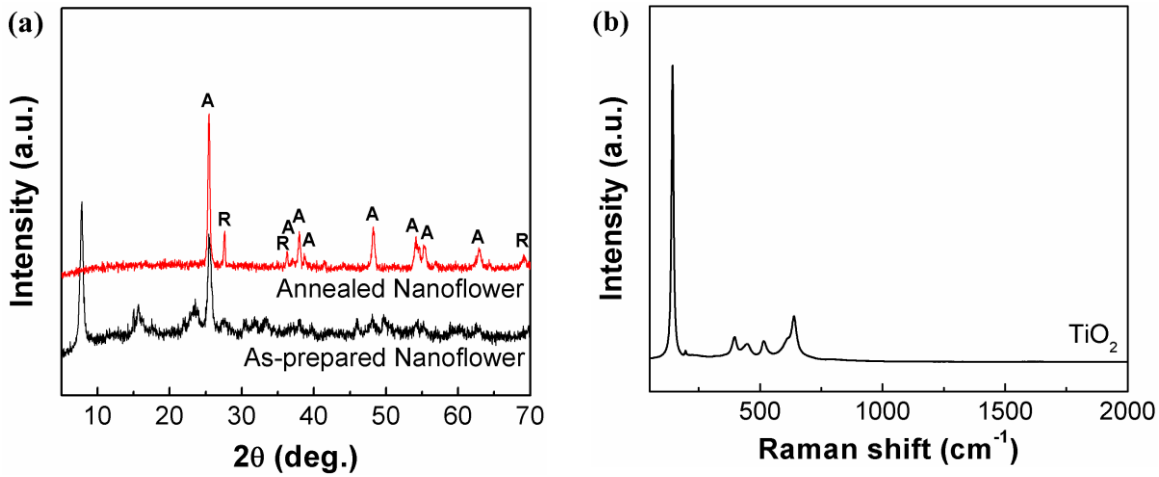

Figure 23: XRD spectra of as-prepared nanoflowers and anneal TiO_2 nanoflowers (a) and Raman spectra of TiO_2 nanoflowers after annealing (b).

4.2.2 Photocatalytic Performance

The photocatalytic activity of the TiO_2 nanoflower and P25 was determined through the degradation of methylene blue under UV irradiation. Figure 24a shows the normalized photodegradation of MB over 30 minutes of exposure using P25 and the TiO_2 nanoflower. It is shown that the TiO_2 nanoflower outperforms P25 in the photodegradation of MB. This is believed to be attributed to the hierarchical nature of the nanoflower morphology. The highly

crystalline nanosheet structure allows for fast charge transport, resulting in lower recombination rates compared to nanoparticle materials. A simple calculation of the first-order degradation rate constant, $k=-ln(C/C_0)/t$, gives a quantitative measure of this difference in photocatalytic performance. Dividing the rate constant by that of P25 also provides a quantitative measure of improvement over P25. k(P25) = 0.0620 min^{-1}, k(TiO_2 Nanoflower) = 0.0921 min^{-1}, showing that our TiO_2 morphology provides a ~49% increase in degradation rate. The change in the characteristic absorbance peak of MB (~664 nm) over time due to TiO_2 nanoflower photocatalysis is shown in Figure 24b. The decrease in the absorbance peak of MB relates to the decrease in MB concentration in the solution, and thus the decomposition of the target compound. As previously mentioned, the blue shift in the absorbance peak over time is due to the N-demethylation of MB as it undergoes attack from active oxygen species.[56]

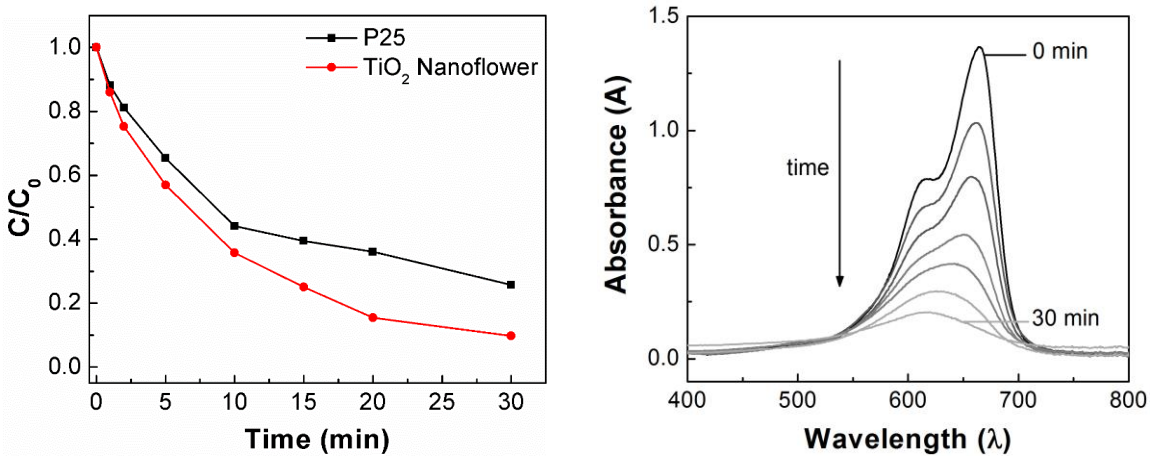

Figure 24: Photodegradation of MB under UV irradiation, comparing the performance of commercial P25 and TiO_2 nanoflowers. C is the measured dye absorption at a given time interval and C_0 is the measured dye absorption of the solution at absorption–desorption equilibrium (a). Change in the characteristics absorbance peak (~664 nm) of MB over time using TiO_2 nanoflower (b).

This further confirms its decomposition during photocatalysis. One should keep in mind that this relates only to the removal MB, and its structurally similar intermediates, from the solution. This is not necessarily indicative of the complete removal of all intermediate products in solution.

To better understand the difference in photocatalytic performance of P25 and the TiO_2 nanoflower, further characterization was conducted. Surface area measurements reveal that the TiO_2 nanoflower has a BET specific surface area of 16.4 $m^2 \cdot g^{-1}$ and an average pore size of 23.2 nm compared to a measured surface area of 46.1 $m^2 \cdot g^{-1}$ and pore size of 12.4 nm for P25 (Figure 34). The lower surface area of the TiO_2 nanoflower is expected, as annealing of the TiO_2 nanoflower at 700 °C causes strong sintering of particles and sheets which subsequently lowers surface area. This further suggests that the enhanced performance of the TiO_2 nanoflower is not due to an increase in surface area but rather improved charge transport properties.

EIS was performed on P25 and the TiO_2 nanoflower using a frequency range of 1 MHz to 10 mHz at an amplitude of 5 mV. A Nyquist plot of this data is shown in Figure 26, along with a Randles circuit used for impedance analysis. The different components in this circuit represent the electrochemical processes occurring at the electrode-electrolyte interface. The solution resistance (R_s) is determined by the *x*-intercept of the EIS curve and describes the overall resistance between the electrode and the electrolyte. The R_s value is consistently low between the two materials, with values of 31.2 $\Omega \cdot cm^{-2}$ and 35.7 $\Omega \cdot cm^{-2}$ for P25 and the TiO_2 nanoflower, respectively.

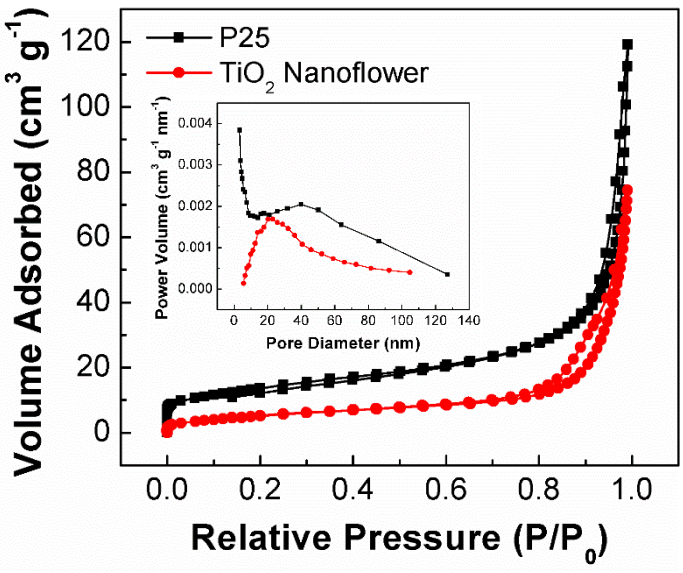

Figure 25: BET measurements of P25 and TiO_2 nanoflowers. Inset: pore size distribution of P25 and TiO_2 nanoflowers.

The region of interest is the semi-circle found at high frequencies corresponding to the interfacial charge-transfer resistance (R_{ct}). A smaller impedance arc radius corresponds to a smaller R_{ct}, and is clearly illustrated by our TiO_2 nanoflower and composite material in the Nyquist plot. Fitted values from impedance analysis verifies this observation with R_{ct} values of 160 $k\Omega \cdot cm^{-2}$ and 68.9 $k\Omega \cdot cm^{-2}$ for P25 and the TiO_2 nanoflower, respectively. The 45° slope found at the lower frequencies corresponds to the Warburg impedance (Z_W), and the length of this region determines the diffusion resistance of ions within the pores of the material. In this way, it can be seen that the TiO_2 has a slightly lower Warburg impedance than P25. The impedance analysis thus confirms the improved charge transfer and decreased ionic diffusion resistance of the TiO_2 nanoflower over commercial P25.

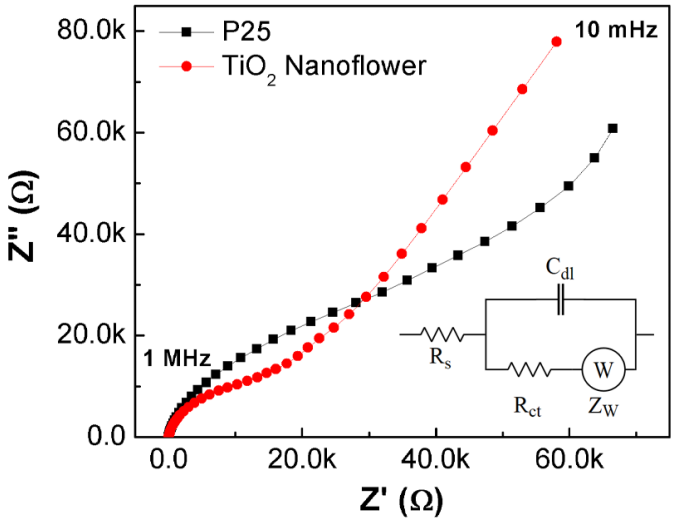

Figure 26: Nyquist plots of P25, the TiO_2 nanoflower. Inset: the Randles circuit model for impedance analysis: R_s is the solution resistance, C_{dl} is the double layer capacitance, and Z_W is the Warburg impedance.

Material absorption data was acquired using a diffuse reflectance UV-Vis recording spectrophotometer (Figure 27a). The TiO_2 nanoflower shows a small red-shift in absorption compared to commercial P25. This implies that the TiO_2 nanoflower is able to absorb more light closer to the visible-light spectrum. However, it should also be noted that P25 absorbs more strongly within the UV region. It is therefore unclear whether TiO_2 has a higher absorption efficiency than P25 across the entire absorption spectrum. A Kubelka-Munk transformation on the absorption data can be used to create a Tauc plot and estimate the band gap of each material.[161, 183] The Kubelka-Munk function, $[F(R\infty)h\nu]^{1/2}$, is approximated by $(\alpha h\nu)^{1/2}$ where α is the absorption coefficient and hν is the photon energy. A Tauc plot is generated by plotting $(\alpha h\nu)^{1/2}$ versus $h\nu$. By extrapolating a tangent line generated from the linear region of the curve to the *x*-axis, approximate band gaps of 3.0 eV and 2.9 eV can be found for P25, TiO_2 nanoflower, respectively.

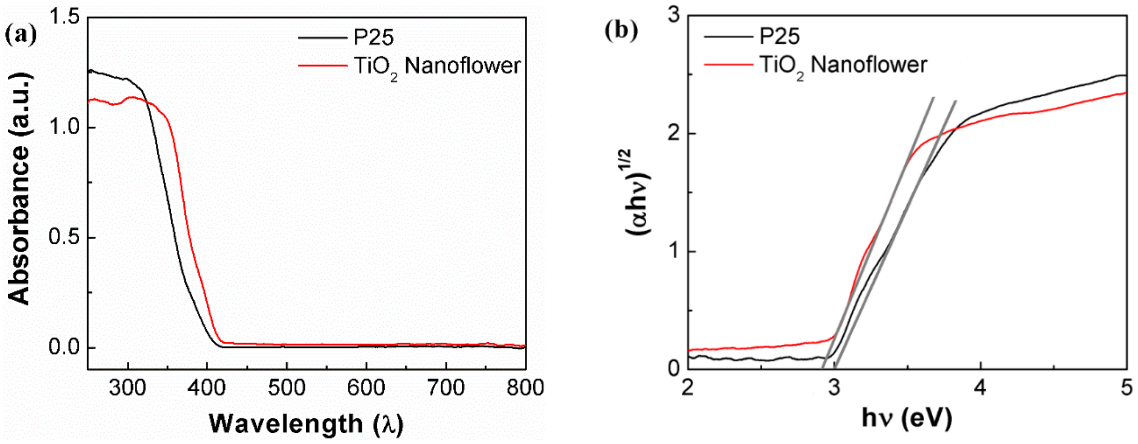

Figure 27: Absorbance spectra of P25 and the TiO_2 nanoflower (a), and band gap estimation using a Tauc plot (b).

4.3 Summary

TiO_2 nanoflowers were synthesized using a solvothermal reaction, and were annealed at 700°C to produce a TiO_2 material containing both anatase and rutile phases. These TiO_2 nanoflowers were shown to outperform P25 in the photodegradation of MB under UV irradiation by a factor of 1.49. BET and EIS show that, although the TiO_2 nanoflowers have a lower specific surface area than P25, they were able to improve photocatalytic activity on the basis of reduced charge transfer resistance and Warburg impedance. This is largely due to the hierarchical structure of the TiO_2 nanoflowers, which provides highly crystalline, two-dimensional structures that improve electron mobility within the material. This study confirms that hierarchical TiO_2 nanoflowers are a suitable candidate for UV-activated photocatalysis.

5.0 Graphene-Wrapped Hierarchical TiO_2 Nanoflowers

The following section is based on previously published work[169] and is reproduced by permission from The Royal Society of Chemistry.

It was shown in the previous study that hierarchical TiO_2 nanoflowers can be used in photocatalysis with improved photocatalytic activity. In order to further improve the performance of photocatalytic materials, composites consisting of TiO_2 and carbonaceous materials have been explored.[7] Carbonaceous materials such as carbon nanotubes,[184, 185] activated carbons,[186, 187] and graphene[188, 189] have been combined with TiO_2 to create composites with improved performance. Graphene in particular has been shown to provide several advantages to pure TiO_2 photocatalysis:[123] First, graphene consists of a highly conjugated planar surface which allows for preferential adsorption of aromatic compounds such as methylene blue (MB) through π–π stacking.[116, 125, 126] Second, the addition of graphene has been shown to cause a red-shift in the absorption spectrum leading to activation under visible-light irradiation.[7, 116, 125] Third, due to its high electron mobility, the presence of two-dimensional graphene greatly improves the charge transport properties of the overall material and reduces the rate of charge-carrier recombination.[116, 125, 127]

Graphene-wrapping of other materials is a more recent method for hybridizing graphene to form composites, and has found uses in Li-ion batteries,[142, 146] supercapacitors,[148, 190] fuel cells,[191] and solar cells.[192] This method of hybridization allows for an increased amount of contact between graphene and the photocatalyst, thus improving charge transport characteristics.[193, 194] Unfortunately, graphene wrapping of metal oxides often involves additional functionalization of the material surface which is an undesirable intermediate step.

The compounds used for this purpose, such as poly(allylamine hydrochloride),[142] (3-aminopropyl)trimethoxysilane,[147] and aminopropyltrimethoxysilane[148] are often toxic and unnecessarily detrimental to the environment. Little work has been done on graphene-wrapped TiO_2, and to the best of my knowledge graphene-wrapped TiO_2 hierarchical structures have not been studied. It is therefore desirable to achieve graphene hybridization of such structures using facile methods that do not require pre-functionalization.

This study reports the synthesis of graphene-wrapped hierarchical TiO_2 nanoflowers (G-TiO_2) using a facile hydrothermal method with significantly improved photocatalytic degradation of MB under UV irradiation. Prepared TiO_2 nanoflowers are intermixed with graphene oxide sheets and hydrothermally reduced to produce a graphene-wrapped TiO_2 composite. It is proposed that the modification of TiO_2 in this manner helps to improve photodegradation properties by increasing adsorption through π–π stacking of MB on graphene and improving electronic properties by accepting photo-generated electrons and further suppressing recombination. Therefore, this hierarchical morphology combines the unique properties of TiO_2 nanoflowers and the high surface area and conductivity of graphene.

5.1 Experimental Methods & Characterization

Graphitic oxide (GO) was synthesized from graphite powder using a modified Hummers method as described in previous work.[121, 122, 195, 196] In a typical synthesis, 360 mL H_2SO_4 and 40 mL H_3PO_4 were added to a 1 L Erlenmeyer flask in an ice bath while stirring. 2 g of graphite powder was then added to the flask and stirred for 30 min. 18 g of $KMnO_4$ was added slowly

over the course of several hours in order to begin the oxidation of graphite. After all $KMnO_4$ was added, the solution was heated to 50°C in an oil bath and stirred for 16 h. After this, the solution was again placed in an ice bath to allow the mixture to cool to room temperature. 460 mL DDI water was added drop-wise to the solution over the course of several hours to neutralize the mixture. During this reaction, the temperature of the solution was kept below 10°C. 20 mL of 30% H_2O_2 was then added to the solution drop-wise. Once the reaction was complete, the solution was centrifuged and washed with DDI water, 30% HCl, 50% ethanol, 5% HCl, and then DDI water again. The resulting material was frozen using liquid N_2 and freeze-dried to produce a dry GO powder.

In order to synthesize the G-TiO_2 composites, a certain amount of GO (2 mg to 20 mg to achieve approximate 1 wt%, 5 wt%, and 10 wt% graphene loadings) was dissolved in a solution containing 20 mL water and 10 mL ethanol, and sonicated for 1 h. The solution was then centrifuged at 6000 rpm for 5 min to remove any large sheets. TiO_2 nanoflower material was added and the solution was stirred for an additional 2 h to ensure the complete mixing of GO with TiO_2. The mixture was then transferred to an autoclave and heated to 120°C for 3 h to simultaneously bind the GO to the TiO_2 nanoflower surface and reduce GO to graphene. The final composites were centrifuged and washed several times with de-ionized water and dried overnight at 60°C. 1 wt%, 5 wt%, and 10 wt% composites were denoted as 0.01G-TiO_2, 0.05G-TiO_2, and 0.10G-TiO_2, respectively. For comparison, the reduction process was repeated without TiO_2 to produce reduced GO (RGO).

This procedure can be viewed in conjunction with the procedure for the synthesis of the TiO_2 nanoflower, as discussed in Section 4.1, below in Figure 28. This flow chart clearly illustrates

the individual syntheses of TiO_2 and RGO products and how TiO_2 materials can be introduced into a GO solution before reduction to form graphene-TiO_2 composites. Because of the simplicity of this process, it is possible that a variety of TiO_2 morphologies or even other metal oxides can be hybridized with RGO.

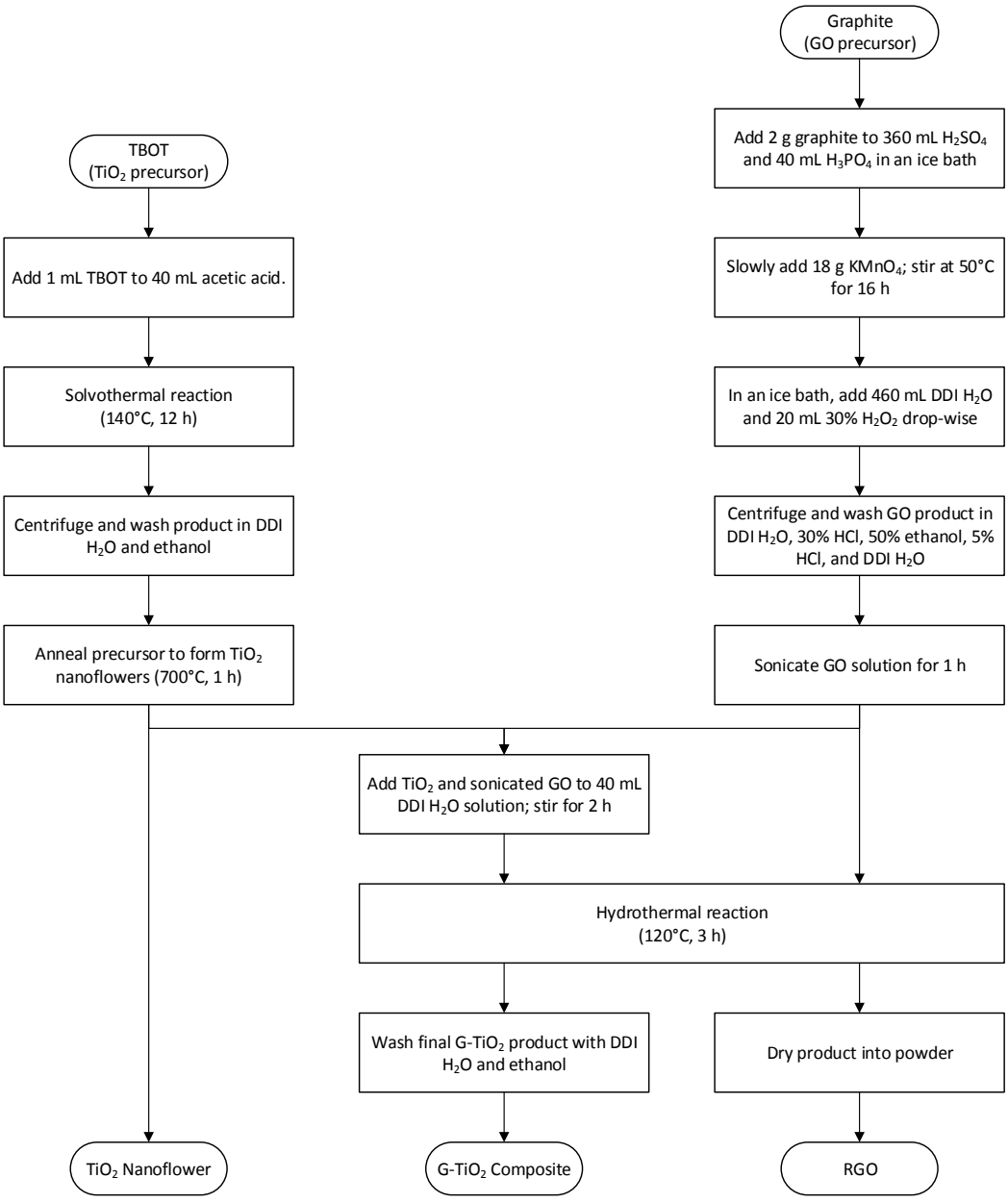

Figure 28: Flow chart outlining production of photocatalysts used in this thesis work.

Characterization was done in the same manner as previously found in Section 4.1. FTIR was performed using a Thermo Nicolet Avatar 320 FTIR spectrophotometer. Brunauer-Emmett-Teller (BET) specific surface areas were measured using a surface area and porosity analyzer (Micromeritics ASAP2020). Moisture was removed from BET samples by first placing material in a vacuum oven at 100 °C overnight. In order to further remove moisture and impurities, samples were degassed at 80 °C for 300 min using He. Lower degassing temperatures were used due to the temperature sensitivity the graphene samples.

5.2 Results & Discussion

5.2.1 Structure and Morphology

SEM was used to characterize the G-TiO_2 composites (Figure 29). After modifying the TiO_2 surface with graphene, the final composite material resembles a graphene-wrapped TiO_2 flower (shown in Figure 29c and d; the TiO_2 nanoflower precursor is shown in Figure 29a and b for reference) and implies that the reaction mechanism involves graphene loading around the TiO_2 material as opposed to TiO_2 loading on the graphene sheet.

Several reports have shown that the latter mechanism likely occurs when a titanium oxide precursor and GO are used as reagents,[139, 197, 198] while the former mechanism is possible when using prepared TiO_2 and GO as reagents.[146, 147, 193] In fact, when using TiO_2 and GO as reagents the loading mechanism is determined by the relative size of the materials, where smaller GO sheets tend to load onto larger TiO_2 particles and smaller TiO_2 particles tend to load onto larger GO sheets.[193] The wrapping of TiO_2 with graphene can therefore be explained by the

interaction of the –OH and –COOH functional groups of GO with the surface of TiO_2. During hydrothermal reduction the removal of these functional groups results in unpaired *p* electrons which more readily bind to the surface atoms of TiO_2.[147]

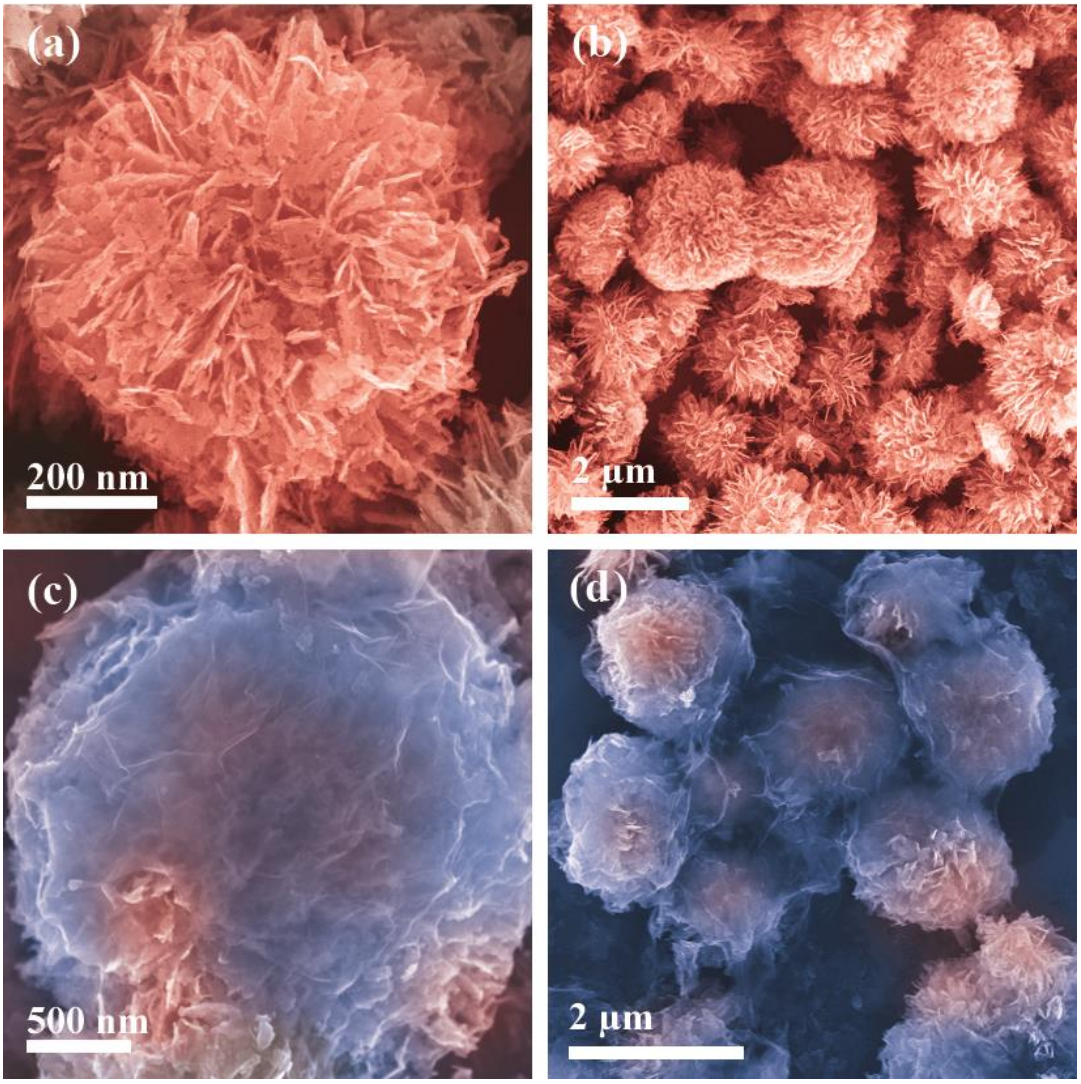

Figure 29: SEM images of TiO_2 nanoflowers before graphene hybridization (c and d) and G-TiO_2 after graphene hybridization using a hydrothermal reaction (c and d). In the images TiO_2 is highlighted as red, and graphene is highlighted as blue.

TEM images of the G–TiO_2 composite are shown in Figure 30. A close-up image of the graphene-wrapped flower edge and its respective specific area diffraction (SAD) pattern (Figure 30b and inset, respectively), along with the lattice spacing (d_{101} = 0.35 nm) observed in the HRTEM images (Figure 30c and d) clearly illustrating the anatase TiO_2 phase.

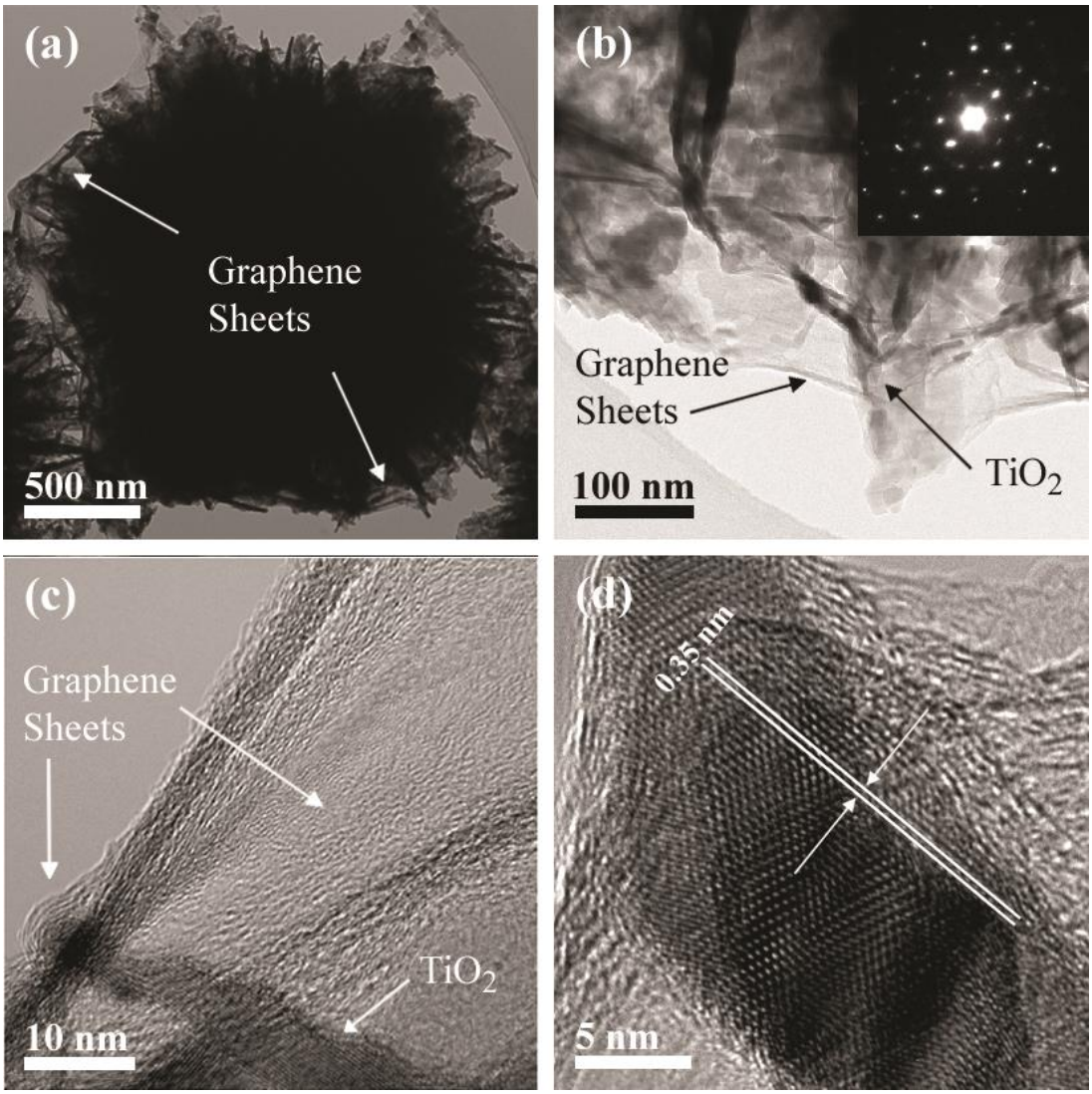

Figure 30: TEM images of a single G–TiO_2 composite (a), and a higher magnification image showing the graphene wrapped nanoflower structure (c); the inset shows the SAD pattern of the given region confirming the anatase phase. An HRTEM image of a single TiO_2 ribbon and wrapping graphene sheets (d), and the tip of a ribbon showing a TiO_2 lattice spacing of 0.35 nm corresponding to the (101) plane of anatase TiO_2.

The HRTEM images further verify the wrapping of graphene sheets around a TiO_2 'petal', and allow for an estimate of the number of graphene layers in the composite to be between five and seven.

Figure 31a shows typical XRD patterns of the G-TiO_2 composite alongside the as-prepared nanoflower and annealed TiO_2 nanoflower. There is no distinguishable difference between the TiO_2 nanoflower and G-TiO_2 composite materials. Calculation of the average crystallite size using the Scherrer equation shows that there is no noticeable change after hydrothermal reaction (~28 nm). In addition, the XRD pattern of G-TiO_2 shows that the graphene phase is not readily detected in the composite due to the low loading of graphene – which is in agreement with literature.[116] Raman spectroscopy was also conducted on the G-TiO_2 composite to further analyze the reduction and crystallinity of GO and reduced GO (RGO) (Figure 31b). As previously mentioned (Figure 23b), the Raman spectra of the nanoflower was confirmed to be predominantly anatase TiO_2 phase with several small rutile phase peaks. These rutile peaks are not readily seen in the G-TiO_2 spectra because the broad peaks mask these modes.

Further analysis of the carbonaceous materials in the range of 1000 cm^{-1} to 3500 cm^{-1} is shown in the inset of Figure 31b. The 1350 cm^{-1} and 1592 cm^{-1} peaks are assigned to the D and G bands, respectively.[199] The intensity ratio of the D band to the G band (I_D/I_G) is used to measure the degree of defects in the GO and RGO material and is also illustrated in the inset of Figure 4b. Before reduction, GO has a lower I_D/I_G ratio of 0.81, which implies that the initial material has a lower amount of defects present. Such low I_D/I_G values are uncommon but are still found in literature.[199] After hydrothermal reduction, the I_D/I_G ratio increases to 0.96. There are several

possible reasons for this. First, the reduction process was preceded by extensive sonication, which is known to reduce graphitic sheet size.[200] Second, the hydrothermal reduction process is also reported to increase fragmentation along reactive sites, leading to the formation of smaller sp^2 domains. Smaller sheet sizes lead to an increased amount of edges, which also act as defects and increase D band intensity.[132, 199, 201, 202] The 2D band around ~2700 cm^{-1} can be used to assess the number of layers in the graphene sheets.[166] Unfortunately, the chemical reduction of GO produces too many layers to be accurately evaluated using Raman. This is in agreement with TEM images, which shows the number of layers to be greater than 1-3 layers which are easily detected by Raman.

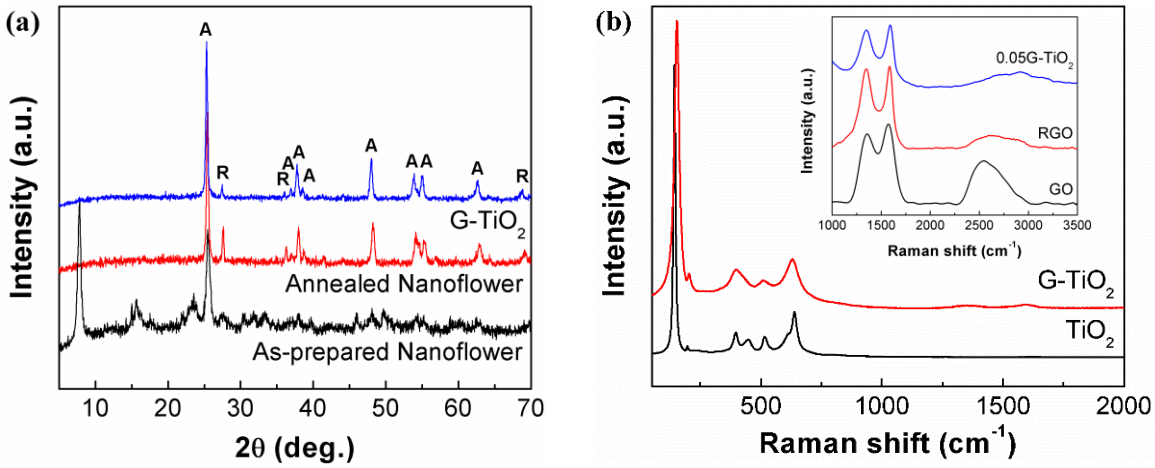

Figure 31: Comparison of G-TiO_2 and TiO_2 nanoflower XRD spectra (a); Comparison of G-TiO_2 and TiO_2 nanoflower Raman spectra. Inset shows D and G bands of GO, RGO, and 0.05G-TiO_2 (b).

5.2.2 Photocatalytic Performance

The photocatalytic activity of the G-TiO_2 composite was again determined through the degradation of methylene blue under UV irradiation. Figure 32a shows the normalized

photodegradation of MB over 30 minutes of exposure using 0.01G-TiO_2, along with P25 and the TiO_2 nanoflower for reference. Adding 1 wt% graphene to the TiO_2 nanoflower improves the rate constant *k* to 0.104 min^{-1}. This is a ~68% improvement over P25, and a small (~13%) improvement over the TiO_2 nanoflower.

Photocatalysis experiments using 0.01G-TiO_2, 0.05G-TiO_2 and 0.10G-TiO_2 were conducted to determine the effect of graphene loading on photocatalytic performance. The 0.01G-TiO_2 and 0.10G-TiO_2 composites were found to have rate constants of 0.104 min^{-1} and 0.168 min^{-1}, respectively, while 0.05G-TiO_2 provides the highest degradation rate constant of 0.211 min^{-1}. This optimal loading finds agreement in previous work,[163] where there exists a trade-off between reduced recombination and increased dye adsorption, and the reduction in available photocatalytic surface sites for the generation of electron-hole pairs and subsequent radical species.[135] The degradation rate of 0.05G-TiO_2 is an improvement on the performance of the un-modified TiO_2 nanoflower by a factor of 2.3, and P25 by a factor of 3.4.

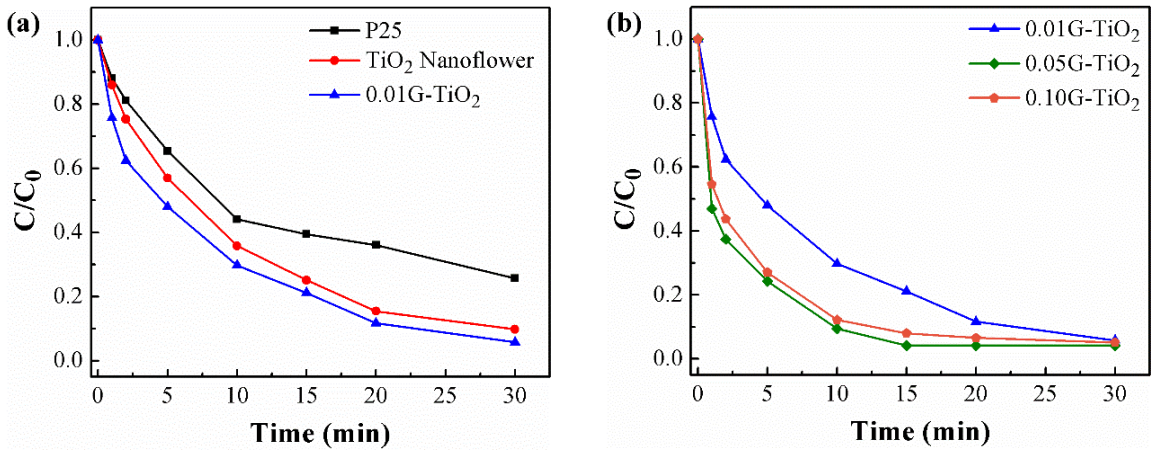

Figure 32: Photodegradation of methylene blue under UV irradiation, comparing the performance of commercial P25, the TiO_2 nanoflower, and 0.01G–TiO_2 (a) and 1 wt%, 5 wt%, and 10 wt% graphene loadings (b). C is the measured dye absorption at a given time interval and C_0 is the measured dye absorption of the solution at absorption–desorption equilibrium.

The change in the MB absorbance over time due to 0.05G-TiO_2 photocatalysis is shown in Figure 33. The change in the characteristic peak is similar to that of the TiO_2 nanoflower in Section 4, however the absorbance peak is significantly lower at t = 0 min. This is due to the strong initial absorbance of the graphene sheets that leads to a lower equilibrium concentration C_0. It can also be seen that the 0.05G-TiO_2 composite removes virtually all traces of MB by t = 30 min. It should again be clarified that the removal of MB does not imply the removal of all intermediate products. However, the reduction of almost all peaks by t = 30 min implies that all optically active intermediates have either been removed or are continually removed via photocatalysis.

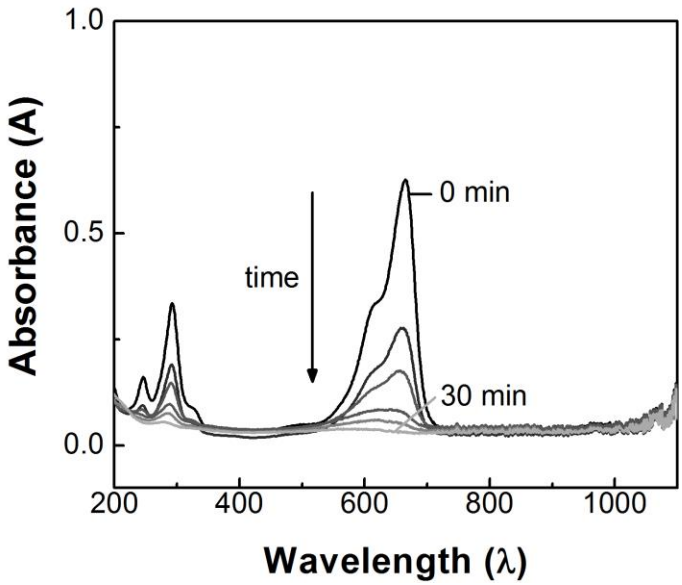

Figure 33: Change in the characteristic absorbance peak (~664 nm) of MB over time using 0.05G-TiO_2 composite (b).

The results of all experiments discussed so far can be combined into one table to compare the reaction rate constants of different materials and graphene loadings (Table 1).

Table 1: Rate constant calculations for data obtained from the photo-degradation of MB.

Sample	Rate constant *k* (min^{-1})	*k(i)/k(P25)*
P25	0.0620	n/a
TiO_2 Nanoflower	0.0921	1.49
0.01G-TiO_2	0.104	1.68
0.05G-TiO_2	0.211	3.40
0.10G-TiO_2	0.168	2.71

Surface area measurements were performed on the 0.05G-TiO_2 material in order to provide a point of comparison between the graphene-wrapped TiO_2 nanoflower and the previously studied TiO_2 materials (TiO_2 nanoflower and P25). Recall that the TiO_2 nanoflower was found to have a BET specific surface area of 16.4 m^2 g^{-1} and an average pore size of 23.2 nm. After wrapping with 5 wt% graphene, the surface area more than doubles (33.2 m^2 g^{-1}) while the average pore size reduces to ~15.6 nm (Figure 34). Measurements of pore volume also follow this trend in surface area.

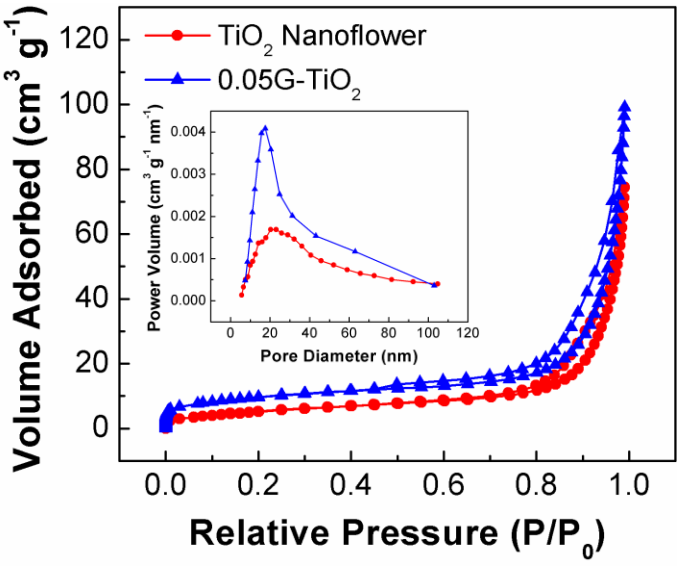

Figure 34: BET measurements of TiO_2 nanoflowers and 0.05G-TiO_2. Inset: pore size distribution of TiO_2 nanoflowers and 0.05G-TiO_2.

A summary of BET data is shown in Table 2. Wrapping with graphene causes a substantial increase in surface area and reduction in average pore size, which is understandably attributed to the high surface area and porosity of graphene. It is important to note that graphene does not readily participate in photocatalytic redox reactions like TiO_2. Therefore, the additional surface is much more likely to improve performance based on preferential methylene blue adsorption rather than by providing more total photocatalytic surface sites.

EIS was performed on the 0.05G-TiO_2 in a similar manner to P25 and the TiO_2 nanoflower, and a Nyquist plot of this data is shown in Figure 35. The R_s value is found to be consistent with that of P25 and the TiO_2 nanoflower. Fitted values from impedance analysis gave an R_{ct} value 38.9 kΩ cm^{-2} and the Warburg impedance was found to be much smaller than the other two materials.

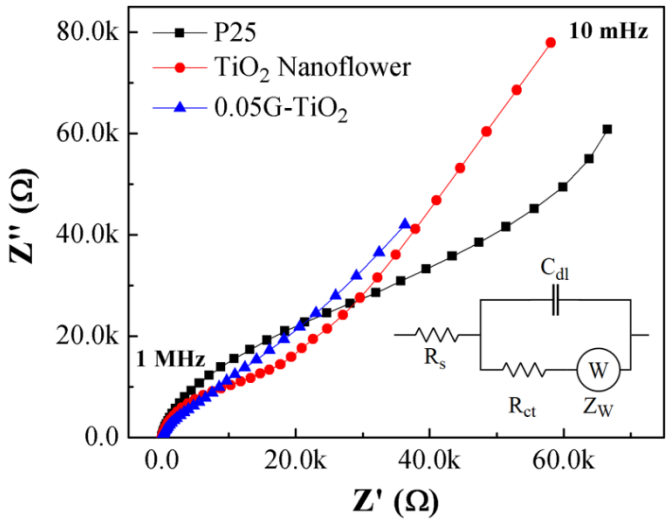

Figure 35: Nyquist plots of P25, the TiO_2 nanoflower, and 0.05G-TiO_2. Inset: the Randles circuit model for impedance analysis: R_s is the solution resistance, C_{dl} is the double layer capacitance, and Z_W is the Warburg impedance.

Table 2 provides a combined list of all relevant parameters for P25, the TiO_2 nanoflower, and 0.05G-TiO_2. It is therefore shown that the addition of graphene further improves performance by providing a highly conductive surface that allows for fast transport of injected electrons.

Material absorption data for 0.05G-TiO_2 was acquired using a diffuse reflectance UV-Vis recording spectrophotometer (Figure 36). The 0.05G-TiO_2 composite is shown to further extend the absorption of the TiO_2 nanoflower into the visible range, thus further increasing absorption efficiency across the entire UV and visible range. The addition of graphene not only increases the onset absorption wavelength of the composite but also provides background absorption across the entire visible light spectrum. This background absorption is likely due to the highly conjugated structure (and subsequent zero band gap) of graphene which makes it possible to absorb even lower energy light irradiation. This is further supported by observing the black physical appearance of graphene.

Using a Tauc plot, an approximate band gap of 2.6 eV can be estimated for 0.05G-TiO_2. It should be noted that the background absorption of graphene is not reflected in the band gap estimation because it does not provide onset absorption characteristics that would relay band gap information. Therefore, modification with graphene not only increases absorption in the UV range but also provides a red shift in absorption to higher wavelengths. Absorption over a wider spectrum can also lead to increased charge generation efficiency and subsequently increased potential radical generation and target degradation. This red shift is reported to be due to the Ti-O-C chemical bond, and is closely associated with the reduction in TiO_2 band gap due to carbon doping.[163, 164]

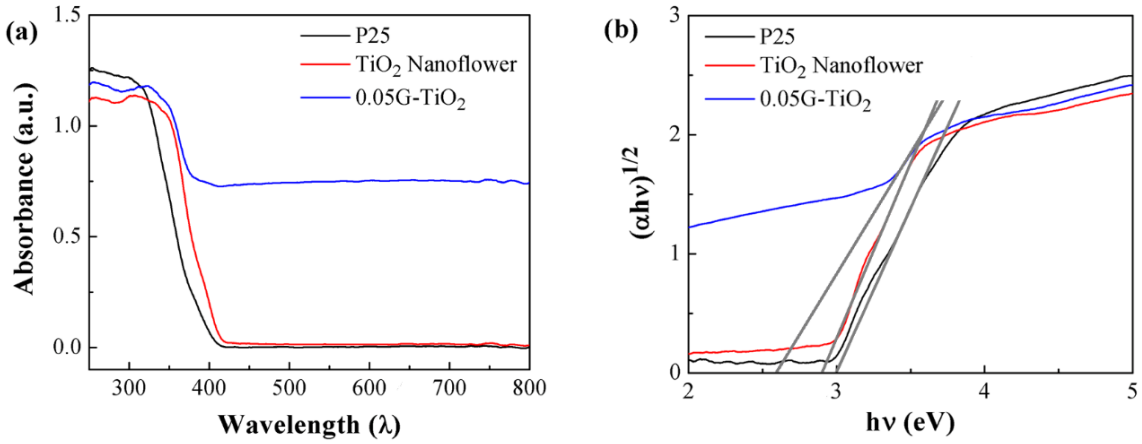

Figure 36: Absorbance spectra of P25, the TiO_2 nanoflower and 0.05G–TiO_2 (a), and band gap estimation using a Tauc plot (b).

Table 2: Surface analysis data and fitted values of EIS data modelled in ZSimpWin using a Randles circuit.

Sample	BET specific surface area (m^2/g)	Average pore diameter (nm)	Pore volume (cm^3/g)	R_s (Ω cm^{-2})	R_{ct} ($k\Omega$ cm^{-2})
P25	46.1	12.4†	0.179†	31.4	160
TiO_2 Nanoflower	16.4	23.2	0.116	35.7	68.9
0.05G-TiO_2	33.2	15.6	0.148	29.0	38.9

†Measured values using instrument. It should be noted that P25 is not a porous material.

FTIR was performed to investigate the functionality and interaction between TiO_2 and RGO and explore the possibility of a Ti-O-C chemical bond that could be responsible for band gap reduction in the G-TiO_2 composite (Figure 37). RGO shows peaks at 1718 cm^{-1} (C=O), 1577 cm^{-1} (skeletal vibration), 1399 cm^{-1} (C-OH), and 1246 cm^{-1} (C-O-C).[203] The TiO_2 materials share a common broad peak at ~3400 cm^{-1} (-OH) associated with the adsorption of water. The TiO_2 nanoflower also has a second peak at 1629 cm^{-1}, which is assigned to the binding vibration of the H-O bond.[204] The 0.05G-TiO_2 composite also shares this peak at 1617 cm^{-1}, however it is red shifted due to the presence of the skeletal vibration of RGO. The composite

also has two small additional peaks at 1265 cm^{-1} and 1061 cm^{-1}, which can be assigned to the C-O-C and C-O stretching vibration of RGO. Therefore, although other groups[164, 205] have reported Ti-O-C peaks at 1738, 1260, 1096, and 798 cm^{-1} which are also seen in our results, based on our data it is difficult to confirm the presence of this interaction due to their strong similarity to vibrational modes of RGO.

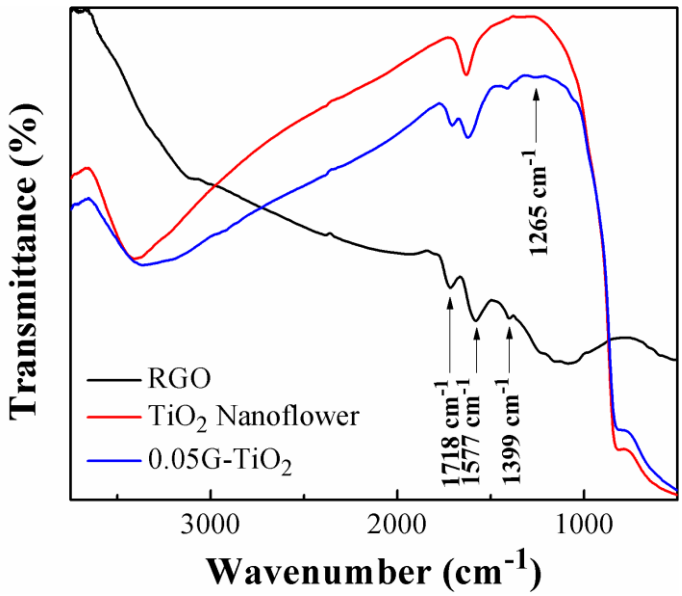

Figure 37: FTIR spectra of RGO, TiO_2 Nanoflower, and 0.05G-TiO_2.

However, the FTIR results do reveal that the addition of graphene to the TiO_2 nanoflower introduces negatively charged functional groups (i.e. –OH groups) and lowers its isoelectric point (the isoelectric point of TiO_2 is within the range of pH = 6 – 7.5).[193, 206, 207] The photocatalyst experiments are conducted at pH ~ 6.5. Given that MB is positively charged in solution,[53] it is expected that the negatively charged G-TiO_2 composite will attract positively charged MB more effectively than TiO_2. This in turn contributes to increased MB adsorption and degradation.

5.3 Summary

Graphene-wrapped TiO_2 nanoflowers were synthesized using a hydrothermal reaction without the use of pre-functionalization. These G-TiO_2 composites were able to further improve upon the photocatalytic activity of the TiO_2 nanoflower, and were shown to outperform P25 in the photodegradation of MB under UV irradiation by a factor of 3.4. BET reveals that the addition of graphene greatly increases the surface area and pore volume of the catalysts, providing more surface area for MB adsorption. EIS shows that the presence of graphene can greatly reduce intra and inter-particle resistance, as well as Warburg impedance. DRS also shows that the G-TiO_2 composites are able to reduce the overall band gap of the TiO_2 nanoflowers and extend absorption into the visible-light range. This implies that visible-light photocatalysis is possible with these composite materials. Lastly, FTIR gave insight to the possible reasons for the reduction in band gap, however these results cannot definitively show the existence of the interactions required to explain this reduction.

6.0 Conclusions and Future Work

In summary, the wrapping of graphene around flower-like TiO_2 using a simple synthesis method has been demonstrated to greatly enhance the photocatalytic activity of TiO_2 when compared to commercial P25. In doing so, this thesis fulfills the objective presented, that is: (i) explore and verify the merits of hierarchical TiO_2 structures over normal TiO_2 nanoparticles; and, (ii) show the enhanced photocatalytic activity of TiO_2 via the specific heterostructuring of TiO_2 with graphene to form graphene-wrapped TiO_2.

In the first study, hierarchical TiO_2 nanoflowers were synthesized using a solvothermal reaction. The flower structures were shown to consist of smaller nanoribbon and nanoparticle morphologies. This TiO_2 nanoflower material was shown to outperform P25 by a factor of 1.49. Using BET and EIS analysis, this improvement is on the basis of improved charge transport along the hierarchical structure as opposed to increased surface area. DRS showed that the TiO_2 nanoflower had a slightly smaller band gap than P25.

In the second study, the graphene-wrapped hierarchical TiO_2 nanostructures show greatly improved performance in the photo-degradation of MB under UV irradiation. This improved performance should be ascribed to the ability of graphene to increase conductivity, suppress recombination, and provide additional, preferential adsorption sites for MB. The optimal graphene loading was found to be 5 wt% and is attributed to a balance between the improved conductivity and adsorption of graphene and the reduction in photocatalytic surface sites of TiO_2.

Despite the strong performance of the graphene-wrapped TiO_2 described in this work, additional work should be conducted in order to further verify and improve current results. Based on the results obtained from these experiments, the following future work is recommended:

1. Confirm the visible-light activity of graphene-wrapped TiO_2 nanoflowers by performing visible-light photocatalysis and comparing activity with commercial P25 under the same conditions. This is an important step in verifying whether this graphene-TiO_2 composite is a suitable photocatalyst for real-world conditions under solar irradiation.
2. Investigate the feasibility of graphene-wrapping other hierarchical materials, including non-TiO_2 photocatalytic materials, using similar experimental techniques; evaluate their performance. The nanoflower morphology is just one type of hierarchical material. Other hierarchical TiO_2 materials have also been synthesized with promising photocatalytic performance. In addition, novel non-TiO_2 photocatalytic materials may prove to be even better suited for graphene hybridization and should therefore also be explored.
3. Determine whether (flexible) films or membranes can be made from graphene-wrapped TiO_2 nanoflowers or similar materials to provide a practical candidate for higher throughput treatment of waste-water and other pollutants. Batch processes are typically impractical for waste-water remediation, and continuous processes with highly accessible catalysts are more desirable configurations.
4. Synthesize tri-phasic structures by including a third material in the composite. This material may include plasmon resonance noble metals or small band gap

semiconductors for charge-carrier transfer and visible light sensitization. Adding additional phases to the photocatalyst can not only increase absorption of the solar spectrum, but also improve control over charge-carrier movement, reducing recombination and improving photocatalytic efficiency.

5. Determine the activity of graphene-wrapped TiO_2 nanoflowers in other photocatalytic applications. Specifically, use the composite material in a hydrogen production system, and evaluate the efficiency under both electrolysis and photocatalytic (artificial and solar) conditions. These experiments can evaluate the ability of this composite to catalyze other redox reactions other than the ones discussed in this work and expand the usefulness of such a material to different applications.

This thesis work has provided a strong foundation for further research in photocatalytic materials. Future research should include: the extension of research scope into novel photocatalytic materials; the synthesis and evaluation of visible and/or infrared-light activated photocatalysts under solar-simulated light; and, the expansion of photocatalytic systems into other application areas such as hydrogen production systems and integrated solar fuel cell systems. The goal of this future research is to use these foundational concepts in photocatalyst synthesis and testing to eventually create practical real-world applications in clean and renewable technologies.

References

1. *Canada's Emissions Trends*; Environment Canada: 2013; pp 15-16.

2. Fujishima, A.; Honda, K., Electrochemical Photolysis of Water at a Semiconductor Electrode. *Nature* **1972,** *238* (5358), 37-38.

3. Fujishima, A.; Rao, T. N.; Tryk, D. A., Titanium dioxide photocatalysis. *Journal of Photochemistry and Photobiology C: Photochemistry Reviews* **2000,** *1* (1), 1-21.

4. O'Regan, B.; Graetzel, M., A low-cost, high-efficiency solar cell based on dye-sensitized colloidal TiO2 films. *Nature* **1991,** *353*, 737-740.

5. Li, X.; Shen, B.; Xu, C., Interaction of titanium and iron oxide with ZSM-5 to tune the catalytic cracking of hydrocarbons. *Applied Catalysis A: General* **2010,** *375* (2), 222-229.

6. Gueymard, C. A., The sun's total and spectral irradiance for solar energy applications and solar radiation models. *Solar Energy* **2004,** *76* (4), 423-453.

7. Leary, R.; Westwood, A., Carbonaceous nanomaterials for the enhancement of TiO2 photocatalysis. *Carbon* **2011,** *49* (3), 741-772.

8. Chen, X.; Li, C.; Gratzel, M.; Kostecki, R.; Mao, S. S., Nanomaterials for renewable energy production and storage. *Chem. Soc. Rev.* **2012,** *41*, 7909-7937.

9. Liu, G.; Wang, L.; Yang, H. G.; Cheng, H.-M.; Lu, G. Q., Titania-based photocatalysts-crystal growth, doping and heterostructuring. *J. Mater. Chem.* **2010,** *20* (5), 831-843.

10. Takahashi, K.; Yoshikawa, A.; Sandhu, A., *Wide Bandgap Semiconductors: Fundamental Properties and Modern Photonic and Electronic Devices*. Springer London, Limited: 2007.

11. Viswanathan, B.; Sivasanker, S.; Ramaswamy, A. V., *Catalysis: Principles and Applications*. Narosa Publishing House: 2002.

12. Hoffmann, M. R.; Martin, S. T.; Choi, W.; Bahnemann, D. W., Environmental Applications of Semiconductor Photocatalysis. *Chemical Reviews* **1995,** *95* (1), 69-96.

13. Murzin, D. Y.; Salmi, T., *Catalytic Kinetics*. Elsevier Science: 2005.

14. Davis, A. P.; Huang, C. P., The photocatalytic oxidation of sulfur-containing organic compounds using cadmium sulfide and the effect on CdS photocorrosion. *Water Res.* **1991,** *25* (10), 1273-1278.

15. Wu, L.; Yu, J. C.; Fu, X., Characterization and photocatalytic mechanism of nanosized CdS coupled TiO2 nanocrystals under visible light irradiation. *J. Mol. Catal. A: Chem.* **2006,** *244* (1–2), 25-32.

16. Adeli, B.; Taghipour, F., A Review of Synthesis Techniques for Gallium-Zinc Oxynitride Solar-Activated Photocatalyst for Water Splitting. *ECS Journal of Solid State Science and Technology* **2013,** *2* (7), Q118-Q126.

17. Sutton, A. P., *Electronic Structure of Materials*. Clarendon Press: 1993.

18. Levinson, J.; Shepherd, F. R.; Scanlon, P. J.; Westwood, W. D.; Este, G.; Rider, M., Conductivity behavior in polycrystalline semiconductor thin film transistors. *J. Appl. Phys.* **1982,** *53* (2), 1193-1202.

19. Zou, Z.; Ye, J.; Sayama, K.; Arakawa, H., Direct splitting of water under visible light irradiation with an oxide semiconductor photocatalyst. *Nature* **2001,** *414* (6864), 625-627.

20. Parlett, C. M. A.; Wilson, K.; Lee, A. F., Hierarchical porous materials: catalytic applications. *Chem. Soc. Rev.* **2013,** *(pre-print)*, -.

21. Zhu, J.; Zäch, M., Nanostructured materials for photocatalytic hydrogen production. *Current Opinion in Colloid \& Interface Science* **2009,** *14* (4), 260 - 269.

22. Qu, Y.; Duan, X., Progress, challenge and perspective of heterogeneous photocatalysts. *Chem. Soc. Rev.* **2013,** *(pre-print)*, -.

23. Carp, O.; Huisman, C. L.; Reller, A., Photoinduced reactivity of titanium dioxide. *Prog. Solid State Chem.* **2004,** *32* (1–2), 33 - 177.

24. Daneshvar, N.; Salari, D.; Khataee, A. R., Photocatalytic degradation of azo dye acid red 14 in water on ZnO as an alternative catalyst to TiO2. *Journal of Photochemistry and Photobiology A: Chemistry* **2004,** *162* (2–3), 317-322.

25. Kumar, R.; Kumar, G.; Umar, A., ZnO nano-mushrooms for photocatalytic degradation of methyl orange. *Mater. Lett.* **2013,** *97* (0), 100-103.

26. Kormann, C.; Bahnemann, D. W.; Hoffmann, M. R., Environmental Photochemistry - Is Iron-Oxide (Hematite) an Active Photocatalyst - a Comparative-Study - Alpha-Fe2o3, Zno, Tio2. *Journal of Photochemistry and Photobiology a-Chemistry* **1989,** *48* (1), 161-169.

27. Baltrusaitis, J.; Hu, Y.-S.; McFarland, E. W.; Hellman, A., Photoelectrochemical Hydrogen Production on α-Fe2O3 (0001): Insights from Theory and Experiments. *Chemsuschem* **2014,** *7* (1), 162-171.

28. Sayama, K.; Yoshida, R.; Kusama, H.; Okabe, K.; Abe, Y.; Arakawa, H., Photocatalytic decomposition of water into H2 and O2 by a two-step photoexcitation reaction using a WO3 suspension catalyst and an Fe3+/Fe2+ redox system. *Chem. Phys. Lett.* **1997,** *277* (4), 387-391.

29. Guo, Y.; Quan, X.; Lu, N.; Zhao, H.; Chen, S., High Photocatalytic Capability of Self-Assembled Nanoporous WO3 with Preferential Orientation of (002) Planes. *Environmental Science & Technology* **2007,** *41* (12), 4422-4427.

30. Konta, R.; Ishii, T.; Kato, H.; Kudo, A., Photocatalytic Activities of Noble Metal Ion Doped SrTiO3 under Visible Light Irradiation. *The Journal of Physical Chemistry B* **2004,** *108* (26), 8992-8995.

31. Yu, H.; Wang, J.; Yan, S.; Yu, T.; Zou, Z., Elements doping to expand the light response of SrTiO3. *Journal of Photochemistry and Photobiology A: Chemistry* **2014,** *275* (0), 65-71.

32. Zhou, L.; Wang, W.; Liu, S.; Zhang, L.; Xu, H.; Zhu, W., A sonochemical route to visible-light-driven high-activity BiVO4 photocatalyst. *J. Mol. Catal. A: Chem.* **2006,** *252* (1–2), 120-124.

33. Nagabhushana, G. P.; Nagaraju, G.; Chandrappa, G. T., Synthesis of bismuth vanadate: its application in H2 evolution and sunlight-driven photodegradation. *J. Mater. Chem. A* **2013,** *1* (2), 388-394.

34. Wachs, I. E.; Phivilay, S. P.; Roberts, C. A., Reporting of Reactivity for Heterogeneous Photocatalysis. *ACS Catalysis* **2013,** *3* (11), 2606-2611.

35. Kudo, A.; Miseki, Y., Heterogeneous photocatalyst materials for water splitting. *Chem. Soc. Rev.* **2009,** *38* (1), 253-278.

36. Jing, D.; Guo, L., A Novel Method for the Preparation of a Highly Stable and Active CdS Photocatalyst with a Special Surface Nanostructure. *The Journal of Physical Chemistry B* **2006,** *110* (23), 11139-11145.

37. Hu, Y.; Gao, X.; Yu, L.; Wang, Y.; Ning, J.; Xu, S.; Lou, X. W., Carbon-Coated CdS Petalous Nanostructures with Enhanced Photostability and Photocatalytic Activity. *Angew. Chem., Int. Ed.* **2013,** *52* (21), 5636-5639.

38. Reber, J. F.; Meier, K., Photochemical production of hydrogen with zinc sulfide suspensions. *The Journal of Physical Chemistry* **1984,** *88* (24), 5903-5913.

39. Rajabi, H. R.; Khani, O.; Shamsipur, M.; Vatanpour, V., High-performance pure and Fe3+-ion doped ZnS quantum dots as green nanophotocatalysts for the removal of malachite green under UV-light irradiation. *J. Hazard. Mater.* **2013,** *250–251* (0), 370-378.

40. James, D.; Zubkov, T., Photocatalytic properties of free and oxide-supported MoS2 and WS2 nanoparticles synthesized without surfactants. *Journal of Photochemistry and Photobiology A: Chemistry* **2013,** *262* (0), 45-51.

41. Yan, S. C.; Li, Z. S.; Zou, Z. G., Photodegradation Performance of g-C3N4 Fabricated by Directly Heating Melamine. *Langmuir* **2009,** *25* (17), 10397-10401.

42. Bai, X.; Wang, L.; Zong, R.; Zhu, Y., Photocatalytic Activity Enhanced via g-C3N4 Nanoplates to Nanorods. *The Journal of Physical Chemistry C* **2013,** *117* (19), 9952-9961.

43. Gogate, P. R.; Pandit, A. B., A review of imperative technologies for wastewater treatment I: oxidation technologies at ambient conditions. *Advances in Environmental Research* **2004,** *8* (3–4), 501-551.

44. Malato, S.; Fernández-Ibáñez, P.; Maldonado, M. I.; Blanco, J.; Gernjak, W., Decontamination and disinfection of water by solar photocatalysis: Recent overview and trends. *Catal. Today* **2009,** *147* (1), 1-59.

45. Chong, M. N.; Jin, B.; Chow, C. W. K.; Saint, C., Recent developments in photocatalytic water treatment technology: A review. *Water Res.* **2010,** *44* (10), 2997-3027.

46. Bahnemann, D., Photocatalytic water treatment: solar energy applications. *Solar Energy* **2004,** *77* (5), 445-459.

47. Peral, J.; Domènech, X.; Ollis, D. F., Heterogeneous Photocatalysis for Purification, Decontamination and Deodorization of Air. *Journal of Chemical Technology & Biotechnology* **1997,** *70* (2), 117-140.

48. Kanakaraju, D.; Glass, B.; Oelgemöller, M., Titanium dioxide photocatalysis for pharmaceutical wastewater treatment. *Environ. Chem. Lett.* **2014,** *12* (1), 27-47.

49. Zhao, W.; Ma, W.; Chen, C.; Zhao, J.; Shuai, Z., Efficient Degradation of Toxic Organic Pollutants with Ni2O3/TiO2-xBx under Visible Irradiation. *J. Am. Chem. Soc.* **2004,** *126* (15), 4782-4783.

50. Kabra, K.; Chaudhary, R.; Sawhney, R. L., Treatment of Hazardous Organic and Inorganic Compounds through Aqueous-Phase Photocatalysis: A Review. *Ind. Eng. Chem. Res.* **2004,** *43* (24), 7683-7696.

51. Herrmann, J.-M., Heterogeneous photocatalysis: fundamentals and applications to the removal of various types of aqueous pollutants. *Catal. Today* **1999,** *53* (1), 115-129.

52. Zollinger, H., *Color Chemistry: Syntheses, Properties, and Applications of Organic Dyes and Pigments*. Wiley: 2003.

53. Lachheb, H.; Puzenat, E.; Houas, A.; Ksibi, M.; Elaloui, E.; Guillard, C.; Herrmann, J.-M., Photocatalytic degradation of various types of dyes (Alizarin S, Crocein Orange G, Methyl Red, Congo Red, Methylene Blue) in water by UV-irradiated titania. *Appl. Catal., B* **2002,** *39* (1), 75-90.

54. Houas, A.; Lachheb, H.; Ksibi, M.; Elaloui, E.; Guillard, C.; Herrmann, J.-M., Photocatalytic degradation pathway of methylene blue in water. *Appl. Catal., B* **2001,** *31* (2), 145-157.

55. Kannan, N.; Sundaram, M. M., Kinetics and mechanism of removal of methylene blue by adsorption on various carbons—a comparative study. *Dyes Pigm.* **2001,** *51* (1), 25-40.

56. Zhang, T.; Oyama, T.; Aoshima, A.; Hidaka, H.; Zhao, J.; Serpone, N., Photooxidative N-demethylation of methylene blue in aqueous TiO2 dispersions under UV irradiation. *Journal of Photochemistry and Photobiology A: Chemistry* **2001,** *140* (2), 163-172.

57. Wu, T.; Liu, G.; Zhao, J.; Hidaka, H.; Serpone, N., Photoassisted Degradation of Dye Pollutants. V. Self-Photosensitized Oxidative Transformation of Rhodamine B under Visible Light Irradiation in Aqueous TiO2 Dispersions. *The Journal of Physical Chemistry B* **1998,** *102* (30), 5845-5851.

58. Greenwood, N. N.; Earnshaw, A., *Chemistry of the Elements*. Oxford: Pergamon Press: 1984; p 1117-1119.

59. Gratzel, M., Photoelectrochemical cells. *Nature* **2001,** *414* (6861), 338-344.

60. Maness, P.-C.; Smolinski, S.; Blake, D. M.; Huang, Z.; Wolfrum, E. J.; Jacoby, W. A., Bactericidal Activity of Photocatalytic TiO2 Reaction: toward an Understanding of Its Killing Mechanism. *Appl. Environ. Microbiol.* **1999,** *65* (9), 4094-4098.

61. Dalton, J. S.; Janes, P. A.; Jones, N. G.; Nicholson, J. A.; Hallam, K. R.; Allen, G. C., Photocatalytic oxidation of NOx gases using TiO2: a surface spectroscopic approach. *Environ. Pollut.* **2002,** *120* (2), 415-422.

62. Linsebigler, A. L.; Lu, G.; Yates, J. T., Photocatalysis on TiO2 Surfaces: Principles, Mechanisms, and Selected Results. *Chemical Reviews* **1995,** *95* (3), 735-758.

63. Fujishima, A.; Zhang, X.; Tryk, D. A., TiO2 photocatalysis and related surface phenomena. *Surf. Sci. Rep.* **2008,** *63* (12), 515-582.

64. Park, N. G.; van de Lagemaat, J.; Frank, A. J., Comparison of Dye-Sensitized Rutile- and Anatase-Based TiO2 Solar Cells. *The Journal of Physical Chemistry B* **2000,** *104* (38), 8989-8994.

65. Riegel, G.; Bolton, J. R., Photocatalytic Efficiency Variability in TiO2 Particles. *The Journal of Physical Chemistry* **1995,** *99* (12), 4215-4224.

66. Li, G.; Gray, K. A., Preparation of Mixed-Phase Titanium Dioxide Nanocomposites via Solvothermal Processing. *Chem. Mater.* **2007,** *19* (5), 1143-1146.

67. Scanlon, D. O.; Dunnill, C. W.; Buckeridge, J.; Shevlin, S. A.; Logsdail, A. J.; Woodley, S. M.; Catlow, C. R. A.; Powell, M. J.; Palgrave, R. G.; Parkin, I. P.; Watson, G. W.; Keal, T. W.; Sherwood, P.; Walsh, A.; Sokol, A. A., Band alignment of rutile and anatase TiO2. *Nat. Mater.* **2013,** *12* (9), 798-801.

68. Luo, H.; Takata, T.; Lee, Y.; Zhao, J.; Domen, K.; Yan, Photocatalytic Activity Enhancing for Titanium Dioxide by Co-doping with Bromine and Chlorine. *Chem. Mater.* **2004,** *16* (5), 846-849.

69. Shannon, R. D.; Pask, J. A., Kinetics of the Anatase-Rutile Transformation. *J. Am. Ceram. Soc.* **1965,** *48* (8), 391-398.

70. Tang, H.; Prasad, K.; Sanjinès, R.; Schmid, P. E.; Lévy, F., Electrical and optical properties of TiO2 anatase thin films. *J. Appl. Phys.* **1994,** *75* (4), 2042-2047.

71. Abayev, I.; Zaban, A.; Fabregat-Santiago, F.; Bisquert, J., Electronic conductivity in nanostructured TiO2 films permeated with electrolyte. *physica status solidi (a)* **2003,** *196* (1), R4-R6.

72. Anpo, M.; Kamat, P. V., *Environmentally Benign Photocatalysts: Applications of Titanium Oxide-based Materials*. Springer: 2010.

73. *Carbon Black, Titanium Dioxide, and Talc*; International Agency for Research on Cancer: Lyon, France, 2010.

74. DuPont. DuPont Ti-Pure titanium dioxide 2007. (accessed 17 March 2014).

75. Boffetta, P.; Soutar, A.; Cherrie, J. W.; Granath, F.; Andersen, A.; Anttila, A.; Blettner, M.; Gaborieau, V.; Klug, S. J.; Langard, S.; Luce, D.; Merletti, F.; Miller, B.; Mirabelli, D.; Pukkala, E.; Adami, H.; Olov; Weiderpass, E., Mortality Among Workers Employed in the Titanium Dioxide Production Industry in Europe. *Cancer Causes and Control* **2004,** *15* (7), 697-706.

76. Ong, W.-J.; Tan, L.-L.; Chai, S.-P.; Yong, S.-T.; Mohamed, A. R., Facet-Dependent Photocatalytic Properties of TiO2-Based Composites for Energy Conversion and Environmental Remediation. *Chemsuschem* **2014,** *7* (3), 690-719.

77. Chen, X.; Mao, S. S., Titanium Dioxide Nanomaterials: Synthesis, Properties, Modifications, and Applications. *Chemical Reviews* **2007,** *107* (7), 2891-2959.

78. Hench, L. L.; West, J. K., The sol-gel process. *Chemical Reviews* **1990,** *90* (1), 33-72.

79. Testino, A.; Bellobono, I. R.; Buscaglia, V.; Canevali, C.; D'Arienzo, M.; Polizzi, S.; Scotti, R.; Morazzoni, F., Optimizing the Photocatalytic Properties of Hydrothermal TiO2 by the Control of Phase Composition and Particle Morphology. A Systematic Approach. *J. Am. Chem. Soc.* **2007,** *129* (12), 3564-3575.

80. Liu, N.; Chen, X.; Zhang, J.; Schwank, J. W., A review on TiO2-based nanotubes synthesized via hydrothermal method: Formation mechanism, structure modification, and photocatalytic applications. *Catal. Today* **2014,** *225* (0), 34-51.

81. Yang, H. G.; Liu, G.; Qiao, S. Z.; Sun, C. H.; Jin, Y. G.; Smith, S. C.; Zou, J.; Cheng, H. M.; Lu, G. Q., Solvothermal Synthesis and Photoreactivity of Anatase TiO2 Nanosheets with Dominant {001} Facets. *J. Am. Chem. Soc.* **2009,** *131* (11), 4078-4083.

82. Wang, J.; Tafen, D. N.; Lewis, J. P.; Hong, Z.; Manivannan, A.; Zhi, M.; Li, M.; Wu, N., Origin of Photocatalytic Activity of Nitrogen-Doped TiO2 Nanobelts. *J. Am. Chem. Soc.* **2009,** *131* (34), 12290-12297.

83. De Marco, L.; Manca, M.; Giannuzzi, R.; Malara, F.; Melcarne, G.; Ciccarella, G.; Zama, I.; Cingolani, R.; Gigli, G., Novel Preparation Method of TiO2-Nanorod-Based Photoelectrodes for Dye-Sensitized Solar Cells with Improved Light-Harvesting Efficiency. *J. Phys. Chem. C* **2010,** *114* (9), 4228-4236.

84. Wen, B.-M.; Liu, C.-Y.; Liu, Y., Solvothermal synthesis of ultralong single-crystalline TiO2 nanowires. *New J. Chem.* **2005,** *29* (7), 969-971.

85. Liao, J.-Y.; Higgins, D.; Lui, G.; Chabot, V.; Xiao, X.; Chen, Z., Multifunctional TiO2–C/MnO2 Core–Double-Shell Nanowire Arrays as High-Performance 3D Electrodes for Lithium Ion Batteries. *Nano Lett.* **2013,** *13* (11), 5467-5473.

86. Zhao, Z.; Jiao, X.; Chen, D., Preparation of TiO2 aerogels by a sol-gel combined solvothermal route. *J. Mater. Chem.* **2009,** *19* (19), 3078-3083.

87. Li, Y.; Fu, Z.-Y.; Su, B.-L., Hierarchically Structured Porous Materials for Energy Conversion and Storage. *Adv. Funct. Mater.* **2012,** *22* (22), 4634-4667.

88. Mali, S. S.; Kim, H.; Shim, C. S.; Patil, P. S.; Kim, J. H.; Hong, C. K., Surfactant free most probable TiO2 nanostructures via hydrothermal and its dye sensitized solar cell properties. *Sci. Rep.* **2013,** *3*.

89. Sun, Z.; Kim, J. H.; Zhao, Y.; Bijarbooneh, F.; Malgras, V.; Lee, Y.; Kang, Y.-M.; Dou, S. X., Rational Design of 3D Dendritic TiO2 Nanostructures with Favorable Architectures. *J. Am. Chem. Soc.* **2011,** *133* (48), 19314-19317.

90. Ye, M.; Xin, X.; Lin, C.; Lin, Z., High Efficiency Dye-Sensitized Solar Cells Based on Hierarchically Structured Nanotubes. *Nano Lett.* **2011,** *11* (8), 3214-3220.

91. Yu, J. G.; Zhang, L. J.; Cheng, B.; Su, Y. R., Hydrothermal preparation and photocatalytic activity of hierarchically sponge-like macro-/mesoporous titania. *J. Phys. Chem. C* **2007,** *111* (28), 10582-10589.

92. Choi, W.; Termin, A.; Hoffmann, M. R., The Role of Metal Ion Dopants in Quantum-Sized TiO2: Correlation between Photoreactivity and Charge Carrier Recombination Dynamics. *The Journal of Physical Chemistry* **1994,** *98* (51), 13669-13679.

93. Colmenares, J. C.; Aramendía, M. A.; Marinas, A.; Marinas, J. M.; Urbano, F. J., Synthesis, characterization and photocatalytic activity of different metal-doped titania systems. *Applied Catalysis A: General* **2006,** *306* (0), 120-127.

94. Ranjit, K. T.; Viswanathan, B., Photocatalytic reduction of nitrite and nitrate ions over doped TiO2 catalysts. *Journal of Photochemistry and Photobiology A: Chemistry* **1997,** *107* (1–3), 215-220.

95. Xu, A.-W.; Gao, Y.; Liu, H.-Q., The Preparation, Characterization, and their Photocatalytic Activities of Rare-Earth-Doped TiO2 Nanoparticles. *J. Catal.* **2002,** *207* (2), 151-157.

96. Choi, Y.; Umebayashi, T.; Yoshikawa, M., Fabrication and characterization of C-doped anatase TiO2 photocatalysts. *J. Mater. Sci.* **2004,** *39* (5), 1837-1839.

97. Burda, C.; Lou, Y.; Chen, X.; Samia, A. C. S.; Stout, J.; Gole, J. L., Enhanced Nitrogen Doping in TiO2 Nanoparticles. *Nano Lett.* **2003,** *3* (8), 1049-1051.

98. Ho, W.; Yu, J. C.; Lee, S., Low-temperature hydrothermal synthesis of S-doped TiO2 with visible light photocatalytic activity. *J. Solid State Chem.* **2006,** *179* (4), 1171-1176.

99. Yu, J. C.; Yu; Ho; Jiang; Zhang, Effects of F- Doping on the Photocatalytic Activity and Microstructures of Nanocrystalline TiO2 Powders. *Chem. Mater.* **2002,** *14* (9), 3808-3816.

100. Sun, W. T.; Yu, Y.; Pan, H. Y.; Gao, X. F.; Chen, Q.; Peng, L. M., CdS quantum dots sensitized TiO2 nanotube-array photoelectrodes. *J. Am. Chem. Soc.* **2008,** *130* (4), 1124-+.

101. Bessekhouad, Y.; Robert, D.; Weber, J. V., Photocatalytic activity of Cu2O/TiO2, Bi2O3/TiO2 and ZnMn2O4/TiO2 heterojunctions. *Catal. Today* **2005,** *101* (3–4), 315-321.

102. Brahimi, R.; Bessekhouad, Y.; Bouguelia, A.; Trari, M., Improvement of eosin visible light degradation using PbS-sensititized TiO2. *Journal of Photochemistry and Photobiology A: Chemistry* **2008,** *194* (2–3), 173-180.

103. Sayama, K.; Mukasa, K.; Abe, R.; Abe, Y.; Arakawa, H., Stoichiometric water splitting into H2 and O2 using a mixture of two different photocatalysts and an IO3-/I- shuttle redox mediator under visible light irradiation. *Chem Commun* **2001,** (23), 2416-2417.

104. Nazeeruddin, M. K.; Splivallo, R.; Liska, P.; Comte, P.; Gratzel, M., A swift dye uptake procedure for dye sensitized solar cells. *Chem Commun* **2003,** (12), 1456-1457.

105. Senevirathna, M. K. I.; Pitigala, P. K. D. D. P.; Tennakone, K., Water photoreduction with Cu2O quantum dots on TiO2 nano-particles. *Journal of Photochemistry and Photobiology A: Chemistry* **2005,** *171* (3), 257-259.

106. Kongkanand, A.; Tvrdy, K.; Takechi, K.; Kuno, M.; Kamat, P. V., Quantum Dot Solar Cells. Tuning Photoresponse through Size and Shape Control of CdSe−TiO2 Architecture. *J. Am. Chem. Soc.* **2008,** *130* (12), 4007-4015.

107. Subramanian, V.; Wolf, E.; Kamat, P. V., Semiconductor−Metal Composite Nanostructures. To What Extent Do Metal Nanoparticles Improve the Photocatalytic Activity of TiO2 Films? *The Journal of Physical Chemistry B* **2001,** *105* (46), 11439-11446.

108. Arabatzis, I. M.; Stergiopoulos, T.; Bernard, M. C.; Labou, D.; Neophytides, S. G.; Falaras, P., Silver-modified titanium dioxide thin films for efficient photodegradation of methyl orange. *Appl. Catal., B* **2003,** *42* (2), 187-201.

109. Osterloh, F. E., Inorganic Materials as Catalysts for Photochemical Splitting of Water. *Chem. Mater.* **2007,** *20* (1), 35-54.

110. Castro Neto, A. H.; Guinea, F.; Peres, N. M. R.; Novoselov, K. S.; Geim, A. K., The electronic properties of graphene. *Reviews of Modern Physics* **2009,** *81* (1), 109-162.

111. Novoselov, K. S.; Geim, A. K.; Morozov, S. V.; Jiang, D.; Zhang, Y.; Dubonos, S. V.; Grigorieva, I. V.; Firsov, A. A., Electric Field Effect in Atomically Thin Carbon Films. *Science* **2004,** *306* (5696), 666-669.

112. AB, N. M. The Nobel Prize in Physics 2010. http://www.nobelprize.org/nobel_prizes/physics/laureates/2010/ (accessed March 11 2014).

113. Geim, A. K.; Novoselov, K. S., The rise of graphene. *Nat. Mater.* **2007,** *6* (3), 183-191.

114. Chen, J.-H.; Jang, C.; Xiao, S.; Ishigami, M.; Fuhrer, M. S., Intrinsic and extrinsic performance limits of graphene devices on SiO2. *Nat Nano* **2008,** *3* (4), 206-209.

115. Stoller, M. D.; Park, S.; Zhu, Y.; An, J.; Ruoff, R. S., Graphene-Based Ultracapacitors. *Nano Lett.* **2008,** *8* (10), 3498-3502.

116. Zhang, H.; Lv, X.; Li, Y.; Wang, Y.; Li, J., P25-Graphene Composite as a High Performance Photocatalyst. *ACS Nano* **2010,** *4* (1), 380-386.

117. Czerw, R.; Foley, B.; Tekleab, D.; Rubio, A.; Ajayan, P. M.; Carroll, D. L., Substrate-interface interactions between carbon nanotubes and the supporting substrate. *Phys Rev B* **2002,** *66* (3), 033408.

118. Ocak, Y. S.; Kulakci, M.; Kılıçoğlu, T.; Turan, R.; Akkılıç, K., Current–voltage and capacitance–voltage characteristics of a Sn/Methylene Blue/p-Si Schottky diode. *Synth. Met.* **2009,** *159* (15–16), 1603-1607.

119. Rao, C. N. R.; Sood, A. K.; Subrahmanyam, K. S.; Govindaraj, A., Graphene: The New Two-Dimensional Nanomaterial. *Angew. Chem., Int. Ed.* **2009,** *48* (42), 7752-7777.

120. Dreyer, D. R.; Park, S.; Bielawski, C. W.; Ruoff, R. S., The chemistry of graphene oxide. *Chem. Soc. Rev.* **2010,** *39* (1), 228-240.

121. Hummers, W. S.; Offeman, R. E., Preparation of Graphitic Oxide. *J. Am. Chem. Soc.* **1958,** *80* (6), 1339-1339.

122. Marcano, D. C.; Kosynkin, D. V.; Berlin, J. M.; Sinitskii, A.; Sun, Z.; Slesarev, A.; Alemany, L. B.; Lu, W.; Tour, J. M., Improved Synthesis of Graphene Oxide. *ACS Nano* **2010,** *4* (8), 4806-4814.

123. Xiang, Q.; Yu, J.; Jaroniec, M., Graphene-based semiconductor photocatalysts. *Chem. Soc. Rev.* **2012,** *41* (2), 782-796.

124. Morales-Torres, S.; Pastrana-Martinez, L. M.; Figueiredo, J. L.; Faria, J. L.; Silva, A. M. T., Design of graphene-based TiO2 photocatalysts-a review. *Environmental Science and Pollution Research* **2012,** *19* (9), 3676-3687.

125. Tan, L. L.; Chai, S. P.; Mohamed, A. R., Synthesis and Applications of Graphene-Based TiO2 Photocatalysts. *Chemsuschem* **2012,** *5* (10), 1868-1882.

126. Liu, Z.; Robinson, J. T.; Sun, X.; Dai, H., PEGylated Nanographene Oxide for Delivery of Water-Insoluble Cancer Drugs. *J. Am. Chem. Soc.* **2008,** *130* (33), 10876-10877.

127. Fan, W.; Lai, Q.; Zhang, Q.; Wang, Y., Nanocomposites of TiO2 and Reduced Graphene Oxide as Efficient Photocatalysts for Hydrogen Evolution. *J. Phys. Chem. C* **2011,** *115* (21), 10694-10701.

128. Williams, G.; Seger, B.; Kamat, P. V., TiO2-graphene nanocomposites. UV-assisted photocatalytic reduction of graphene oxide. *ACS Nano* **2008,** *2* (7), 1487-1491.

129. Guo, J. J.; Zhu, S. M.; Chen, Z. X.; Li, Y.; Yu, Z. Y.; Liu, Q. L.; Li, J. B.; Feng, C. L.; Zhang, D., Sonochemical synthesis of TiO2 nanoparticles on graphene for use as photocatalyst. *Ultrason. Sonochem.* **2011,** *18* (5), 1082-1090.

130. Shen, J. F.; Yan, B.; Shi, M.; Ma, H. W.; Li, N.; Ye, M. X., One step hydrothermal synthesis of TiO2-reduced graphene oxide sheets. *J. Mater. Chem.* **2011,** *21* (10), 3415-3421.

131. Nethravathi, C.; Rajamathi, M., Chemically modified graphene sheets produced by the solvothermal reduction of colloidal dispersions of graphite oxide. *Carbon* **2008,** *46* (14), 1994-1998.

132. Tuinstra, F.; Koenig, J. L., Raman Spectrum of Graphite. *J. Chem. Phys.* **1970,** *53* (3), 1126-&.

133. Zhang, X.-Y.; Li, H.-P.; Cui, X.-L.; Lin, Y., Graphene/TiO2 nanocomposites: synthesis, characterization and application in hydrogen evolution from water photocatalytic splitting. *J. Mater. Chem.* **2010,** *20*, 2801-2806.

134. Liu, B. T.; Huang, Y. J.; Wen, Y.; Du, L. J.; Zeng, W.; Shi, Y. R.; Zhang, F.; Zhu, G.; Xu, X. H.; Wang, Y. H., Highly dispersive {001} facets-exposed nanocrystalline TiO2 on high quality graphene as a high performance photocatalyst. *J. Mater. Chem.* **2012,** *22* (15), 7484-7491.

135. Perera, S. D.; Mariano, R. G.; Vu, K.; Nour, N.; Seitz, O.; Chabal, Y.; Balkus, K. J., Hydrothermal Synthesis of Graphene-TiO2 Nanotube Composites with Enhanced Photocatalytic Activity. *Acs Catalysis* **2012,** *2* (6), 949-956.

136. Farhangi, N.; Chowdhury, R. R.; Medina-Gonzalez, Y.; Ray, M. B.; Charpentier, P. A., Visible light active Fe doped TiO2 nanowires grown on graphene using supercritical CO2. *Applied Catalysis B-Environmental* **2011,** *110*, 25-32.

137. Liu, J. C.; Bai, H. W.; Wang, Y. J.; Liu, Z. Y.; Zhang, X. W.; Sun, D. D., Self-Assembling TiO2 Nanorods on Large Graphene Oxide Sheets at a Two-Phase Interface and Their Anti-Recombination in Photocatalytic Applications. *Adv. Funct. Mater.* **2010,** *20* (23), 4175-4181.

138. Chang, J.; Yang, J.; Ma, P.; Wu, D.; Tian, L.; Gao, Z.; Jiang, K.; Yang, L., Hierarchical titania mesoporous sphere/graphene composite, synthesis and application as photoanode in dye sensitized solar cells. *J. Colloid Interface Sci.* **2013,** *394* (0), 231 - 236.

139. Lambert, T. N.; Chavez, C. A.; Hernandez-Sanchez, B.; Lu, P.; Bell, N. S.; Ambrosini, A.; Friedman, T.; Boyle, T. J.; Wheeler, D. R.; Huber, D. L., Synthesis and Characterization of Titania-Graphene Nanocomposites. *J. Phys. Chem. C* **2009,** *113* (46), 19812-19823.

140. Du, J.; Lai, X. Y.; Yang, N. L.; Zhai, J.; Kisailus, D.; Su, F. B.; Wang, D.; Jiang, L., Hierarchically Ordered Macro-Mesoporous TiO2-Graphene Composite Films: Improved Mass Transfer, Reduced Charge Recombination, and Their Enhanced Photocatalytic Activities. *ACS Nano* **2011,** *5* (1), 590-596.

141. Gao, P.; Liu, Z.; Tai, M.; Sun, D. D.; Ng, W., Multifunctional graphene oxide–TiO2 microsphere hierarchical membrane for clean water production. *Appl. Catal., B* **2013,** *138–139* (0), 17-25.

142. Luo, Y. S.; Luo, J. S.; Zhou, W. W.; Qi, X. Y.; Zhang, H.; Yu, D. Y. W.; Li, C. M.; Fan, H. J.; Yu, T., Controlled synthesis of hierarchical graphene-wrapped TiO2@Co3O4 coaxial nanobelt arrays for high-performance lithium storage. *J. Mater. Chem. A* **2013,** *1* (2), 273-281.

143. Yu, S.; Yun, H. J.; Kim, Y. H.; Yi, J., Carbon-doped TiO2 nanoparticles wrapped with nanographene as a high performance photocatalyst for phenol degradation under visible light irradiation. *Appl. Catal., B* **2014,** *144* (0), 893-899.

144. Oh, Y.; Nam, S.; Wi, S.; Kang, J.; Hwang, T.; Lee, S.; Park, H. H.; Cabana, J.; Kim, C.; Park, B., Effective wrapping of graphene on individual Li4Ti5O12 grains for high-rate Li-ion batteries. *J. Mater. Chem. A* **2014,** *2* (7), 2023-2027.

145. Dai, Y. Q.; Jing, Y.; Zeng, J.; Qi, Q.; Wang, C. L.; Goldfeld, D.; Xu, C. H.; Zheng, Y. P.; Sun, Y. M., Nanocables composed of anatase nanofibers wrapped in UV-light reduced graphene oxide and their enhancement of photoinduced electron transfer in photoanodes. *J. Mater. Chem.* **2011,** *21* (45), 18174-18179.

146. Chen, J. S.; Wang, Z.; Dong, X. C.; Chen, P.; Lou, X. W., Graphene-wrapped TiO2 hollow structures with enhanced lithium storage capabilities. *Nanoscale* **2011,** *3* (5), 2158-2161.

147. Lee, J. S.; You, K. H.; Park, C. B., Highly Photoactive, Low Bandgap TiO2 Nanoparticles Wrapped by Graphene. *Adv. Mater.* **2012,** *24* (8), 1084-1088.

148. Zhu, J. Y.; He, J. H., Facile Synthesis of Graphene-Wrapped Honeycomb MnO2 Nanospheres and Their Application in Supercapacitors. *ACS Appl. Mater. Interfaces* **2012,** *4* (3), 1770-1776.

149. Hao, X.; Kuang, C.; Gu, Z.; Wang, Y.; Li, S.; Ku, Y.; Li, Y.; Ge, J.; Liu, X., From microscopy to nanoscopy via visible light. *Light Sci Appl* **2013,** *2*, e108.

150. Broglie, L. d., Recherches sur la théorie des quanta. *Ann. Phys.* **1925,** *3* (22).

151. Zhou, W.; Wang, Z. L., *Scanning Microscopy for Nanotechnology*. Springer: Verlag, 2006; p 1-32.

152. ISAAC, Scanning Electron Miscroscopy (SEM). University of Glasgow.

153. Williams, D. B.; Carter, C. B., *Transmission Electron Microscopy - A Textbook for Materials Science*. Springer: New York, 2009; p 141.

154. Azaroff, L. V.; Kaplow, R.; Kato, N.; Weiss, R. J.; Wilson, A.; Young, R., *X-ray Diffraction*. McGraw-Hill: New York, 1974.

155. Connolly, J. R., Introduction to X-ray Powder Diffraction. The University of New Mexico, 2007.

156. Langford, J. I.; Wilson, A. J. C., Scherrer after sixty years: A survey and some new results in the determination of crystallite size. *J. Appl. Crystallogr.* **1978,** *11* (2), 102-113.

157. Brunauer, S.; Emmett, P. H.; Teller, E., Adsorption of Gases in Multimolecular Layers. *J. Am. Chem. Soc.* **1938,** *60* (2), 309-319.

158. Clark, B. J.; Frost, T.; Russell, A.; Group, U. S., *UV Spectroscopy: Techniques, Instrumentation and Data Handling*. Springer: 1993.

159. Kortüm, G.; Braun, W.; Herzog, G., Principles and Techniques of Diffuse-Reflectance Spectroscopy. *Angewandte Chemie International Edition in English* **1963,** *2* (7), 333-341.

160. Newport, Principle of operation of an integrating sphere. The incoming beam is diffusely reflected inside an integrating sphere. The output port cannot "see" the region of first impact. 1162, Ed. 2014.

161. Tauc, J.; Grigorovici, R.; Vancu, A., Optical Properties and Electronic Structure of Amorphous Germanium. *physica status solidi (b)* **1966,** *15* (2), 627-637.

162. Griffiths, P. R.; De Haseth, J. A., *Fourier Transform Infrared Spectrometry*. Wiley: 2007.

163. Zhang, Y.; Tang, Z. R.; Fu, X.; Xu, Y. J., TiO2-graphene nanocomposites for gas-phase photocatalytic degradation of volatile aromatic pollutant: is TiO2-graphene truly different from other TiO2-carbon composite materials? *ACS Nano* **2010,** *4* (12), 7303-14.

164. Sakthivel, S.; Kisch, H., Daylight Photocatalysis by Carbon-Modified Titanium Dioxide. *Angew. Chem., Int. Ed.* **2003,** *42* (40), 4908-4911.

165. Gardiner, D. J.; Graves, P. R.; Bowley, H. J., *Practical Raman spectroscopy*. Springer-Verlag: 1989.

166. Ferrari, A. C.; Meyer, J. C.; Scardaci, V.; Casiraghi, C.; Lazzeri, M.; Mauri, F.; Piscanec, S.; Jiang, D.; Novoselov, K. S.; Roth, S.; Geim, A. K., Raman Spectrum of Graphene and Graphene Layers. *Phys. Rev. Lett.* **2006,** *97* (18), 187401.

167. Bard, A. J.; Faulkner, L. R., *Electrochemical Methods; Fundamentals and Applications*. Wiley Interscience Publications: 2000.

168. Hu, C.-C.; Chen, W.-C.; Chang , K.-H., How to Achieve Maximum Utilization of Hydrous Ruthenium Oxide for Supercapacitors. *J. Electrochem. Soc.* **2004,** *151* (2), A281-A290.

169. Lui, G.; Liao, J.-Y.; Duan, A.; Zhang, Z.; Fowler, M.; Yu, A., Graphene-wrapped hierarchical TiO2 nanoflower composites with enhanced photocatalytic performance. *J. Mater. Chem. A* **2013,** *1* (39), 12255-12262.

170. Chen, D. H.; Caruso, R. A., Recent Progress in the Synthesis of Spherical Titania Nanostructures and Their Applications. *Adv. Funct. Mater.* **2013,** *23* (11), 1356-1374.

171. Macak, J. M.; Zlamal, M.; Krysa, J.; Schmuki, P., Self-organized TiO2 nanotube layers as highly efficient photocatalysts. *Small* **2007,** *3* (2), 300-304.

172. Mao, Y.; Wong, S. S., Size- and Shape-Dependent Transformation of Nanosized Titanate into Analogous Anatase Titania Nanostructures. *J. Am. Chem. Soc.* **2006,** *128* (25), 8217-8226.

173. Sun, Z.; Kim, J. H.; Zhao, Y.; Attard, D.; Dou, S. X., Morphology-controllable 1D-3D nanostructured TiO2 bilayer photoanodes for dye-sensitized solar cells. *Chem Commun (Camb)* **2013,** *49* (10), 966-8.

174. Zhu, K.; Vinzant, T. B.; Neale, N. R.; Frank, A. J., Removing structural disorder from oriented TiO2 nanotube arrays: Reducing the dimensionality of transport and recombination in dye-sensitized solar cells. *Nano Lett.* **2007,** *7* (12), 3739-3746.

175. Liao, J. Y.; He, J. W.; Xu, H. Y.; Kuang, D. B.; Su, C. Y., Effect of TiO2 morphology on photovoltaic performance of dye-sensitized solar cells: nanoparticles, nanofibers, hierarchical spheres and ellipsoid spheres. *J. Mater. Chem.* **2012,** *22* (16), 7910-7918.

176. Wu, G.; Wang, J.; Thomas, D. F.; Chen, A., Synthesis of F-Doped Flower-like TiO2 Nanostructures with High Photoelectrochemical Activity. *Langmuir* **2008,** *24* (7), 3503-3509.

177. Liao, J. Y.; Lei, B. X.; Kuang, D. B.; Su, C. Y., Tri-functional hierarchical TiO2 spheres consisting of anatase nanorods and nanoparticles for high efficiency dye-sensitized solar cells. *Energy Environ. Sci.* **2011,** *4* (10), 4079-4085.

178. Bakardjieva, S.; Šubrt, J.; Štengl, V.; Dianez, M. J.; Sayagues, M. J., Photoactivity of anatase–rutile TiO2 nanocrystalline mixtures obtained by heat treatment of homogeneously precipitated anatase. *Appl. Catal., B* **2005,** *58* (3–4), 193-202.

179. Kim, C.-S.; Kwon, I.-M.; Moon, B. K.; Jeong, J. H.; Choi, B.-C.; Kim, J. H.; Choi, H.; Yi, S. S.; Yoo, D.-H.; Hong, K.-S.; Park, J.-H.; Lee, H. S., Synthesis and particle size effect on the phase transformation of nanocrystalline TiO2. *Mater. Sci. Eng., C* **2007,** *27* (5–8), 1343-1346.

180. Wang, D. H.; Jia, L.; Wu, X. L.; Lu, L. Q.; Xu, A. W., One-step hydrothermal synthesis of N-doped TiO2/C nanocomposites with high visible light photocatalytic activity. *Nanoscale* **2012,** *4* (2), 576-84.

181. Tian, F.; Zhang, Y.; Zhang, J.; Pan, C., Raman Spectroscopy: A New Approach to Measure the Percentage of Anatase TiO2 Exposed (001) Facets. *The Journal of Physical Chemistry C* **2012,** *116* (13), 7515-7519.

182. Zhang, W. F.; He, Y. L.; Zhang, M. S.; Yin, Z.; Chen, Q., Raman scattering study on anatase TiO 2 nanocrystals. *J. Phys. D: Appl. Phys.* **2000,** *33* (8), 912.

183. Lin, H.; Huang, C. P.; Li, W.; Ni, C.; Shah, S. I.; Tseng, Y.-H., Size dependency of nanocrystalline TiO2 on its optical property and photocatalytic reactivity exemplified by 2-chlorophenol. *Appl. Catal., B* **2006,** *68* (1–2), 1-11.

184. An, G.; Ma, W.; Sun, Z.; Liu, Z.; Han, B.; Miao, S.; Miao, Z.; Ding, K., Preparation of titania/carbon nanotube composites using supercritical ethanol and their photocatalytic activity for phenol degradation under visible light irradiation. *Carbon* **2007,** *45* (9), 1795-1801.

185. Ong, W.-J.; Gui, M. M.; Chai, S.-P.; Mohamed, A. R., Direct growth of carbon nanotubes on Ni/TiO2 as next generation catalysts for photoreduction of CO2 to methane by water under visible light irradiation. *RSC Adv.* **2013,** *3* (14), 4505-4509.

186. Li, Y.; Li, X.; Li, J.; Yin, J., Photocatalytic degradation of methyl orange by TiO2-coated activated carbon and kinetic study. *Water Res.* **2006,** *40* (6), 1119-1126.

187. Xue, G.; Liu, H.; Chen, Q.; Hills, C.; Tyrer, M.; Innocent, F., Synergy between surface adsorption and photocatalysis during degradation of humic acid on TiO2/activated carbon composites. *J. Hazard. Mater.* **2011,** *186* (1), 765-772.

188. Liang, Y.; Wang, H.; Sanchez Casalongue, H.; Chen, Z.; Dai, H., TiO2 nanocrystals grown on graphene as advanced photocatalytic hybrid materials. *Nano Res* **2010,** *3* (10), 701-705.

189. Zhang, Y.; Zhang, N.; Tang, Z. R.; Xu, Y. J., Improving the photocatalytic performance of graphene-TiO2 nanocomposites via a combined strategy of decreasing defects of graphene and increasing interfacial contact. *Phys. Chem. Chem. Phys.* **2012,** *14* (25), 9167-75.

190. Zhou, S. P.; Zhang, H. M.; Zhao, Q.; Wang, X. H.; Li, J.; Wang, F. S., Graphene-wrapped polyaniline nanofibers as electrode materials for organic supercapacitors. *Carbon* **2013,** *52,* 440-450.

191. Aravind, S. S. J.; Ramaprabhu, S., Pt Nanoparticle-Dispersed Graphene-Wrapped MWNT Composites As Oxygen Reduction Reaction Electrocatalyst in Proton Exchange Membrane Fuel Cell. *ACS Appl. Mater. Interfaces* **2012,** *4* (8), 3805-3810.

192. Ahn, K. S.; Seo, S. W.; Park, J. H.; Min, B. K.; Jung, W. S., The Preparation of Alumina Particles Wrapped in Few-layer Graphene Sheets and Their Application to Dye-sensitized Solar Cells. *Bull. Korean Chem. Soc.* **2011,** *32* (5), 1579-1582.

193. Kim, H. I.; Moon, G. H.; Monllor-Satoca, D.; Park, Y.; Choi, W., Solar Photoconversion Using Graphene/TiO2 Composites: Nanographene Shell on TiO2 Core versus TiO2 Nanoparticles on Graphene Sheet. *J. Phys. Chem. C* **2012,** *116* (1), 1535-1543.

194. Xiang, Q.; Yu, J., Graphene-Based Photocatalysts for Hydrogen Generation. *J. Phys. Chem. Lett.* **2013,** *4* (5), 753-759.

195. Hassan, F. M.; Chabot, V.; Li, J.; Kim, B. K.; Ricardez-Sandoval, L.; Yu, A., Pyrrolic-structure enriched nitrogen doped graphene for highly efficient next generation supercapacitors. *J. Mater. Chem. A* **2013,** *1* (8), 2904-2912.

196. Yu, A.; Roes, I.; Davies, A.; Chen, Z., Ultrathin, transparent, and flexible graphene films for supercapacitor application. *Appl. Phys. Lett.* **2010,** *96* (25), 253105-3.

197. Lee, Y.-C.; Yang, J.-W., Self-assembled flower-like TiO2 on exfoliated graphite oxide for heavy metal removal. *J. Ind. Eng. Chem.* **2012,** *18* (3), 1178-1185.

198. Xin, X.; Zhou, X. F.; Wu, J. H.; Yao, X. Y.; Liu, Z. P., Scalable Synthesis of TiO2/Graphene Nanostructured Composite with High-Rate Performance for Lithium Ion Batteries. *ACS Nano* **2012,** *6* (12), 11035-11043.

199. Stankovich, S.; Dikin, D. A.; Piner, R. D.; Kohlhaas, K. A.; Kleinhammes, A.; Jia, Y.; Wu, Y.; Nguyen, S. T.; Ruoff, R. S., Synthesis of graphene-based nanosheets via chemical reduction of exfoliated graphite oxide. *Carbon* **2007,** *45* (7), 1558-1565.

200. Pan, S.; Aksay, I. A., Factors Controlling the Size of Graphene Oxide Sheets Produced via the Graphite Oxide Route. *ACS Nano* **2011,** *5* (5), 4073-4083.

201. Shen, J.; Yan, B.; Shi, M.; Ma, H.; Li, N.; Ye, M., One step hydrothermal synthesis of TiO2-reduced graphene oxide sheets. *J. Mater. Chem.* **2011,** *21* (10), 3415-3421.

202. Wang, J.; Hernandez, Y.; Lotya, M.; Coleman, J. N.; Blau, W. J., Broadband Nonlinear Optical Response of Graphene Dispersions. *Adv. Mater.* **2009,** *21* (23), 2430-2435.

203. Long, M.; Qin, Y.; Chen, C.; Guo, X.; Tan, B.; Cai, W., Origin of Visible Light Photoactivity of Reduced Graphene Oxide/TiO2 by in Situ Hydrothermal Growth of Undergrown TiO2 with Graphene Oxide. *The Journal of Physical Chemistry C* **2013,** *117* (32), 16734-16741.

204. Zhu, J.; Yang, D.; Geng, J.; Chen, D.; Jiang, Z., Synthesis and characterization of bamboo-like CdS/TiO2 nanotubes composites with enhanced visible-light photocatalytic activity. *J Nanopart Res* **2008,** *10* (5), 729-736.

205. Sener, S.; Erdemoglu, M.; Asilturk, M.; Sayilkan, H., The Effect of Silane Modification on the Adsorptive Properties of Natural Pyrophyllite and Synthetic Titanium-Based Powders Prepared by the Sol-Gel Process. *Turk. J. Chem.* **2005,** *29* (5), 487-495.

206. Bourikas, K.; Vakros, J.; Kordulis, C.; Lycourghiotis, A., Potentiometric Mass Titrations: Experimental and Theoretical Establishment of a New Technique for Determining the Point of Zero Charge (PZC) of Metal (Hydr)Oxides. *J. Phys. Chem. B* **2003,** *107* (35), 9441-9451.

207. Kosmulski, M.; Matijevi?, E., Zeta potential of anatase (TiO2) in mixed solvents. *Colloids Surf.* **1992,** *64* (1), 57 - 65.